Investigation of low-cost infrared thermal sensors for monitoring water stress in grapevines

by

Jaco Luus

Thesis presented in partial fulfilment of the requirements for the degree of Master of Engineering (Mechanical) in the Faculty of Engineering at Stellenbosch University

Supervisor: Dr. D.N.J. Els

Co-supervisor: Dr. C. Poblete-Echeverría

December 2021

Declaration

By submitting this thesis electronically, I declare that the entirety of the work contained therein is my own, original work, that I am the sole author thereof (save to the extent explicitly otherwise stated), that reproduction and publication thereof by Stellenbosch University will not infringe any third party rights and that I have not previously in its entirety or in part submitted it for obtaining any qualification.

Date: December 2021 .....

Abstract

Investigation of low-cost infrared thermal sensors for monitoring water stress in grapevines

J. Luus

Department of Mechanical and Mechatronic Engineering,
University of Stellenbosch,
Private Bag X1, Matieland 7602, South Africa.

Thesis: MEng (Mech)

December 2021

Infrared (IR) measurement of canopy temperature is an effective method of determining plant water stress. The crop water stress index (CWSI) is a normalised plant water stress value that can be calculated from vineyard IR measurements. Normalising reference temperature measurements, uncertainty of IR sensor requirements and unstandardised physical measurement parameters are, however, a hindrance to the adoption of IR temperature measurement for plant water stress detection in vineyards.

To improve the CWSI reference temperatures, physical measurements in a commercial Cabernet Sauvignon vineyard were used to develop a heat transfer (HT) model and simple empirical (EMP) model for determining these temperatures by using optimisation. The HT model is derived from fundamental heat transfer principles and uses data from a commercial weather station, while the EMP model requires only ambient temperature and humidity data. The HT and EMP models could calculate reference temperatures to within 1.0 K and 1.5 K of physical measurements, respectively.

Low-cost IR array and single-area sensor canopy temperature measurements were compared to image analysed commercial IR camera measurements. The investigated low-cost IR array sensor was found to be unsuitable for CWSI measurements, while single-area sensors could measure temperatures similar to those of the IR camera. All low-cost sensors were, however, unable to accurately measure CWSI reference temperatures. It was determined that a sensors' spectral ranges have a significant effect on the measured canopy temperature, especially when measuring sunlit canopies.

Finally, the best physical conditions for measuring CWSI using different sensor types were investigated. It was found that low-cost single-area sensors could

measure CWSI accurately, as long as the sensor's field of view was taken into account. Furthermore, it was found that the shaded side of the canopy, measured one hour after solar noon, provided the best midday plant temperature measurements for all investigated sensors as it is more photosynthetically active from the morning sun. Using a single-area IR sensor for canopy temperature measurements along with the EMP method to determine the reference temperatures was found to be an effective low-cost and low-effort method of measuring CWSI in vineyards.

Uittreksel

Ondersoek in lae koste infrarooi termiese sensors vir die monitering van waterspanning in wingerde

("Investigation of low-cost infrared thermal sensors for monitoring water stress in grapevines")

J. Luus

Departement Meganiese en Megatroniese Ingenieurswese,
Universiteit van Stellenbosch,
Privaatsak X1, Matieland 7602, Suid Afrika.

Tesis: MIng (Meg)

Desember 2021

Infrarooi (IR) meting van wingerd lower temperatuur is 'n effektiewe manier om plant waterspanning te bepaal. Die gewas waterspanningsindeks (GWSI), is 'n genormaliseerde waterspanning waarde wat vanuit IR metings van wingerd temperatuur bepaal kan word. Normaliserende verwysingstemperature, onsekerheid oor IR sensor vereistes en ongestandaardiseerde meting prosedures is belemmerend tot die aanneming van IR temperatuur meting vir die bepaling van plant waterspanning in wingerde.

Om die GWSI verwysing temperature te verbeter, is fisiese metings in 'n kommersiële Cabernet Sauvignon wingerd gebruik om, deur middel van optimering, 'n hitte oordrag (HO) en empiriese (EMP) model te ontwikkel wat hierdie temperature kan bepaal. Die HO model is afgelei vanaf fundamentele hitte oordrag beginsels en gebruik weerstasie data, terwyl die EMP model slegs omgewings temperatuur en humiditeit data benodig. Die HO en EMP modelle kon die verwysingstemperature tot onderskeidelik 1.0 K en 1.5 K van die fisies gemete temperature bepaal.

Lower temperature gemeet deur lae koste veelvuldige- en enkel-area IR sensors is vergelyk met metings van 'n kommersiële IR kamera op veskillende afstande. Die lae koste veelvuldige- area sensor wat ondersoek is, kon nie akkurate waardes vir die GWSI bepaal nie. Die enkel-area sensors kon wel temperature vergelykbaar met die van die kommersiële IR kamera meet. Nie een van die goedkoop sensors kon die GWSI verwysings temperature akkuraat genoeg meet nie.

Dit is bepaal dat die spektrale gebied wat 'n IR sensor meet 'n merkwaardige effek het op die gemete lower temperture, veral as die wingerd in direkte sonlig is.

Laastens is die beste fisiese toestande vir die meting van GWSI met IR sensors ondersoek. Daar is gevind enkel-area lae koste sensors die GWSI akkuraat kon bepaal solank die besigtigingsarea van die sensors in ag geneem word. Daar is verder bepaal dat die skadukant van die lower, een uur na sonmiddag, die beste geleentheid bied vir die meting van lower temperature vir die GWSI. Hierdie kant van die lower werk goed omdat dit vir die heel oggend aktief gefotosinteer het. Daar is gevind dat 'n enkel-area sensor gepaard met die EMP metode om verwysings temperature te bepaal 'n effektiewe, goedkoop en maklike metode is om GWSI in wingerde te bepaal.

Acknowledgements

I would like to express my sincere gratitude to the following people and organisations:

- My supervisors Dr D.N.J. Els and Dr C. Poblete-Echeverría for their guidance throughout this study. Their involvement and sincere interest has inspired me to go the extra mile in exploring new ideas and committing to the long hours.
- Winetech and Vinepro for project support and funding.
- Thelema wine farm and its employees for giving us access to a premium Cabernet Sauvignon vineyard.
- Members of the Integrated Vineyard Monitoring System (IVMS) research group of Stellenbosch University, for supporting me on the measurement days. The measurements would not have been possible without them. I would like to thank the international students who joined us is these two difficult years.
- My parents, Pieter and Stefanie Luus, who inspired me to pursue my passion in Engineering and supported me throughout my University career.

Dedications

This thesis is dedicated to my Lord and Saviour, Jesus Christ, the True Vine.

Contents

List of Figures

List of Tables

Nomenclature

Abbreviations

CWSI	Crop water stress index
EMP	Empirical
FOV	Field of view
HT	Heat transfer
IR	Infrared
LEB	Leaf energy balance
LWP	Leaf water potential
MR	Measurement rig
MAE	Mean absolute error
MBE	Mean bias error
PCA	Principle component analysis
PSO	Particle swarm optimisation
RGB	Red green blue
ROI	Region of interest
RMSE	Root mean squared error
SWP	Stem water potential
TIR	Thermal infrared
UAV	Unmanned areal vehicle
VPD	Vapour pressure deficit
WP	White panel

Constants

$\sigma =$ $5.67 \cdot 10^{-8}\,\mathrm{W/m^2 \cdot K^4}$

Variables

A	Area	$[\mathrm{m^2}]$
B	Calibration coefficient	[ ]
c	Spesific heat capacity	[kJ/kgK]
D	Diffusion	[ ]

F	View factor	[ ]
f	Fitness value	[ ]
f	Fraction of radiation	[ ]
G	Incident radiation	[W/m^2]
h	Heat transfer coefficient	[m^2/s]
h	Enthalpy	[J/kg]
I	Index	[ ]
J	Radiosity	[W/m^2]
k	Thermal conductivity	[W/mK]
L	Length	[s/m]
$\dot{m}$	Mass flow rate	[kg/ms]
N	Sample size	[ ]
p	Damping factor	[ ]
P	Pressure	[Pa]
Pr	Prandtl Number	[ ]
$\dot{Q}$	Heat transfer rate	[J/s]
R	Radiation heat transfer	[W/m^2]
Re	Reynolds number	[ ]
r	Resistance to water vapour transfer	[s/m]
S	Signal relating to measured infrared radiation	[ ]
s	Standard error of the fit	[ ]
Sc	Schmidt number	[ ]
Sh	Sherwood relation	[ ]
T	Temperature	[K]
T'	Temperature	[°C]
V	Wind speed	[m/s]
z	Altitude	[m]
α	Solar absorptivity	[ ]
γ	Psychrometeric constant	[W/m^2]
δ	Empirical correlation coefficient	[ ]
ϵ	Emissivity	[ ]
θ	Angle of incidence error	[°]
λ	Latent heat of vaporization of water	[J/kg]
ρ	Density	[kg/m^3]
σ	Standard deviation	[ ]
υ	Kinematic viscosity	[m^2/s]

ϕ	Relative humidity	[%]
φ	Radiative heat flux	[W/m^2]

Subscripts

a	Ambient
bc	back canopy
c	Canopy
c	Characteristic
conv	Convection
dry	Dry reference
d	Diffuse
D	Direct
db	Dry-bulb
EMP	Empirical
evap	Evaporation
f	Measurement value
fg	Fluid to gas
H_2O	Water
i	Counter
j	Counter
l	Leaf
lb	Lower baseline
M	Model under consideration
N	Natural method
net	Net radiation
ni	Isothermal net radiation
o	Reference value
oc	Opposite canopy
r	Stomatal resistance
rad	Radiation
sol	Solar
sky	Sky
s	Soil
St	Stomatal
s	Surface
ub	Upper baseline
v	Vapour

wet	Wet reference
wb	Wet-bulb
∞	Far from a surface

Superscripts

$*$	Saturation

Chapter 1

Introduction

1.1 Overview

Globally, agriculture requires a vast supply of water, requiring 71.7% of global fresh water supply (FOA, 2017), and therefore, water management is critical for agriculture sustainability. In this context, wine-producing countries are frequently affected by drought conditions (Chaves *et al.*, 2010; Webb *et al.*, 2007). Increased temperatures put growers at risk of smaller yield, but also to changes in grapevine phenology (Choné *et al.*, 2001). It is a fact that viticulture will become more reliant on irrigation to compensate for the effects of climate change (Fraga *et al.*, 2018) with global surface temperatures 1.09 °C warmer in the 2011-2020 period compared to the 1850-1900 period (IPCC, 2021). Medrano *et al.* (2014) indicates that the 300 mm to 700 mm annual vineyard water consumptions is generally higher than the annual precipitation in many viticultural areas. Deficit irrigation strategies such as regulated-deficit irrigation and partial root zone drying, which reduce water consumption, can be used to improve fruit quality at the cost of a reduction in potential yield (Chaves *et al.*, 2007; Medrano *et al.*, 2014). Nevertheless, the implementation of irrigation strategies requires knowledge of the water status of the grapevines and narrower thresholds of physiological indices.

Stem water potential (SWP), a measurement of the pressure required to force a drop of water out of a leaf stem, is one of the standard methods of measuring plant water stress (Choné *et al.*, 2001). This method has been used successfully for many years. However, the use of SWP for irrigation scheduling in a commercial vineyard has some limitations in practice. SWP is destructive, time-consuming (Grant *et al.*, 2006) and local, so it requires many measurements to characterise an entire field (Jackson, 1982). For these reasons, direct methods of irrigation scheduling must be improved, and new methods investigated.

In this sense, canopy temperature (T_c) can be a viable alternative for irrigation scheduling (Poblete-Echeverria *et al.*, 2017; Stoll and Jones, 2007; Zhou *et al.*, 2021). It is well known that leaf temperature increases with increasing plant water stress. When no water is available in the root zone, transpiration will decrease

from the maximum potential, and plant temperature will increase (Idso *et al.*, 1981). Canopy and leaf temperature can be measured with non-contact infrared (IR) sensors and cameras which are non-destructive, instantaneous and can be applied at different scales. Satellites can provide temperature data of large areas at low resolution, while aerial vehicles such as drones can gather data of entire vineyards at a higher resolution. Handheld thermal cameras can be used to measure T_c at vine level with a sufficient resolution by simply changing measurement distance (Zhou *et al.*, 2021). This proximal method is cost effective and logistically simple to implement in the field. Some sensors (on all measurement scales) combine temperature data with normal images.

Although the use of various scales of IR measurements to determine plant water stress accurately has been widely studied, there are still some limitations and uncertainties, especially in regions with significant variability in the climate (Jones, 1999). The canopy temperature is not only affected by plant water stress, but also by several climatic and physiological conditions such as solar radiation, wind speed, ambient temperature, and humidity (Idso *et al.*, 1981; Petrie *et al.*, 2019; Poirier-Pocovi *et al.*, 2020). For this reason, thermal stress indexes are needed to compensate for the multiple effects by normalising the measurements to a particular temperature range. The thermal indexes allow the comparison between measurements taken on different days with different ambient conditions.

The investigation into accurate stress detection in vineyards using IR thermography is an important advancement, not only for precision viticulture, but for agriculture in general. An established canopy temperature measurement protocol will accelerate the implementation of this technology. The advances made in the technological field must be bridged to traditional agricultural practices. Results from this research can be applied to orchards planted in similar styles as vineyards, such as super high density olive orchards.

1.2 Motivation

Full knowledge and understanding of plant stress in vineyards can make a significant impact on water usage in viticulture. Irrigation is used to control water stress in vineyards, which must be finely managed, as it can produce desirable features in the wine that is ultimately produced. Fruit quality can be improved by a water deficit (Van Leeuwen *et al.*, 2009), but severe water deficit can reduce fruit quantity and quality and negatively influence the longevity of the grapevines (Pellegrino *et al.*, 2014). Farmers can use plant stress levels as an indicator of when to irrigate plants, as not to waste water. This is especially important in the drought-prone region of the Cape Winelands in South Africa, where the vines have to be irrigated in the hot, dry summer months.

Thermal imaging can replace the current destructive methods in practice. Measuring plant water stress is traditionally done per block and not repeated within a block, due to the limitations of the SWP measurements. The variability

within a block is difficult to determine with limited measurement points. With immediate canopy temperature measurements, IR sensors open the door to plant or region-based irrigation.

Improvements to irrigation scheduling can only be made with the simultaneous improvement of plant water status measurements. Plant water stress is a key factor in the field of precision agriculture, and specifically in precision viticulture. A robust, low-cost and easy-to-use measurement of plant water stress will advance irrigation scheduling in the field of precision viticulture, which will in turn increase yield and limit the environmental impact of vineyards.

Progress made in the field of thermal measurement in viticulture can easily be bridged to other agricultural fields. Apple and olive orchards, for example, are planted in a similar row structures to grapevines. The insight gained through this study will accelerate the adoption of IR plant water stress measurements in other agricultural fields.

1.3 Project statement and objectives

1.3.1 Problem statement

The general aim of this study is to improve the grapevine CWSI measurement techniques. To accomplish this, alternatives to manual measurements of CWSI reference temperatures must be investigated and physical canopy temperature measurement parameters must be established. This is required to ultimately compare low-cost sensors to commercial IR cameras for CWSI determination.

1.3.2 Objectives

This study has three main objectives with its respective goals:

Objective 1: Improve CWSI reference temperature measurement (Chapter 4)

(a) Select a baseline reference temperature measurement protocol.

(b) Compare and select automatic reference temperature methods.

(c) Compare measurements of the low-cost sensors to those of an IR camera.

Objective 2: Investigate hardware and physical requirements of canopy temperature measurements (Chapters 3 and 5)

(a) Calibrate the sensors that will be compared in the study.

(b) Investigate automatic analysis techniques of thermal images.

(c) Compare low-cost sensor canopy measurements to commercial IR camera measurements.

Objective 3: Determine the best conditions for CWSI measurements (Chapter 6)

(a) Determine the best measurement parameters for accurate CWSI measurement.

(b) Investigate whether the low-cost sensors can be used along with automatic reference temperature methods to determine CWSI.

Chapter 2

Literature Review

2.1 Introduction

CWSI is a relevant method of plant water stress measurement that is used in many crops. Mwinuka *et al.* (2021) used the CWSI to calculate plant water stress in eggplant and used it to predict the yield under deficit irrigation. Chandel *et al.* (2021) used multiple linear regression of CWSI and near infrared stress indexes to predict alfalfa yield (R2 = 0.64). Gonzalez-Dugo *et al.* (2020) indicates that CWSI measurement taken at noon is an good indicator of the water status of almond trees. The authors determined a good correlation ($r^2 = 0.91$) between CWSI and midday transpiration measurements.

Relevant background information with regard to infrared (IR) sensors is presented. Plant water stress physiology is discussed before the benefits and limitations of the crop water stress index (CWSI) are presented. State-of-the-art thermal plant water stress detection methods are discussed, and a summary of some of the most relevant research regarding the CWSI in grapevines is presented.

2.2 Infrared thermal imaging

2.2.1 Infrared energy

Energy is transferred from one surface to another through IR radiation. Radiation is emitted by every object above 0 K and has a wavelength between 0.75 µm and 100 µm. Small wavelength (high-frequency) radiation has more energy and is easily detectable by IR sensors. As IR transmission through the atmosphere depends strongly on radiation wavelength, bands of maximum transmission must be selected for the IR sensors (Minkina and Dudzik, 2009). IR wavelengths in the 1 µm to 5 µm and 8 µm to 14 µm spectrum have good atmospheric transmission at ground level (Kaplan, 2007), but the latter has the best transmission (Minkina and Dudzik, 2009), as presented in Figure 2.1. At long measurement distances (>10 m), the atmospheric transmission window starts slightly higher at about

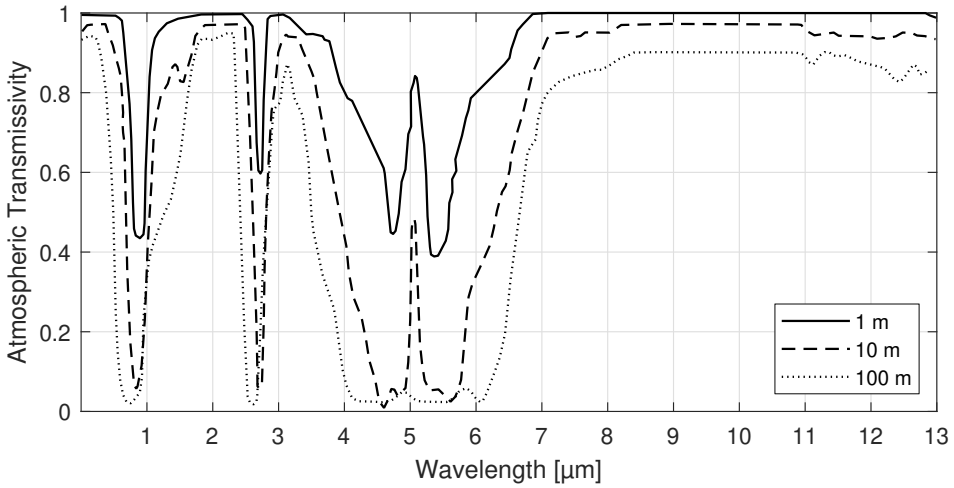

Figure 2.1. IR atmospheric transmissivity at different distances and wavelengths, digitised from Minkina and Dudzik (2009)

8.4 µm. In the 5 µm to 8 µm waveband, water vapour absorbs IR radiation, resulting in reduced IR transmissivity. Measurements taken in this band would be affected by humidity and measurement distance. In the 8 µm to 14 µm band, the atmospheric transmission is very good, especially at short distances. Loss of IR energy is negligible at short distances but the presence of water vapour in the air increases energy losses (Minkina and Dudzik, 2009).

2.2.2 Infrared sensors

A basic IR sensor schematic is presented in Figure 2.2. Lenses are required to focus the IR radiation from the sensor's field of view (FOV) to the detector. Glass is opaque to IR radiation at 10 µm and is not suitable for a lens as in a normal camera. Materials such as zinc selenide, sapphire and fused quartz have more uniform IR transmission properties and are suitable materials for IR lenses. A filter is placed in front of the detector to limit the electromagnetic waves to a specific IR band. The detector generates a voltage that is proportional to the objects in the FOV of the sensor.

Two main types of IR detectors exist. Photodetectors have limited spectral responses, fast response times and high sensitivities, but must be cooled for optimal performance. Thermal detectors which are typically used in commercial IR sensors and cameras can operate at room temperature, have uniform spectral responses but have lower response times and sensitivities. The electronics of thermal detectors compensate for the ambient temperature and factor in the emissivity of the target surface.

Thermography is a process by which an image of an object is created by displaying the object's temperature instead of its actual colour. Kaplan (2007) explains that IR plane focal array cameras employ a sensor array instead of a single

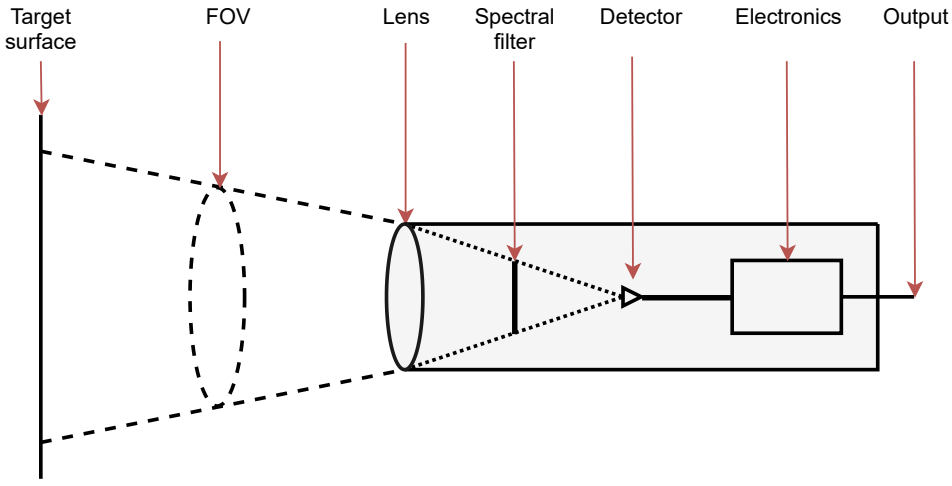

Figure 2.2. Components of thermal camera, adapted from Kaplan (2007)

sensor to generate a two-dimensional temperature grid of the FOV. The lens directs a region of IR radiation to an IR detector, similar to a pixel in a normal reg green blue (RGB) camera.

Commercial IR cameras record a RGB colour image as well as a matrix of temperature values. The display is often a pseudocolour temperature heat map with a superimposed layer of the edges detected from the RGB image. This allows the user to identify objects by shape, while visualising the associated temperature in colour.

A very wide range of IR sensors exists. It ranges from high-resolution IR cameras in satellites and drones to simple low-cost array or single-area sensors. These low-cost IR sensors have been successfully used in research (Noguera *et al.*, 2020; Drechsler *et al.*, 2019; Van Asbroeck, 2018), and may provide a feasible alternative to expensive IR thermal imagery.

Carrasco-Benavides *et al.* (2020) studied the influence of thermal infrared (TIR) resolution on CSWI performance in cherry trees. The authors found that the lower-resolution camera (60×80 pixels compared to 260×195 pixels) performed just as well as the high resolution camera. They recommend that the low-resolution camera be used as a cost effective and practical tool for assessing water stress in cherry trees.

2.2.3 Thermal infrared sensor calibration

To ensure accurate IR temperature measurement, the IR sensor must be calibrated to a known reference in the entire expected measurement range (Bower *et al.*, 2009). An accurate reference surface is a thermal cavity which approximates a blackbody surface (Bower *et al.*, 2009). Cetas (1978) constructed a thermal cavity with emissivity greater than 0.999 by drilling a cylindrical hole with a conical tip into an aluminium block and painting the inside velvet black ($\epsilon =$

0.975). Thermistors on the inside surface of the cavity reported the blackbody temperature. The blackbody temperature was controlled by heating or cooling the entire aluminium block.

Bower *et al.* (2009) identified the need for an accurate, cost-effective alternative blackbody calibration source and identified water as a suitable substance. Horwitz (1999) indicated that water is an ideal calibration source as its vapour phase does not absorb significant radiation at short path lengths, it is opaque in the liquid state and it has a high emissivity of 0.98.

Bower *et al.* (2009) used a water bath with recirculating water as a blackbody calibration source for IR sensors. By placing a thermistor probe directly under the water surface, the blackbody temperature was accurately measured. The authors indicated that heat transfer does occur as the water moves radially outward and evaporates from the measurement beaker. The authors corrected for this with heat transfer calculations, but found the error to be 0.19 °C at 30 °C and 2.02 °C at 66 °C. The authors concluded that the cost effective method provides accurate results in the temperature range of liquid water.

Minkina and Dudzik (2009) state that commercial IR sensor calibration is done by using a calibration curve in the form of

$$S_{\mathrm{i}} = \frac{B_1}{\exp \frac{B_2}{T_{\mathrm{i}}} - B_3} \tag{2.1}$$

where B_1, B_2 and B_3 are determined by best fit. S_{i} is the signal measured by the IR detector at target temperature T_{i}. The calibrated temperatures are then calculated as

$$T_{\mathrm{i}} = \frac{B_2}{\ln(\frac{B_1}{S_{\mathrm{i}}} + B_3)} \tag{2.2}$$

from the detector signal.

2.3 Plant physiology

2.3.1 Transpiration

A plant can regulate its temperature by evaporation of water through stomata in the leaves. Stomata are minute openings in leaves that control gas exchange. Stomatal conductance (g_{s}) is a measure of leaf transpiration. Water stress in plant is a result of insufficient moisture available in the root zone of the plant (Idso *et al.*, 1981). An increase in plant temperature due to a lack of water is a response to plant water stress, rather than an indicator of plant water stress. The water deficit leads to a closure in leaf stomata. As a result the plant's transpiration rate declines and the leaf temperature increases (Poblete-Echeverria *et al.*, 2017). Other variables such as humidity, atmospheric temperature, wind speed, and irradiance from the sun further influence the plant canopy temperature (Poblete-Echeverria *et al.*, 2017; Jones, 2018).

Thermal imaging can thus be used to estimate the level of plant water stress by measuring canopy temperature (Jones, 2002; Idso *et al.*, 1981). As thermal imaging operates outside of the visual spectrum, plant water stress can be detected before damage is visible and irreversible (Chaerle and Van Der Straeten, 2001).

2.3.2 Grapevine seasonal development

Grapevines are deciduous plants (losing their leaves every winter). The development of the vines undergoes several classifiable stages throughout each season. These stages are cultivar- and climate-dependent. EL scoring, developed by Eichhorn and Lorenz (1977) and refined by Coombe (1995), is an established method of identifying 47 stages of grapevine development.

The major stages are: (i) bud burst (4), where the first leaf tips become visible; (ii) 0.1 m Shoot length (12); (iii) Start of flowering (19); (iv) Flowering (17), where 50% caps are off; (v) Setting (27), where young berries enlarge >2 mm; (vi) Pea–sized berries (31) where berries are>17 mm diameter; (vii) Veraison (35)- berries begin to colour and enlarge; (viii) Harvest (38), where the berries are ripe.

Some authors such as Olivo *et al.* (2008) and Fernandes de Oliveira *et al.* (2021) use simpler major stages when dealing with water stress measurements. These are stage I, which is from the winter bud to fruit-set, stage II from fruit-set to veraison, and stage III, veraison to harvest. This simpler method will be used for the remainder of this document.

Shortly before or during the onset of berry ripening (or veraison), the shoots harden and turn from green to reddish or yellowish brown (Keller, 2015). Abundant nutrient and water supply may delay this process. The leaf canopy reaches its final size around this stage, after which it is trimmed to a height of around 2 m. Shoots are manually moved to be within the trellis.

2.3.3 Stress indexes

Canopy temperature T_c alone is not an accurate indicator of plant water stress, as the ambient temperature, which changes day by day, has a significant impact on T_c. This establishes the need for a parameter or index that normalises T_c to the climatic conditions at the time of measurement.

Idso *et al.* (1981) defines the CWSI as the normalised ratio between a non-stressed baseline temperature and a fully stressed baseline temperature. The use of normalised stress indexes allows for the comparison of plant stress values in different environmental conditions (Jones, 1999).

$$CWSI = \frac{T_c - T_{wet}}{T_{dry} - T_{wet}} \tag{2.3}$$

The canopy temperature is defined as the mean of the leaf temperature distribution (Fuchs, 1990). T_{wet} and T_{dry} are reference temperature values that repre-

sent the maximum and minimum possible temperatures reachable by the plant. These wet and dry temperatures are not to be confused with wet-bulb and dry-bulb temperatures. The maximum temperature is reached when no transpiration occurs, while the minimum temperature is achieved when the plants transpire at their maximum potential, as explained in Section 2.3.5.

Some authors such as Sepúlveda-Reyes *et al.* (2016), Alchanatis *et al.* (2009) and Moller *et al.* (2007) have attempted to use theoretical leaf energy balances for the calculation of the maximum and minimum leaf temperatures, but Poirier-Pocovi *et al.* (2020) indicate that one needs knowledge of complex parameters such as leaf resistance to convective heat transfer, slope of the saturation vapour pressure curve and the net radiation on the leaves. The authors further indicate that in practical applications it is difficult to provide these parameters without specialised expertise and costly apparatus. Alghory and Yazar (2018) suggest that it is infeasible to use theoretical values for the calculation of CWSI. Bellvert *et al.* (2014) and Cohen *et al.* (2005) modelled values for T_{wet} and T_{dry} based on an empirical value added to the ambient temperature (Poirier-Pocovi *et al.*, 2020).

The CWSI is non-linearly related to the rate of evaporation or stomatal conductance (Jones, 2018). Indexes that relate T_{c} to stomatal conductance index and air temperature have been investigated, but CWSI remains the most popular (Ihuoma and Madramootoo, 2017).

2.3.4 Sunlit and shaded side of canopy

Pou *et al.* (2014) suggested that there is no agreement on which side of the canopy measurements must be taken. Further research into this question has not provided consistent results.

Jones (2002) investigated which side of a grapevine provides the best correlation between T_{c} and stomatal conductance. He found that the temperature variation on the sunlit side is greater than on the shaded side. The different angles of incidence for radiance from the sun on the leaves, and the visibility of shaded leaves from the sunlit side is responsible for the large variation in temperatures. The large temperature variation complicates the process of calculating a representative canopy temperature. Jones (2018) explains that the sunlit side of the canopy, due to the higher temperature, has a greater response in stomatal conductance. The shaded side of a single canopy has less temperature variation as leaf orientations have a much smaller effect on the leaf energy balance.

Petrie *et al.* (2019) found that the shaded side of the grapevine provided a good correlation ($r^2 = 0.61$) between CWSI and stem water potential (SWP), which is an accurate measurement of plant water stress, discussed in Section 2.5.3. Similarly, Gutiérrez *et al.* (2021) found that the shaded side performed better than the sunlit side. The use of the shaded side of the canopy mitigated the effects of clouds passing and affecting the leaf energy balance as a result of the changing radiation. The authors further found that the relationship between SWP and

CWSI were best described with a curvilinear fit, as other authors such as Ru *et al.* (2020) have also found.

Pou *et al.* (2014) conducted a comprehensive study on the correlation between canopy temperature and stomatal conductance in grapevines. The authors found that midday, shaded measurements represent the best correlation between canopy temperature and stomatal conductance.

Poirier-Pocovi *et al.* (2020) explain that in shaded canopies, the canopy temperature and CWSI reference temperatures are dominated by air temperature. Poirier-Pocovi *et al.* (2020) recommend that sunny conditions are necessary to capture the effects of plant water stress as canopy temperature is more sensitive to stomatal conductance under these conditions.

2.3.5 Reference temperatures

The required CWSI reference temperatures for equation 2.3 are an obstacle to the adoption of the method. Petrie *et al.* (2019) stated that the requirements for the use of reference surfaces makes it unlikely that the technology will be appealing to growers.

Jones (1999) found that a leaf wetted on both sides with soapy water is a good reference surface for the non-stressed temperature T_{wet}. The authors further found that a leaf covered on both sides with a thin coating of petroleum jelly (Vaseline) is an accurate reference for T_{dry}, as it prevents transpiration. It is suggested that the average of reference measurements before and after each target plant must be taken into account for changes in weather conditions. Jones (2002) indicates that about one minute must pass before measuring the reference leaves for the new steady state temperature to be reached. This method is the standard for measuring the reference temperatures, but it is notoriously tedious and inconvenient to use. This method is referred to throughout this document as the 'Natural method' (N) . Jones (2002) and Jones (1999) found that real leaves provide the best reference surface as they possess similar aerodynamic and radiometric properties to the canopy being studied, assuming that the orientations relative to the sun are similar. Artificial reference surfaces were tested by Jones (1999), but real leaves were found to have a time constant similar to that of the canopy.

Poirier-Pocovi *et al.* (2020) claim that it is impractical to measure reference temperatures and emphasises the need for better reference surfaces. One such example is the use of the standard deviation in the temperature of the thermal image. Noguera *et al.* (2020) uses adaptable temperature thresholds as

$$T_{\text{wet}} = T_{\text{c}} - 2\sigma \tag{2.4a}$$

$$T_{\text{dry}} = T_{\text{c}} + 2\sigma \tag{2.4b}$$

where σ is the standard deviation determined from the histogram of the entire set of thermal images for a measurement day. He explains that this approach

relies on the need for a diverse range of stress values in the set, which might not be available if all plants measured are under water stress. His technique does, however, allow for automation of data analysis without the need for time-consuming reference measurements. Sepúlveda-Reyes *et al.* (2016) used a similar technique, and determined the amount of standard deviations by using the standard method developed by Jones (1999) as a reference.

Grant *et al.* (2006) suggests using fully irrigated and non-irrigated plants as reference temperatures, while Poirier-Pocovi *et al.* (2020) argue that it is rarely possible to have access to both a non-transpiring and fully transpiring leaf under similar environmental conditions.

Jones (2002) found that reference surfaces are affected by the water status of the vine, more so for the dry reference than the wet. The author explained that the plant water status has a measurable impact on the canopy microclimate. This encourages the use of detached leaves as they are independent of the canopy and can be used on the entire block, if maintained at a consistent angle to the sun. In another study Jones (2002) found, by comparing thermocouple measurements to IR measurements, that the application of substances to the leaf affects its emissivity. He reported an emissivity error of approximately 0.008.

Petrie *et al.* (2019) investigated the use of artificial reference surfaces (terry-cloth fabric coated similar to T_{wet} and T_{dry} leaves) and found that the fabric was 2 K warmer than the normal T_{dry}. An uncoated, separated leaf averaged around 0.6 K warmer than the normal T_{dry}. These reference surfaces were tested in shaded conditions. The wetted fabric proved to have a more stable temperature than the wetted leaf. The authors of the study make no recommendation of which surface to use.

2.4 Leaf energy balance

2.4.1 CWSI in terms of VPD

Idso *et al.* (1981) found a negative linear correlation between the difference in canopy and ambient temperature ($T_c - T_a$), and vapour pressure deficit (VPD), for non-stressed or fully transpiring plants. As the VPD increases, a greater potential exists for a plant to lower its temperature below the ambient temperature. This linear trend is used as a non-stressed baseline for maximum possible plant transpiration at a given VPD. As less water becomes available to the plant, or when the plant cannot transpire at the maximum potential rate, ($T_c - T_a$) will be above the baseline at that specific VPD.

The authors found that the baseline intercepts the zero VPD axis at a positive value for ($T_c - T_a$), as shown in Figure 2.3. This implies that when no transpiration occurs, T_c will be at a higher temperature than T_a. Solar radiation can raise the canopy temperature above the ambient temperature. The stressed baseline must therefore be above the point where the non-stressed baseline intercepts the

y axis. To determine a good estimate of the stressed baseline, the authors suggest the following:

Take the horizontal distance between the intercept of the non-stressed baseline and the $T_c - T_a = 0$ line, labelled as a in Figure 2.3. Move the distance a to the negative region of VPD from the zero point. The $(T_c - T_a)$ value where this negative VPD value intersects the non-stressed baseline can be taken as the stressed baseline.

CWSI is then calculated as

$$CWSI = \frac{(T_c - T_a) - (T_c - T_a)_{lb}}{(T_c - T_a)_{ub} - (T_c - T_a)_{lb}} \tag{2.5}$$

with lb denoting the lower or non-stressed baseline and ub denoting the upper or stressed baseline. These baseline values are indicated on Figure 2.3 for values corresponding to the VPD measured at the time of measuring $(T_c - T_a)$.

The CWSI of point X in Figure 2.3 can be visually estimated as the ratio of the vertical distance between X and the non-stressed baseline below the point and the vertical distance between the stressed baseline and the non-stressed baseline below the X. In the example, CWSI = 0.4. The CWSI calculated here is the ratio of evapotranspiration to maximum potential evapotranspiration.

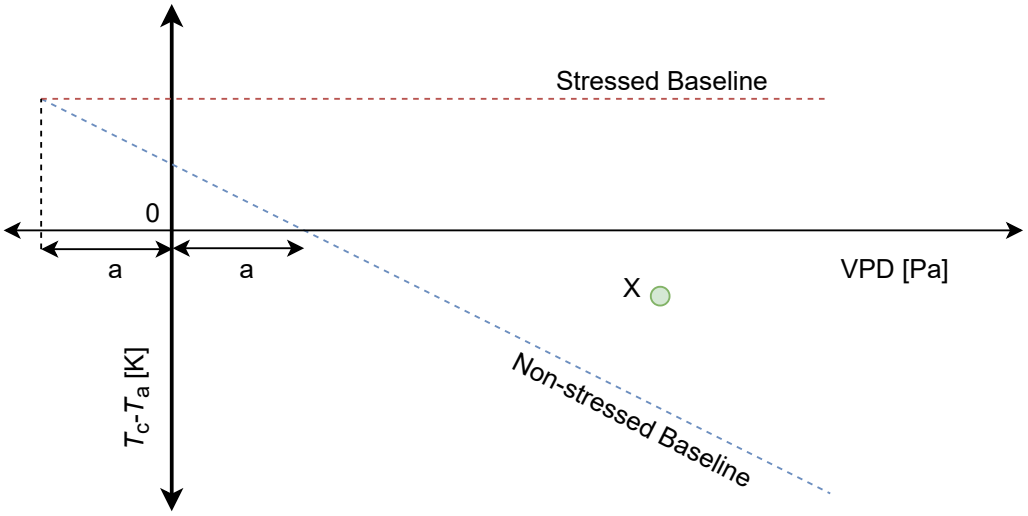

Figure 2.3. Plant-air temperature difference vs VPD

Jones (2018) explains that this approach does not perform well in humid climates, as variation in VPD is a driving force for the evaporation. Another drawback is the need to define the non-stressed baseline over a wide range of VPD. A plant must therefore be maintained at a non-stressed level for an entire season before the model can be used. This approach was developed for homogenous crops such as lucerne. The method does not account for changes in wind speed and irradiance.

Table 2.1. Resistance terms in reference surface equations

Resistance	Description	Equation	Reference
r_{HR}	Parallel resistance to heat and radiative transfer	$(r_H r_R)/(r_H + r_R)$	(Guilioni *et al.*, 2008)
$r_{l,V}$	Leaf resistance to water vapour transfer that is mainly dependent on stomatal resistance	$0.92 r_{b,H}$	(Guilioni *et al.*, 2008)
$r_{b,V}$	Boundary layer resistance to water vapour transport	$0.92 r_{b,H}$	Jones (2014)
r_H	Leaf boundary layer resistance to convective heat transfer	$100\sqrt{L_c/V}$	Jones (2014)
r_R	Leaf resistance to radiative heat transfer	$(\rho c_p)/(8\epsilon\sigma T_a^4)$	(Guilioni *et al.*, 2008)

Note: Subscripts b and l refer to boundary layer and leaf respectively. Subscripts R and H refer to radiative and convective heat transfer respectively. Subscript V refers to water vapour transfer.

2.4.2 Theoretical wet and dry reference temperatures

The standard equation for a leaf energy balance,

$$T_l - T_a = \frac{r_{HR}(r_{b,V} + r_{l,V})\gamma R_N}{\rho c_p(\gamma(r_{b,V} + r_{l,V}) + \Delta r_{HR})} - \frac{r_{HR}\delta_e}{\gamma(r_{b,V} + r_{l,V}) + \Delta r_{HR}} \tag{2.6}$$

given by Jones (2014), can be rearranged to provide theoretical values for reference leaf temperatures. The resistance terms are calculated as explained in Table 2.1 and T_l is leaf temperature. The resistance to heat and water vapour transfer have units s/m which is the reciprocal of the conductance unit typically used in plant physiology.

If all the terms related to evaporative cooling are omitted, the dry reference surface will equal the net isothermal radiation Jones (1999). T_{dry} is subsequently calculated as

$$T_{dry} = T_a + \frac{r_{HR} R_N}{\rho c_p} \tag{2.7}$$

By setting the leaf resistance to water vapour transfer ($r_{l,V}$) equal to zero, the wet surface temperature can be calculated as

$$T_{wet} = T_a + \frac{r_{HR} r_{b,V} \gamma R_N}{\rho c_p(\gamma r_{b,V} + \Delta r_{HR})} - \frac{r_{HR}\delta_e}{\gamma r_{b,V} + \Delta r_{HR}} \tag{2.8}$$

2.5 Plant water stress measurements

The importance of water stress measurements in vineyards have been emphasized. In order do evaluate IR thermal plant water stress measurements, a suit-

able reference water stress measurement must be used. Plant water stress measurements can be soil-, atmosphere- or plant based. A brief overview of the different methodologies is presented.

2.5.1 Soil-based

Soil-based methods directly measure the moisture in soil that is available to the plants. These techniques can measure soil capillary tension, soil electrical conductivity or absorption of radiation by moisture in the soil. Vineyards with diverse soil properties may require multiple sensors to capture the spacial variability. Varying depth of roots and inconsistent vertical soil water distribution can lead to measurements that do not reflect the vines' water status (Rienth and Scholasch, 2019).

2.5.2 Atmosphere based

By determining vineyard evapotranspiration, plant water consumption can be estimated. Evapotranspiration is calculated by performing a total energy balance on the net radiation, sensible heat exchange to the surrounding air and radiation heat exchange from the soil to the canopy. The latent heat flux density is then calculated to determine the amount of water transpired by the plants. Rienth and Scholasch (2019) indicate that atmosphere based methods are promising, but that the measurement of the subsensible heat exchange is complicated.

2.5.3 Plant-based

Plant-based measurements of water stress can provide a direct indication of the plant's current condition. Direct methods are more involved and difficult to automate, but provide more accurate plant water stress measurements.

Stomatal conductance

Measurement of plant stomatal conductance (g_s) is a suitable method of detecting the level of water deficit in a plant (Rienth and Scholasch, 2019). Porometers can be used to measure and H_2O diffusion from a leaf, while IR gas analysers can measure both H_2O and CO_2. The equipment is complex to use, expensive and requires frequent calibration (Rienth and Scholasch, 2019). It is not suitable for large scale measurements in a vineyard, but can provide accurate plant water stress measurements.

Water potential

In plants, water moves from root to leaves through tubes called xylem. Water is absorbed in the roots and transpiration occurs at the leaves. The transpiration

Figure 2.4. Pressure chamber used to measure SWP

Figure 2.5. Leaf in foil covered plastic bag

creates negative pressure, forcing the water from the roots, through the stem and shoots to the leaves. If more water is lost than is absorbed by the roots, the plant is under water stress and it has a high water stress potential.

Water potential is measured using a pressure chamber with an inert gas such as Nitrogen. A pressure chamber is presented in Figure 2.4 with a schematic in Figure 2.6. A leaf is placed inside a pressure chamber with the petiole (leaf stem) on the outside. A rubber seal ensures a tight seal around the petiole. The pressure in the chamber is increased until water is seen to bubble out of the stem. The pressure at this moment is recorded as the water potential. Water potential is often reported as a negative value since it relates to the tension required to move water from the roots to the leaves.

Rienth and Scholasch (2019) indicate that plant and soil come into equilibrium overnight, as maximum water potential is reached predawn (Améglio *et al.*, 2021; Klepper, 1968). Predawn water potential has been shown to correlate well to grapevines in a mild stress condition ($gs > 0.15\,\text{mol}\,H_2O\,m^2/s$) (Poblete-Echeverria *et al.*, 2019). At this time, plant water status and soil water content are in equilibrium (Choné *et al.*, 2001). Predawn water potential is measured just before sunrise and is a good indication of soil water content.

At dawn, the leaves start transpiring and the water deficit recovers, with a minimum water potential (maximum water stress) reached around noon. SWP is measured on leaves to determine the level of water stress in the plant. Covering a leaf with a foil-covered plastic bag prevents transpiration and photosynthesis. The covered leaf's water potential is in equilibrium to that of the plant stem (Choné *et al.*, 2001). After the leaf has been enclosed in a foil-covered plastic bag, as shown in Figure 2.5, for at least an hour, it is cut off with a sharp blade. Choné *et al.* (2001) found that there is no significant difference between enclosing the leaf 1 hour, 2 hours or 6 hours before taking the measurement. The authors further found that the vertical position of the leaf in a mechanically pruned canopy has a negligible effect on the SWP.

Leaf water potential (LWP) is an alternative to SWP that is preferred by some,

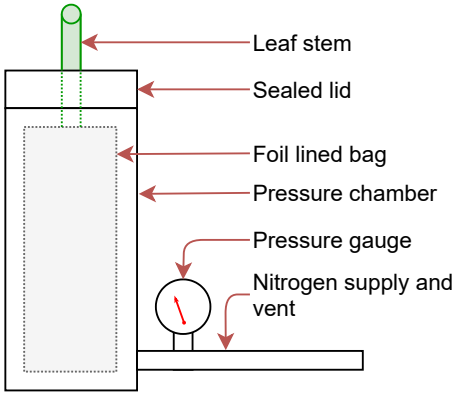

Figure 2.6. Pressure chamber schematic

Table 2.2. Ranges of SWP relating to grapevine water status (Leeuwen *et al.*, 2009)

Water status	SWP range (MPa)
No water deficit	>-0.6
Weak water deficit	-0.6 to -0.9
Weak to moderate water deficit	-0.9 to -1.1
Moderate to severe water deficit	-1.1 to -1.4
Severe water deficit	<-1.4

such as Bellvert *et al.* (2014). The procedure and equipment used is similar to that of SWP, but the leaves are not covered before measurement. Leaf water potential gives the instantaneous stress value, on which the current transpiration has an effect. Bellvert *et al.* (2014) successfully correlated LWP to CWSI.

SWP is the standard method of measuring plant water stress (Grant *et al.*, 2006). Midday SWP has been shown to be highly correlated to transpiration rates in vineyards (Choné *et al.*, 2001). Poblete-Echeverria *et al.* (2019) compared predawn-, leaf- and stem water potential in calculating water stress classes determined with g_s measurements. The authors found that SWP is the best water stress indicator for grapevines under severe water stress. SWP will thus be used as the baseline water stress measurement in this study, as grapevines are often maintained in a narrow window of high water stress for improved wine quality. SWP ranges with the corresponding levels of plant water stress is presented in Table 2.2.

It can be difficult to see the small drop of water forced out of the petiole and it is recommended that a magnifying glass is used. This can lead to different operators reporting different values for the SWP. The pressure chamber and gas canister are heavy and difficult to move around. Petrie *et al.* (2019) argues that operator safety and operator bias are limitations to the commercial application of SWP. SWP is thus an impractical method of measuring water stress variability in an entire vineyard as it is time-consuming and destructive.

2.6 Thermal imaging in vineyards

Pineda *et al.* (2020) summarised issues relating to stress measurement with IR as follows: (i) The number of plants measured at the same time is limited; (ii) Atmospheric conditions such as clouds and wind can skew results and prohibit measurements. An automatic irrigation system will need additional weather information, such as cloud cover, rain and wind speed, as CWSI methods are developed for clear, sunny days; (iii) Accuracy and sensitivity of IR sensors must be taken into account when analysing results; (iv) There is a need for accurate complementary measurements (ambient temperature, humidity and wind speed); (v) The time of measurements or time between measurements can have an effect on results; (vi) Biotic stressors such as pathogens may affect plant temperature. The authors conclude that stress indexes, rather than canopy temperatures, are a good indication for plant stress as they can counteract the ambient conditions of the measurement.

In addition to all these drawbacks to the use of thermal imaging in vineyards, Bellvert *et al.* (2014) recommends that the different phenological stage as well as grape cultivar must be taken into account when using CWSI for irrigation scheduling. Fernandes de Oliveira *et al.* (2021) explains that main shoot lignification increases as the phenological stages progresses, which has an effect on the thermal response of the grapevines.

Measurement scale

Thermal imagery can be obtained by satellite, unmanned areal vehicle (UAV) or ground-based systems. Thermal images acquired from satellite images and UAVs allow for rapid data acquisition with the limitation of resolution, as several square metres are often captured by a single satellite image pixel (Gutiérrez *et al.*, 2018). Carrasco-Benavides *et al.* (2020) found that higher resolution ground-based IR cameras did not provide a better estimation of CWSI in cherry trees.

Research done on UAV or satellite-based thermal imaging is not directly applicable to the ground-based systems, as the top of the canopy is measured and not the side. Grant *et al.* (2006) suggests that handheld proximal thermography is suitable for grapevines as the vertical structure of the vines is suited for measurement along the rows.

Jones (2002) indicates that automated image analysis and correction may be more suitable for homogenous crops such as wheat than for row crops such as grapevines. Prueger *et al.* (2018) indicates that there is a considerable need for a suitable method to measure plant water stress on a large scale using IR measurements.

Standardisation

Pineda *et al.* (2020) indicate that there is a need for a system of standardisation for the collection and sharing of data relating to IR measurements in crops. The correlation values obtained by different studies vary as the capture and data processing of thermal images are not standardised (Carrasco-Benavides *et al.*, 2020). The best measurement distance, time of day and canopy side are examples of parameters which are not consistent in literature. The selection of the best measurement parameters is one of the main aims of this study.

Canopy background

In the context of thermal imaging in vineyards, all forms of IR imagery capture non-leaf material such as soil, sky and vines in the neighbouring rows. When measuring the canopy temperature, it is inevitable that background temperatures are measured through gaps in the canopy. Giuliani and Flore (2000) placed large black polyethylene sheets behind apple trees when measuring the canopy temperature. The sheets would heat up to a considerable temperature above the canopy temperature and so temperature thresholding was used to eliminate the background temperatures.

Microclimate

The microclimate is the atmospheric conditions at plant level that directly affect the plant. Wind speed negatively affects CWSI accuracy as rapid changes in the leaves' stomatal conductance influences the transpiration and in turn the leaf temperature (Jones, 1999). Likewise, low VPD as a result of low ambient temperature and high relative humidity, influences the accuracy of CWSI (Jones, 1999).

2.7 Modelling

2.7.1 CWSI sensitivity analysis

Poirier-Pocovi *et al.* (2020) developed a mathematical leaf temperature model, based on the leaf energy balance equation, to investigate the effects of air temperature, humidity, wind speed and radiation on stress indexes. The authors used the surface energy balance model developed by Campbell and Norman (1998), which takes radiation, convection and latent cooling fluxes into account. By setting the latent term equal to zero, T_{dry} is calculated. For T_{wet}, the stomatal resistance was eliminated to simulate a wet leaf.

Poirier-Pocovi *et al.* (2020) investigated the sensitivity of many stress indexes and CWSI in the 1-CWSI form. The goal of the analysis was to determine which environmental conditions the CWSI is sensitive to in comparison with stomatal conductance (which is plant water stress dependent). It was determined that

CWSI, under sunny conditions, is most sensitive to wind speed and stomatal conductance. This makes sense as the boundary layer conductance of a leaf is dependent on g_s and wind to control the water flux. Most importantly, CWSI was found to perform poorly in shaded conditions, being more sensitive to environmental conditions than to the stomatal conductance.

2.7.2 Modern Methods

Kumar *et al.* (2020) used artificial neural network modelling, specifically an unsupervised Kohonen self organising map and a supervised Feed-Forward Back Propagation, to predict CWSI of Indian mustard. The model only uses T_c, T_a and relative humidity (ϕ) as input variables. The model achieved a correlation of $r^2 = 0.97$ and $r^2 = 0.96$ to the baseline CWSI during training and evaluation respectively. The model was trained on data from 2017 and evaluated with data from the following year. The baseline CWSI was determined by measuring T_c with a single-area IR sensor, and by estimating T_{wet} and T_{dry} from well-watered and water-deficit irrigated plants.

King and Shellie (2016) developed a neural network model to predict the temperature of well-watered vineyards using weather station data (wind speed, air temperature, relative humidity and solar radiation). The model produced a correlation coefficient of $r^2 = 0.93$ between predicted and measured Syrah canopy temperatures. Cultivar-specific CWSI reference values were also predicted with neural network modelling. By using the neural network the authors could easily determine the CWSI by doing only physical measurements of canopy temperature. The authors explain that neural networks are well suited to predict reference temperatures as their relationship with environmental conditions and vine response is poorly understood and difficult to calculate mathematically.

A drawback of these neural network methods is that a lot of data is required to train and validate the models. The models find numeric correlations between the variable without taking the relevant physics into consideration. These models are, however, very accurate in determining CWSI directly from T_c and weather station measurements, eliminating the need for reference temperature measurements.

2.8 Studies done on CWSI and plant stress

Numerous studies have been done on the correlation between CWSI and plant stress in vineyards. In these studies, different sensors and methods are used. A summary is given in Table 2.3.

Table 2.3. Relevant grapevine CWSI research

Reference	Canopy side	Time of day	Distance [m]	Reference stress measurement	CWSI Reference surface	Best r^2	Comments
Sepúlveda-Reyes *et al.* (2016)	Shade	14:00–16:00	1.5	SWP	σ	0.46	Found that a constant multiple of the standard deviation (σ) of T_c can be used to estimate T_{wet} and T_{dry}.
Sepúlveda-Reyes *et al.* (2016)	Shade	14:00–16:00	1.5	g_s	LEB	0.51	Good correlations between CWSI and g_s were found using the LEB for reference temperatures.
Sepúlveda-Reyes *et al.* (2016)	Top	13:00–13:30	1.5	SWP	σ	0.36	Used a constant multiple of the standard deviation of UAV thermal images for reference temperatures.
King and Shellie (2016)	Sunny	13:00–15:00	0.15–0.30	LWP	Neural network	0.64	Validated and implemented an automatic remote calculation of CWSI for irrigation scheduling.
Gutiérrez *et al.* (2018)	Sunny	14:00–15:00	1.2	SWP	Artificial reference	0.71	Used a thermal camera attached to an all-terrain vehicle.
Matese *et al.* (2018)	Top	11:00–12:00	70	Net photosynthesis	Jones	0.64	Used UAV IR images.
Petrie *et al.* (2019)	Shaded	12:00–15:00	1.5	SWP	Artificial reference	0.61	Compared different reference surfaces.
Camacho-Alonso *et al.* (2017)	Shaded	08:00, 12:00, 16:00	Unspecified	SWP	Empirical and wetted cloth	0.64	Found different correlations between SWP and CWSI at different stages in the season.

2.9 Discussion

A substantial amount of research into IR measurement of canopy temperature has been done in recent years, especially in precision viticulture. Nevertheless, no standard practises with regards to measurement parameters are applied. For example, measurement distance, time of day, side of canopy, canopy background and sensor types vary considerably between studies, as seen in Table 2.3. Baseline plant water stress measurements are also not kept consistent, the two major methods being SWP and stomatal conductance. A need for a set of guidelines for accurately and repeatedly measuring CWSI in vineyards is identified.

A major point of incoherence in literature is the implementation of the T_{wet} and T_{dry} measurements for CWSI. Methods include covering the leaves with substances, using alternative materials, calculating energy balances, and implementing machine learning models to estimate the reference temperatures. Many of these methods use empirical correlations and heat transfer analyses on the leaves are not implemented. Researchers report that the need for reference temperatures is an hindrance to the adoption of CWSI as a commercial plant water stress measurement technique. There is a clear need for an automatic reference temperature calculation.

Finally, the use of IR sensors is not standardised in literature. Sensors vary from low-cost single-area sensors to expensive research grade thermal cameras that provide RGB and thermal images. The level of accuracy required by the different sensors is unknown.

IR temperature measurements have the potential to improve plant water stress measurements. Measurements are quick non-destructive. Research into the measurement parameters, sensor requirements and reference temperatures will aid in the commercial implementation of the technology.

Chapter 3

Hardware

3.1 Introduction

Literature shows that various infrared (IR) thermal sensors have been used for the study of vineyard canopy temperature. These sensors range from research-grade thermal cameras to low-cost single-area sensors connected to a microcontroller. Even though all these sensors calculate temperature by measuring IR radiation, their utility and accuracy vary significantly. Array-type sensors (with or without accompanying red-green-blue (RGB) cameras) allow the user to select regions of interest in a thermal image, while single-area sensors provide a weighted average temperature of an entire measurement area.

In this chapter, the sensors that were used in this study are introduced. The different sensors' fields of view (FOVs), accuracies and implementations are explained. Lastly, the sensor calibration procedure, used to ensure that the sensors measure similar temperatures in the expected measurement range, is provided.

3.2 Infrared sensors

Three main IR sensor types were considered for this study: (i) Commercial IR sensor arrays with integrated cameras; (ii) Low-cost, low-resolution IR array sensors; (iii) Low-cost, single-area sensors. The array type sensors are used for thermography, as it produces image-like data, while the single point sensors are used for thermometry. A summary of the different IR sensors used in this study is presented in Table 3.1. The relative costs are in relation to the Flir C3 which costs R10 700 (about $720). The indicated costs of the MLX90614 and AMG8833 sensors do not include the required microcontroller and screen, which have a combined relative price of 0.11. The Apogee sensor's relative cost does not include the data logger with a relative cost of 3.1.

To accurately calculate temperature from an IR measurement, the sources of the radiation must be taken into account. IR radiation detected by a sensor is the sum of IR radiation emitted by the target surface, the atmosphere between the

Table 3.1. IR sensors used in this study

Code	Sensor	Type	Accuracy [K]	Pixels	FOV	Relative Price
C3	Flir* C3	IR array with RGB camera	2	60 × 80	40° × 31°	1
F1	Flir One Pro	IR array with RGB camera	3	160 × 120	50° × 43°	0.6
IR12	Melexis† MLX90614 DCH	Single-area	0.3	-	12° cone	0.05
IR35	Melexis MLX90614 BCC	Single-area	0.5	-	35° cone	0.04
IR90	Melexis MLX90614 BAA	Single-area	0.5	-	90° cone	0.02
IR_Arr	Panasonic‡ AMG8833	IR Array	3	8 × 8	60° × 60°	0.09
Apogee	Apogee§ SI-1H1-SS	Single-area	0.2	-	64° × 13°	1.2

*FLIR Systems, Wilsonville, OR, USA. † Melexis, Ypres, Belgium. ‡ Panasonic Corporation of North America, Newark, NJ, USA. § Apogee instruments, Inc., Logan, Utah, USA. Relative costs are in relation to the R10 700 cost of the Flir C3.

target object and the detector and the IR radiation reflected off the target surface. The calculation procedure for accounting for these sources of IR radiation is presented in Appendix A.2.

3.2.1 Commercial thermal imaging cameras

Two commercial IR cameras were considered for this study. The Flir C3 is a standalone thermal camera and the Flir One Pro is attached to, and interfaces with, a smartphone. The lower cost of the latter is achieved by using the smartphone's screen and processor. Both these IR cameras record RGB images which are used to superimpose edge-detected lines on the thermal images for object recognition. An example of these edges is presented in Figure 3.4.

The Flir C3 and One Pro have RGB resolutions of 240×320 pixels and 480 × 640 pixels respectively and the respective spectral ranges are 7.5 µm to 14 µm and 8 µm to 14 µm (Flir, 2016, 2018). Both sensors have a thermal sensitivity of 0.1 K.

To obtain an accurate temperature measurement with the Flir cameras, the ambient and reflected temperatures, emissivity, distance and relative humidity must be taken into account. These parameters were used to calculate temperature from the radiometric data files created by these cameras. A modified version of the R package Thermimage developed by Glenn (2017) was used. The Flir Tools software only allows manual entry of these parameters, while Thermimage was

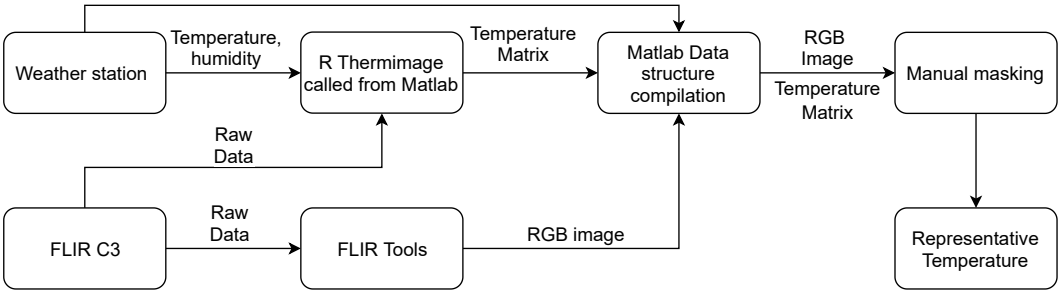

Figure 3.1. Flir temperature calculation flow diagram

called from a Matlab program which automatically specifies the measurement conditions (saved in a data structure) required for the temperature calculation.

Reflected temperature can be determined by measuring the temperature of a crumpled piece of aluminium foil placed in the same orientation as the target object with an emissivity set to 1 (Jones, 2002). As aluminium has a very high reflectivity, its apparent temperature measured by an IR sensor is predominantly determined by the reflected IR radiation of the surroundings. At the experimental site, ambient temperature and humidity are collected by a weather station. Bulk RGB image extraction from the Flir files was done with the standard Flir Tools software. A data flow pipeline for the calculation of a representative temperature from a Flir measurement is presented in Figure 3.1. The pipeline contains an image-masking step, where the user selects a region of interest (ROI) on the RGB image, from which the average temperature is calculated.

3.2.2 Low-cost sensor measurement rig

The IR35 and IR90 Melexis single-area sensors have a spectral range of 5.5 µm to 14 µm (Melexis, 2019). The spectral range of the IR_Arr sensor is 5 µm to 13 µm. The IR12 sensor has an uncoated silicone lens with a spectral range of 2 µm to 14 µm (Melexis, 2019).

The IR12, IR35, IR90 and IR_Arr sensors were connected to the same Teensy 3.6 microcontroller for data capture. The microcontroller was powered with a 20 000 mAh power bank. Schematics for the controller can be found in Appendix C. The battery and electronics are housed in an ABS plastic enclosure, with viewing ports for the various sensors as seen in Figure 3.3. This measurement rig (MR), houses the various sensors and simultaneously measures all the sensor temperatures. Initially, a DHT22 temperature and humidity sensor was connected to the MR, but the sensor proved unreliable and it was decided to gather this data from a local weather station instead.

The single-area sensors capture the entire area in their FOV and report a weighted average temperature as shown in Figure 3.2. These sensors weigh the central part of the canopy higher than the outer edges. The weighing is not determined computationally, but is due to the IR lens geometry.

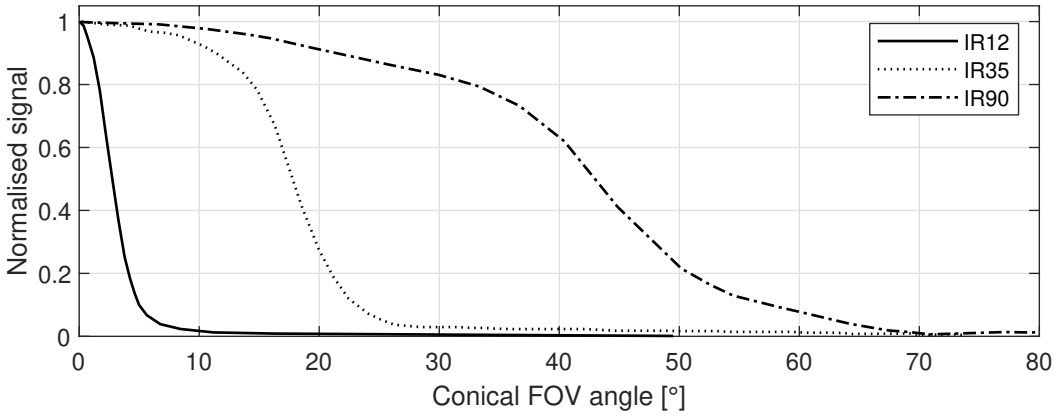

Figure 3.2. Weighting of low-cost sensor field of view, rotated around the central axis. The values for the figures were obtained by graphically digitising the different figures from the sensor data sheets.

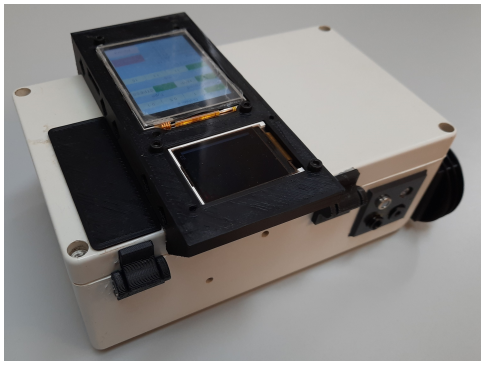

Figure 3.3. Measurement Rig housing sensors and screen

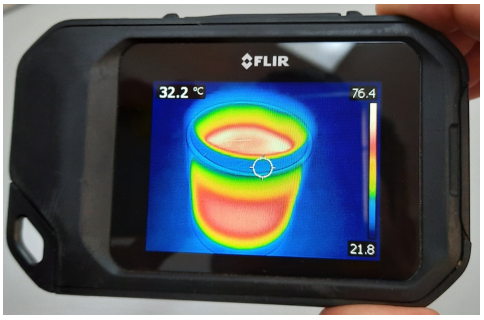

Figure 3.4. Flir C3 thermal image of a coffee mug

A 128×160 pixel LCD screen was used to display the output of the array sensor at 2 Hz. As all the sensors were aligned, the array sensor output was used to aim all of the sensors at the target surfaces. A 2.8 inch Nextion touch screen display was used to input the measurement numbers or measurement configuration that serves as a measurement ID. A simple user interface was created to allow a user to view all the sensor temperatures, turn the sensors on and off and to create logging files. A save button on the screen saves the sensor and measurement time data to an SD card inserted in the microcontroller. The user interface is provided in Appendix C.

3.3 Sensor calibration

3.3.1 Introduction

As different sensors' temperatures are compared in this study, it is important to ensure that these sensors report the same temperatures. The purpose of the experiment is to calibrate a variety of IR sensors for use in vineyard canopy temperature measurements. The calibration range must exceed the entire expected measurement range in the vineyard. The results from Chapter 5 indicate that canopy temperatures are in the 20 °C to 40 °C range. This experiment will cover the range of 10 °C to 50 °C.

This calibration procedure is based on Bower *et al.* (2009) which avoids the use of expensive equipment while ensuring accuracy. Bower *et al.* (2009) uses a thermistor under the surface of the water as a reference temperature and corrects for evaporative cooling with heat transfer calculations. The approach used in this study uses an accurate, calibrated IR sensor as reference temperature.

As the raw detector signals are not available with some commercial sensors, and the measurement range is narrow, a simple linear calibration curve is used in this study.

3.3.2 Experimental setup

The Apogee sensor is laboratory calibrated to 0.127 K uncertainty (95% confidence) in the −30 °C to 65 °C range and was used as a reference temperature measurement. The Apogee IR sensor was connected to a computer via a Campbell Scientific data logger. The emissivity was set to 0.98 for the Apogee and all the sensors.

A schematic of the setup is presented in Figure 3.5. A 5 l glass beaker was placed within a temperature-controlled water bath. The water bath circulated the water in the bottom compartment. Water was pumped by means of an aquarium pump, from the water bath to the glass beaker where it passed through a diffuser before flowing to the top surface. The beaker was levelled so that water overflowed around the top surface. This ensured that the water temperature along the entire top surface was nearly uniform. This double-bath method provided a smooth water surface at the top of the glass beaker that was measured with the different IR sensors. To ensure that the water surface filled the entire FOV of all the sensors, they were fixed to tripods close to the water surface.

The setup had to accommodate various sensor FOVs, ranging from a 12° conical to a square 60° × 60° FOV. Only a portion of the IR cameras' FOVs needed to capture the water surface, as the representative region could be selected from the data based on the RGB image.

Starting with refrigerated water at about 8 °C, the water temperature was measured by all of the sensors before increasing the temperature of the water bath by 5 °C. The next measurement was taken after the temperature had stabilised at

the desired temperature. A real-time graph of the Apogee sensor was used to determine when the temperature of the water had stabilised. This process was repeated until the water reached 50 °C. This calibration procedure was repeated on another day to ensure that the results were consistent.

3.3.3 Results and discussion

The results of the experiment are presented in Figure 3.6. From these results, it is clear that the F1 does not accurately measure temperatures outside of the 20 °C to 40 °C range. The uncertainty of the results from this sensor outweighs the convenience of only attaching a small sensor to a smartphone. It was therefore decided to not use the F1 for the remainder of the study.

The C3 has a constant error of about 2 K. It has a lower average error than the single-area IR sensors, but a higher variation in error, as mentioned in Table 3.2. The higher variation in error is to be expected as it has a lower specified accuracy than the low-cost sensors.

Table 3.2. Calibration results for all the sensors. SD is standard deviation and s is standard error of the fit

Sensor	Original MAE [K]	σ [K]	Slope	Intercept	s [K]	Calibrated MAE [K]
C3	1.87	1.04	0.97	-1.00	1.82	0.74
F1	2.45	2.91	1.22	-7.70	2.95	1.29
IR_Arr	1.33	1.48	0.99	-0.60	0.78	1.23
IR12	1.46	0.45	1.02	-1.93	1.51	0.29
IR35	1.30	0.74	0.96	-0.19	1.45	0.37
IR90	1.37	0.92	1.06	-2.86	1.45	0.34

Note: s is standard error of the fit and MAE is mean average error.

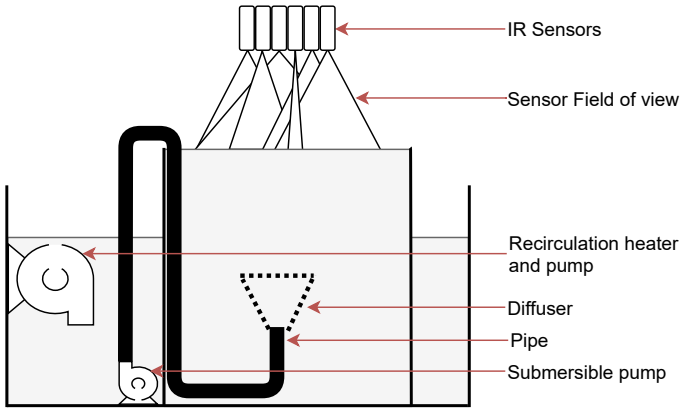

Figure 3.5. Schematic of sensor calibration experiment set-up

The three single-area IR sensors perform well with near linear offsets from the reference temperature. At temperatures above 40 °C, the IR90 sensor has large negative errors. According to the sensor data sheet, these errors were only expected to increase at a target temperature of around 60 °C (Melexis, 2019).

The IR_Arr sensor has large negative errors with high variation. It performs well in the 22 °C to 33 °C range. The mean average errors of the C3,F1 and IR_Arr are within the specified accuracy, while the single-area IR sensors are all outside of the specified accuracy.

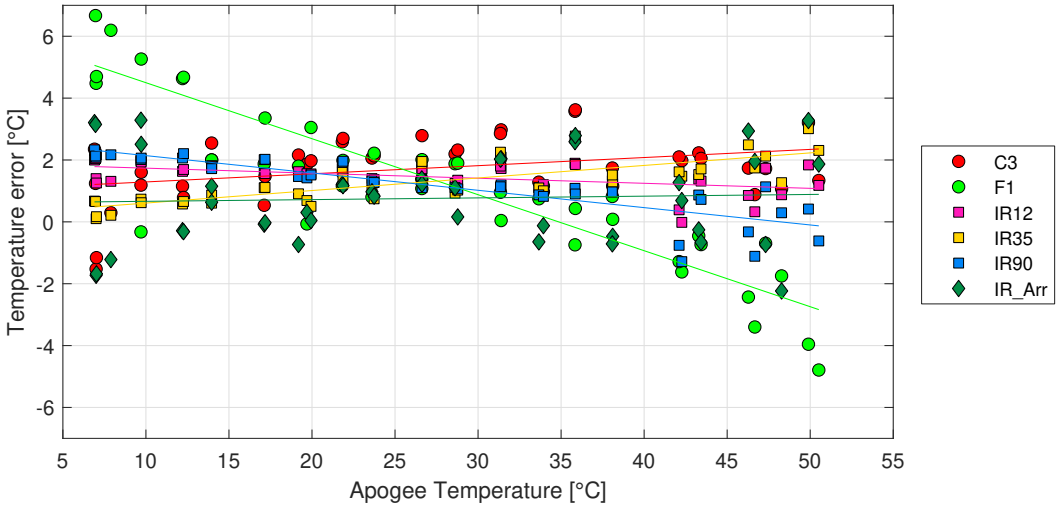

Figure 3.6. Measurement errors for all the sensors at different temperatures using the Apogee as a reference sensor. The errors were calculated by subtracting the reference temperature from the respective sensor temperatures.

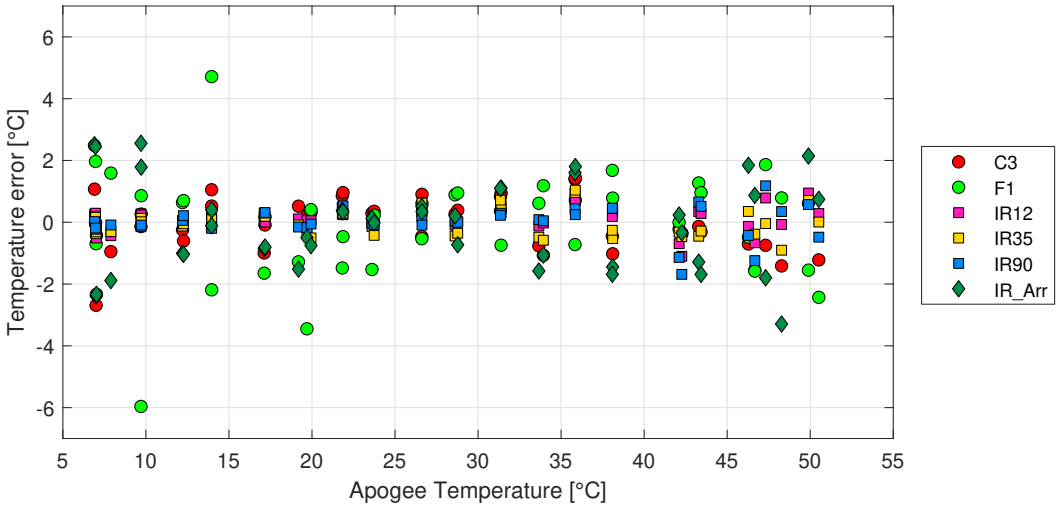

Figure 3.7. Measurement errors after applying the linear calibration.

The observed sensor errors are linear in the measured temperature range. Linear calibration curves were used to calibrate the sensors to the Apogee sensor. The standard error of the fit, s, relates to how closely a polynomial fits a data set (Figliola, 1995) and is calculated as

$$s = \sqrt{\frac{\sum_{i=1}^{N} (y_{\mathrm{f,i}} - y_{\mathrm{o,i}})^2}{N - (m+1)}} \tag{3.1}$$

where m denotes the order of the fit, which is 1 in this case. The standard error of the fit provides a measure of how much each data point is shifted with the calibration. Table 3.2 presents s, the standard error of the fir, and the slope and intercepts of the linear calibration. The C3 has the lowest fit error, while the F1 has the largest fit error of the investigated sensors.

The source of the errors in the single-area IR sensors is unknown, but it is compensated for. Due to the low variation in and the linear nature of the errors, the linear calibration is appropriate.

3.4 Conclusion

The different IR sensors, along with their various specifications and accuracies are presented in this chapter. The implantation of the low-cost sensors in the MR is explained. The calculation procedure for the Flir sensors is presented as a suitable alternative to the use of Flir Tools.

A water bath calibration procedure was used to ensure that the sensors report the same temperature. This allows for temperature comparisons between the different sensors. It was found that the Flir F1 is not suitable for this study and that the low-cost IR sensors have a nearly constant error when compared to a calibrated IR sensor.

Chapter 4

Reference temperatures modelling and measurement

4.1 Introduction

4.1.1 CWSI

The crop water stress index (CWSI) is the "best known" thermal stress index (Pou *et al.*, 2014). It was defined by Idso *et al.* (1981) and further refined by Jones (1999). The CWSI has been used extensively in precision viticulture research (e.g., Grant *et al.* (2006); Petrie *et al.* (2019); Sepúlveda-Reyes *et al.* (2016); Shellie and King (2020)).

$$CWSI = \frac{T_c - T_{wet}}{T_{dry} - T_{wet}} \tag{2.3}^*$$

The CWSI normalises the canopy temperature between the minimum possible temperature (T_{wet}) of a canopy transpiring at the maximum potential rate, and maximum possible temperature (T_{dry}) of a canopy not transpiring at all (Idso *et al.*, 1981). A plant under severe plant water stress will have a CWSI close to 1, while a fully transpiring plant will have a CWSI close to 0. Ideally, a fully transpiring and a non-transpiring plant, under the same environmental conditions as the canopy being measured, must be used for T_{wet} and T_{dry} measurements, respectively. This approach is impractical as it is nearly impossible to have two such reference plants under similar environmental conditions (Poirier-Pocovi *et al.*, 2020). Many researchers find that the practical implications of the reference temperatures are a limitation to the implementation of IR technology in vineyards (e.g. Grant *et al.* (2006); Petrie *et al.* (2019); Sepúlveda-Reyes *et al.* (2016); Poblete-Echeverria *et al.* (2017)).

4.1.2 Natural reference temperature method

Now-a-days, there are different methods to obtain T_{wet} and T_{dry}. Jones (1999) was the first to use Vaseline and soapy water-covered leaves for reference T_{dry}

and T_{wet} measurements, respectively. This method is referred to as the 'Natural method'. The Vaseline prevents the leaf from transpiring and thus being cooled, while the water covered leaf simulates a fully transpiring leaf that cools by evaporation. This method has become a common practice in research (Garcia-Tejero *et al.*, 2016; Petrie *et al.*, 2019; Poirier-Pocovi *et al.*, 2020). There are however some practical limitations with this method. For example, Jones (1999) suggests measuring T_{dry} and T_{wet} before and after measuring each canopy, but this is impractical when measuring many plants.

Sudden gusts of wind, a passing cloud or the selection of the leaf can have an influence on the reference temperatures, which the CWSI is very sensitive to. The application of Vaseline is destructive to the leaf and can influence the plant's physiology if the Vaseline is applied to many leaves throughout the season.

4.1.3 Alternative reference temperature methods

These problems with the Natural reference method have motivated researchers to look for alternative techniques in determining reference temperatures, such as: (i) Mathematical leaf energy balance (LEB) equations which do not need direct T_{wet} and T_{dry} measurements and which account for physiological parameters, net radiation, sensible heat transfer and evaporative cooling at steady state (Jones, 2014). This method has been used in literature (e.g. (Fuentes *et al.*, 2012)), but requires physiological parameters that are difficult to determine (Poirier-Pocovi *et al.*, 2020); (ii) Artificial reference surfaces, such as cloth fabric (Maes *et al.*, 2016) and coloured paper (Poirier-Pocovi *et al.*, 2020) have been investigated, but do not have any physical resemblance to leaf material; (iii) Empirical correlations, such as adding 5 K to 7 K to the ambient temperature for T_{dry} have been investigated (Moller *et al.*, 2007; Rud *et al.*, 2014), but are usually done after the season when the maximum temperature reached by the canopy can be observed. The plants' physiological response changes throughout the season and Fernandes de Oliveira *et al.* (2021) used wet- and dry-bulb temperatures for T_{wet} and T_{dry} respectively, but had to add coefficients to compensate for the different physiological stages; (iv) Modern methods such as machine learning have been used successfully but requires large datasets (multiple seasons) to train the models (Shellie and King, 2020). These modern methods, such as machine learning and optimisation, can be combined with engineering heat transfer approaches to simulate the natural reference method, which is known to be reliable. This proposed method can provide reference values which are based on the appropriate theory, the development of the method is aided by optimisation in estimating complicated parameters.

4.1.4 Chapter objectives

First, different protocols for the measurement of the natural method are compared, in order to establish a consistent and reliable method for the rest of the

study.

The second aim is to propose and test two new methods for determining reference temperatures. One is based on heat transfer principles, while the other is an empirical formulation based on wet- and dry-bulb temperatures. The proposed methods use only meteorological data from a local weather station and eliminates the need for in-field reference temperature measurements. A particle swarm optimisation (PSO) technique was used to obtain the parameters in the heat transfer (HT), LEB and empirical (EMP) methods. PSO was chosen as it is easy to implement, derivative-free and insensitive to initial points when compared to evolutionary methods (Lee and Park, 2006). This method, along with LEB and EMP methods, which are traditional methods of estimating the reference temperatures, are compared to the Natural method proposed by Jones (1999).

The final aim is to determine the applicability of low-cost sensors to measure reference temperatures by comparing them to a commercial infrared camera.

4.2 Materials and methods

4.2.1 Experimental site and plant material

The study was conducted during the season 2020-2021 at Thelema wine farm (-33°54'11.8"S - 18°55'12.4"E and 430 m above sea level) in Stellenbosch, South Africa. The vine cultivar is Cabernet Sauvignon vines, clone CS 338 C grafted on 101-14 rootstock which were planted in 2003 with a North-South orientation. The 2.42 ha block has a 2 m vine spacing and 2.5 m m row spacing and it is drip-irrigated with emitters spaced at 0.6 m (2.3 L/h). The vines are trained to a Vertical Shoot Positioning trellis system with bi-lateral cordon and spur pruned. The soil is sandy loam with a pH of 5.7 and the geology of the region is characterised by compacted sedimentary formations of the Malmesbury Group from the Precambrian Era (Carey, 2005; King and King, 1984). The historical average yield in the block is 8.24 Ton/ha with an average of 4.0 kg/vine. The climate in the area is Mediterranean with winter rainfall. Koppen-Geiger climate classification - Csb (Peel *et al.*, 2007). The seasonal ambient temperature (from September 2020 to March 2021) ranged between 5 °C and 44 °C. For the same period, the effective rainfall was approximately 184 mm.

4.2.2 Meteorological data

Ambient conditions (solar radiation, wind speed, temperature, relative humidity and rainfall) were measured hourly by a standard commercial weather station located within 300 m of the experimental site. These ambient conditions were used in the HT method, the EMP method and for importing the thermal image data. A net radiometer (Hukselflux, model NR01, Delft, Netherlands) was used to

measure net radiation at 15-minute intervals for the LEB model. Upon analysing the data it was noticed that the radiation measurements from the weather station were consistently lower than those of the net radiometer and weather station data from Stellenbosch. It was decided to use net radiometer data, which also measures solar radiation, for determining the net radiation.

4.2.3 Measurement procedure

Reference temperature measurements were done on seven days, at 12:00 and 14:00, in conjunction with canopy temperature measurements required for the next chapters. Jones (1999) suggests taking measurements before and after measuring canopy temperature. It is time-consuming and impractical to do this with all plants and there is the risk of encountering changing weather and solar position conditions if measurements take too long. Six reference temperature data points were collected for each measurement period, which lasted about 30 minutes. All measured leaves were orientated normal to and in the centre of the plant canopy.

For measurements with the C3, thermal images were recorded from ±0.3 m, without casting a shadow on the sunlit leaves. In the data processing process, the average temperature of a selected region of interest (ROI), discussed in section 3.2.1, is taken as the leaf temperature. The IR sensors in the measurement rig (MR) were held close (±20 mm) to the target leaf. For the IR-array sensor, the most frequent value from the temperature distribution was taken as the representative temperature.

To ensure that outliers do not influence the average of the reference values that are used, the following method is used to identify outliers: Compare the two temperatures measured before and after each treatment group. If the values differ by more than 3 K, omit the value that is the furthest away from the group average (not including the two points from the group).

4.2.4 Reference temperature measurement protocol

In literature both attached and detached leaves are used for reference temperatures and the methodology is not standardised. Some researches (e.g., Jones (2002); Fuentes *et al.* (2012)) use attached reference leaves while others (e.g.,Petrie *et al.* (2019); Stoll and Jones (2007)) use detached leaves. The benefit of using a detached leaf is that it is not affected by plant conditions and a single leaf can be reused for multiple measurements, causing less damage to the vines. The drawback is that it is not completely representative of the maximum temperature that a canopy can reach, as it is not under the same physical conditions as the plants. Comparing sunlit to shaded side of the canopy, most authors use reference surfaces from the same side of the canopy temperature measurement. From trials in the previous season, it was observed that a sunlit wet leaf can reach a temperature similar to that of the sunlit canopy. Jones (2002) indicates that the difference

Table 4.1. Alternative reference temperature methods considered

Method	Code	Comment	Source
Natural Method	N	Baseline method where T_{wet} is a water sprayed leaf and T_{dry} is a Vaseline covered leaf	(Jones, 1999)
Leaf energy balance	LEB	Optimise the stomatal resistance, see Section 4.2.6	(Jones, 2014)
Heat transfer	HT	Optimise multiple parameters, see Section 4.2.7	Proposed method
Empirical method	EMP	Optimise empirical values, see Section 4.2.8	Proposed method

in exposure to solar radiation between the reference leaves and the canopy can lead to errors.

The following reference temperatures were measured: (i) Wet sunlit leaf; (ii) Wet shaded leaf; (iii) Dry attached shaded leaf; (iv) Dry detached shaded leaf; (v) Dry attached sunlit leaf; (vi) Dry detached sunlit leaf. The detached leaves were attached to the post supporting the vines with tape, in a similar orientation to the attached leaves being measured.

4.2.5 Baseline method

In this study, the natural reference method (N) proposed by Jones (1999), described in Section 4.1.2, is used as a baseline for comparison and parametrisation of the three alternatives methods. The average of all six measurements was taken as the baseline temperature for that day. The exact condition of these reference leaves, discussed in Section 4.2.4 is established as the first objective of this chapter.

The alternative methods of determining T_{dry} and T_{wet} that are investigated are summarised in Table 4.1.

4.2.6 Leaf energy balance method

The LEB method is described in section 2.4. The final equations are repeated for sake of convenience:

$$T_{dry} = T_a + \frac{r_{HR} R_N}{\rho c_p} \tag{2.7}^*$$

$$T_{wet} = T_a + \frac{r_{HR} r_{b,V} \gamma R_N}{\rho c_p (\gamma r_{b,V} + s r_{HR})} - \frac{r_{HR} \delta_e}{\gamma r_{b,V} + s r_{HR}} \tag{2.8}^*$$

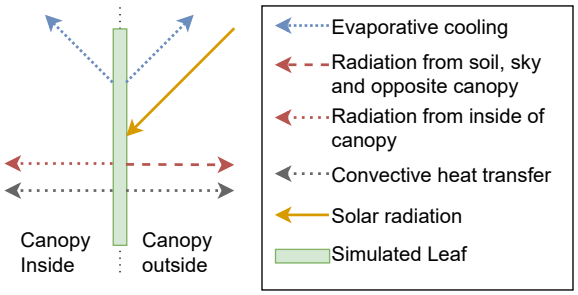

Figure 4.1. Schematic of heat transfer components

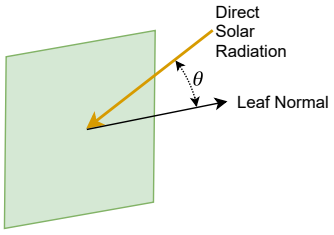

Figure 4.2. Solar angle of incidence (θ) on leaf

4.2.7 Heat transfer calculations

Assumptions and simplifications

The heat transfer (HT) approach uses basic heat transfer principals and climatic properties of the microclimate to estimate the reference surface temperatures. The two reference surfaces, T_{wet} and T_{dry}, are modelled as 0.1 m × 0.1 m vertical flat plates normal to and in the centre of the grapevine canopy, with North-South oriented rows. T_{dry} is simulated as a Vaseline-covered leaf; fully stressed with closed stomata allowing no transpiration. In contrast, T_{wet} is simulated by assuming that the leaf is covered by a thin layer of water. This T_{wet} method is an over estimation of maximum transpiration rate, as a leaf will never get fully wet by itself but it is independent of plant condition and stomatal resistance, which are difficult to measure.

The mechanisms of heat transfer considered are radiative, convective, and evaporative (only in the case of T_{wet}), as shown in Figure 4.1. Conduction to plant tissue is insignificant and can be ignored (Watson, 1933). The leaf is thin, and it is assumed that it has a uniform temperature.

The back of the leaf is exposed to the shaded inside of the canopy, while the front is exposed to the shaded side of the adjacent row canopy, the soil and the sky, with direct sunlight for the T_{dry} leaf. The soil is a combination of red clay and dead grass and a small portion of the soil is shaded by the adjacent row canopy. The soil temperature can exceed 50 °C but has a relatively low influence on the leaf temperature in terms of radiative heat transfer. The soil is therefore simulated as a single surface with the radiative properties of soil being 27 °C above observed ambient temperature (calculated based on the average ground truth measurements observed over all the days). The canopy of the adjacent row is modelled as a single shaded surface with the radiative properties of a big grapevine leaf. It is assumed that the wind direction is North-South down the rows.

Radiative heat transfer

Heat is transferred between any two surfaces at dissimilar temperatures via thermal radiation. Any surface above 0 K emits thermal radiation and the amount is

proportional to the object's surface temperature. Relevant radiation heat transfer theory is presented in Appendix A.

Radiation heat transfer depends on the orientation of both surfaces. The view factor, F_{ij} is defined as the fraction of radiation emitted from surface i that strikes surface j directly. The sum of all the view factors for surface i to N surfaces is equal to 1, to account for all the radiation emitted by object i. The heat transfer from surface i is then

$$\dot{Q}_i = A_i \sum_{j=1}^{N} F_{ij}(J_i - J_j) \tag{4.1}$$

with $\dot{Q}_i$ the rate of heat transfer, A the area of surface i and J the radiosity (Cengal and Ghajar, 2015, eq 13-34):

$$J_i = \epsilon_i \sigma T_i^4 + \rho_i G_i \tag{4.2}$$

where T is the temperature in Kelvin, G is the incident radiation on the surface and ϵ is the emissivity of the surface. The reflectivity of grapevine leaves is low (about 0.04), resulting in a very small fraction of the reflection off surface. Equation 4.2 is simplified to

$$J_i = \epsilon \sigma T_i^4 \tag{4.3}$$

The radiation heat transfer between the soil and target leaf is thus

$$\dot{Q}_{s-l} = A_s F_{s-l} \sigma (\epsilon_s T_s^4 - \epsilon_l T_l^4) \tag{4.4}$$

and similar relations are derived for $\dot{Q}_{bc-l}$,$\dot{Q}_{sky-l}$ and $\dot{Q}_{oc-l}$.

The radiative emissions from the sky, mainly due to CO_2 and H_2O can be approximated by the temperature near the surface of the earth (Mills and Gansen, 2009). Brunt (1940) found an empirical correlation for the emissivity of the sky based on the ambient temperature T_a and relative humidity, ϕ, for a clear sky.

$$\epsilon_{sky} = 0.55 + 1.8\sqrt{P_{H_2O}/P_a} \tag{4.5}$$

where P_a is the atmospheric pressure and P_{H_2O} is the water vapour pressure. The water vapour pressure can be calculated as

$$P_{H_2O} = \phi \cdot P^*_{H_2O} \tag{4.6}$$

The radiation from the sky can be estimated assuming the sky is at ambient temperature with an emissivity of ϵ_{sky} (Mills and Gansen, 2009, example 6.9).

The view factors between the leaf and other surfaces were calculated with the Nullselt unit sphere method. The radiating surfaces for 10 m in each direction were taken into account for heat transfer relations.

The solar energy transferred to the surface of the leaves consists of diffuse solar radiation (G_d) and direct solar radiation, G_D (for the T_{dry} leaf). Diffuse solar

radiation is scattered by the earth's atmosphere and reaches the surface from all directions. For a vertical surface at an angle:

$$G_{\mathrm{d}} = 0.5 \cdot G_{\mathrm{d}} \cdot (1 + \cos\beta) \tag{4.7}$$

where β is the angle between the horizontal and the surface (Maxwell *et al.*, 1986), assuming diffuse radiation is isotropically scattered in a hemisphere. The total incident solar radiation on a surface is the combination of the direct and diffuse components.

$$G_{\mathrm{solar}} = G_D \cos\theta + G_{\mathrm{d}} \tag{4.8}$$

where θ is the angle between the surface normal and the sun, shown in Figure 4.2. This angle is calculated with NREL's Solar Position Algorithm (Reda and Andreas, 2008), with a Matlab function developed by Mahooti (2021). The direct component of solar radiation is omitted for T_{wet} as the leaf is in the shade. The solar energy absorbed by a leaf is

$$\dot{Q}_{\mathrm{solar}} = \alpha_{\mathrm{l}} G_{\mathrm{sol}} \tag{4.9}$$

where α_{l} is the solar absorptivity of the leaf. Nobel (2009) indicates that α is between 0.4 and 0.6 for plant leaf material, but Vaseline- and water-covered leaf material, with undocumented properties, are simulated.

The total radiative heat transfer is the sum of the solar, sky, soil and opposite canopy radiative heat transfer

$$\dot{Q}_{\mathrm{rad}} = \dot{Q}_{\mathrm{sol}} + \dot{Q}_{\mathrm{oc-l}} + \dot{Q}_{\mathrm{s-l}} + \dot{Q}_{\mathrm{sky-l}} + \dot{Q}_{\mathrm{bc-l}} \tag{4.10}$$

Convective heat transfer

Convective heat transfer occurs between the leaf surface and the air. The Reynolds number is calculated to estimate the flow regime of the moving air.

$$Re = \frac{V L_c}{\upsilon} \tag{4.11}$$

υ is the kinematic viscosity of the air while L_{c} is the characteristic length of the leaf, taken as the area divided by the circumference, $L_{\mathrm{c}} = 0.1$ for the flat plate assumption. For typical ambient conditions of wind (V) at 1 m/s and $T_{\mathrm{a}} = 25\,^{\circ}\mathrm{C}$, Re is calculated and found to be around 7 000 , which is in the laminar flow regime. Only when wind speed reaches about 6 m/s, does the flow become turbulent.

According to Cengal and Ghajar (2015), the convective heat transfer coefficient can be calculated as

$$h = 0.664 \frac{k}{L_{\mathrm{c}}} Pr^{1/3} Re^{1/2} \tag{4.12}$$

where k is the thermal conductivity and Pr is the Prandtl number of air at the given temperature. Finally, the energy lost due to convective cooling is calculated as

$$\dot{Q}_{\text{conv}} = 2hA_{\text{l}}(T_{\text{l}} - T_{\text{a}}) \tag{4.13}$$

The multiplication by 2 is on account of convective heat transfer that occurs on both sides of the leaf.

Evaporative heat transfer

As water is evaporated off a surface, it is converted to a gas and removes energy from the surface in proportion to the mass flow rate and the enthalpy of evaporation, h_{fg}.

The diffusion of water vapour into the air has received significant attention for the development of empirical equations (Cengal and Ghajar, 2015, p 841). Marrero and Mason (1972) proposed the following formula:

$$D_{\text{H}_2\text{O}-\text{air}} = 1.87 \cdot 10^{-10} \frac{T^{2.072}}{P} \tag{4.14}$$

Sc, the dimensionless Schmidt number is then calculated for the relative magnitude of momentum diffusivity to mass diffusivity.

$$Sc = \frac{\upsilon}{D_{\text{H}_2\text{O}-\text{air}}} \tag{4.15}$$

Similar to the Nusselt number calculated for convective heat transfer, the Sherwood number is calculated for convective mass transfer. The Sherwood relation (Sh) for laminar forced convection over a flat plate is

$$Sh = 0.664 Re^{1/2} Sc^{1/3} \tag{4.16}$$

The mass transfer coefficient is then calculated

$$h_{\text{mass}} = \frac{Sh \cdot D_{\text{H}_2\text{O}-\text{air}}}{L_{\text{c}}} \tag{4.17}$$

before the mass flow rate of the water vapour is calculated as

$$\dot{m}_{\text{H}_2\text{O}} = h_{\text{mass}} A_{\text{l}} (\rho_{\text{v,s}} - \rho_{\text{v},\infty}) \tag{4.18}$$

with $\rho_{\text{v,s}}$ and $\rho_{\text{v},\infty}$ the density of the water vapour at, and far from the surface respectively. Finally, the heat energy lost due to the evaporation is calculated as

$$\dot{Q}_{\text{evap}} = \dot{m}_{\text{H}_2\text{O}} h_{\text{fg}} \tag{4.19}$$

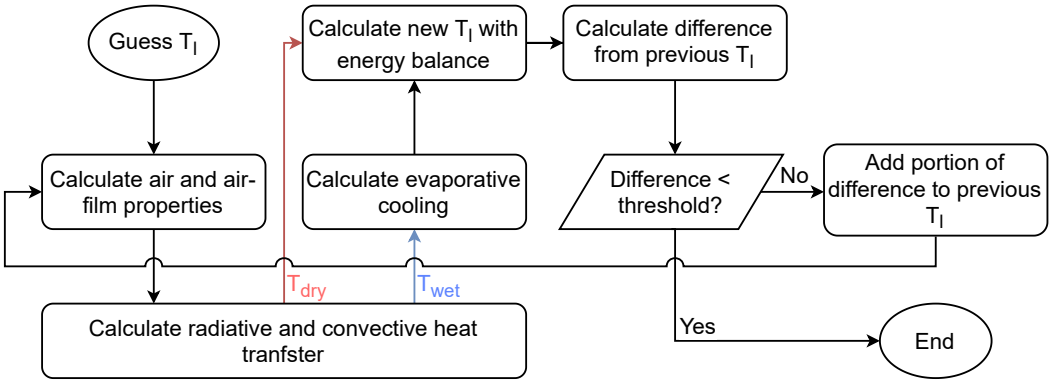

Figure 4.3. Flow diagram presenting the iterative method of calculating the leaf surface temperature. Note the different paths for T_{wet} and T_{dry}

Energy balance and iterative solution

The steady state of the leaf must calculated iteratively. According to convention, energy transferred to the leaf is taken as positive.

$$\dot{Q}_{\text{in}} - \dot{Q}_{\text{out}} = 0 \tag{4.20}$$

$$\dot{Q}_{\text{rad}} + \dot{Q}_{\text{evap}} + \dot{Q}_{\text{conv}} = 0 \tag{4.21}$$

Rearranging the terms and solving for T_l in equation 4.13

$$T_l = \frac{\dot{Q}_{\text{rad}} + \dot{Q}_{\text{evap}}}{2hA_l} + T_a \tag{4.22}$$

For each of the radiation terms, as well as the evaporation term, the leaf surface temperature as well as air properties are required. T_l is solved iteratively by estimating a leaf's temperature before recalculating it, while updating the air properties at each step. Air properties are calculated by interpolation between values found in the Air Properties table of (Cengal and Ghajar, 2015, p. 924)

T_l tends to diverge and a damping term is introduced to limit the effect of the newly calculated T_l:

$$T_l = T_{l,\text{prev}} + d(T_{l,\text{new}} - T_{l,\text{prev}}) \tag{4.23}$$

For a d value of 0.1, T_l was observed to converge. The solution strategy is presented in figure 4.3.

For the dry reference leaf, $\dot{Q}_{\text{evap}}$ is simply omitted. For the wet reference leaf, the direct component of solar radiation is omitted to simulate the leaf in a shaded part of the canopy. This is done to ensure that T_{wet} represents the absolute minimum temperature that a leaf in the canopy can reach.

4.2.8 Empirical Method

Moller *et al.* (2007) found that calculating T_{dry} as a constant offset of 5 K from the ambient temperature provided a simple method for estimating the maximum

canopy temperature. The canopy temperature in our experiment often exceeded the ambient temperature by as much as 7 K. The best value for this parameter, δ_{offset} is unknown.

$$T_{\text{dry,EMP}} = T_{\text{a}} + \delta_{\text{offset}} \tag{4.24}$$

Furthermore, from this study's experimental data, it was observed that the Natural method's T_{wet} corresponds well to a temperature between the wet-bulb and dry-bulb temperature.

$$T_{\text{wet,EMP}} = T_{\text{wb}} + \delta_{\text{frac}}(T_{\text{db}} - T_{\text{wet-bulb}}) \tag{4.25}$$

Wet-bulb temperatures are calculated from the ambient (dry-bulb) temperature and relative humidity, according to an empirical formulation by Stull (2011):

$$\begin{aligned} T'_{\text{wb}} = T_{\text{a}} \operatorname{atan}(0.151977\sqrt{\phi + 8.313659}) \\ + \operatorname{atan}(T'_{\text{a}} + \phi) - \operatorname{atan}(\phi - 1.676331) \\ + 0.00391838(\phi)^{3/2} \operatorname{atan}(0.023101\phi) \\ - 4.686035 \end{aligned} \tag{4.26}$$

The values δ_{offset} and δ_{frac} are optimised to provide the best empirical correlation that minimises the difference between $T_{\text{wet,N}}$ and $T_{\text{wet,EMP}}$ and $T_{\text{dry,N}}$ and $T_{\text{dry,EMP}}$, respectively.

4.2.9 Optimisation

Some parameters of the HT, LEB and EMP models are difficult to measure or not documented. These parameters are listed in Table 4.2, along with a description and bounds. Parameters were optimised by minimising the difference between calculated and measured T_{dry} and T_{wet} values over the seven test days (morning and afternoon). The average error of T_{wet} and T_{dry} were optimised as a single HT model calculates both T_{wet} and T_{dry}. Even though the vines go through different phenological stages, the set of parameters that is optimised is constant throughout the season. This is because the HT model is optimised to the values of the Natural reference, which is not plant-dependent.

The data is split into training and testing at roughly 70% to 30% to verify the results of the optimisation. The models are trained on all the data except for 26 January and 23 February that were selected as the last measurement days of the two major physiological periods. Leaving these two days out ensures that the data is not over fitted.

PSO was used as it is easy to implement, derivative free and insensitive to initial points when compared to evolutionary methods Lee and Park (2006). When compared to other stochastic methods, it can provide quality results with stable convergence characteristics Gaing (2003). The built in Matlab PSO was used. Five reruns were done with 50 particles and 50 iterations.

Table 4.2. Optimisation parameters and bounds

Parameter	Model	Description	Lower bound	Upper bound
α_v	HT	Vaseline-covered leaf solar absorptivity	0.25	1
α_w	HT	Water-covered leaf solar absorptivity	0.25	1
f_{dir}	HT	Fraction of solar radiation that strikes the T_{dry} leaf directly. This value is difficult to measure (Cengal and Ghajar, 2015)	0.8	0.95
δ_{bc}	HT	The surface of the internal canopy radiates heat to the back of the reference leaves. It is optimised to a difference from T_a.	−10 K	10 K
θ_e	HT	The error from the calculated solar angle of incidence presented in Figure 4.2. Leaves facing normal to the canopy were selected for applying Vaseline, but leaves are not simple flat surfaces as approximated and the angles were not determined accurately.	−10°	10°
δ_{offset}	EMP	The difference between T_a and T_{dry}	−10 K	10 K
δ_{frac}	EMP	The fraction between the wet-and dry-bulb temperatures for T_{wet}	0	1

HT and EMP are the heat transfer and empirical models respectively

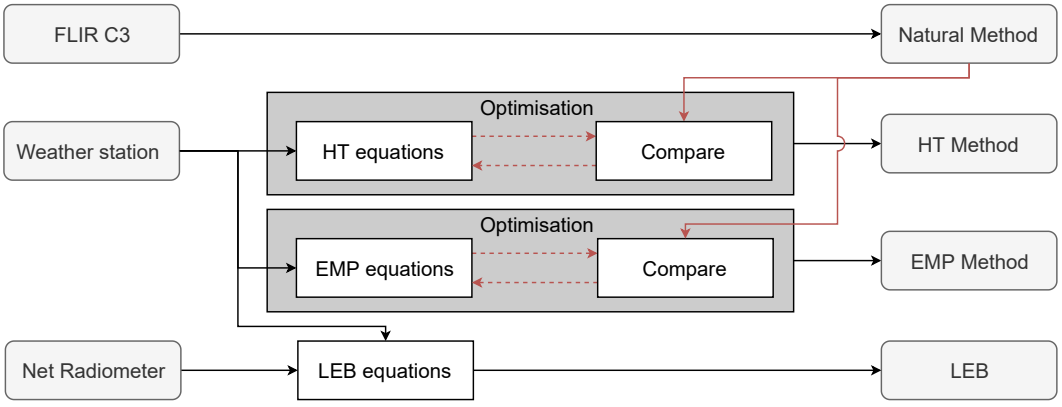

Figure 4.4. Data flow pipeline for computing the various models and optimisations.

A fitness function calculates T_{dry} and T_{wet} for each of the models, based on the meteorological conditions and optimisation parameters. The fitness value is calculated as

$$f = e^{|T_{\text{wet,N}} - T_{\text{wet,M}}|} + e^{T_{\text{dry,N}} - T_{\text{dry,M}}} - 2\,, \tag{4.27}$$

where M denotes the model under consideration. A value of two is subtracted for perfect fitness value to be equal to zero (only for convention). The use of the exponential errors produce better results when compared with normal error values (results not shown). The average of the T_{wet} and T_{dry} errors across all the training days is taken as the final fitness value. The flow of data to determine the different reference methods is presented in Figure 4.4.

The PSO is used for the HT model, where the solution space is complex with five variables. The built-in Matlab function fminc produced worse results compared to PSO (results not shown). A complicated random technique such as PSO is not necessary to optimise simple 2-dimensional problems like the EMP model, but was used for consistency. Other minimising functions would be able to find the optimal values for the EMP model.

4.2.10 Data analysis

A principle component analysis (PCA) of the meteorological data and measured reference temperatures is used to investigate the correlation between the different variables. PCA is a method of interpreting data by reducing data dimensionality while at the same time reducing information loss (Jolliffe and Cadima, 2016). Variables with the same direction on the PCA diagram are positively correlated, while uncorrelated variables are orthogonal. Individual points are plotted on the PCA diagram to visualise their influence over the variables.

The root mean squared error (RMSE), which weighs large errors highly, is used along with the mean absolute error (MAE) to compare the models. If the variance between individual samples is large, the difference between the RMSE and MAE will be large. The mean bias error (MBE) indicates whether a value is over- or underestimated. A 95% confidence interval (CI), calculated with a t-score due to the low sample numbers, is used to determine the true mean of the population.

$$RMSE = \sqrt{\frac{1}{N}\sum_{i=1}^{N}(x_{f,i} - x_{o,i})^2} \tag{4.28a}$$

$$MAE = \frac{1}{N}\sum_{i=1}^{N}|x_{f,i} - x_{o,i}| \tag{4.28b}$$

$$MBE = \frac{1}{N}\sum_{i=1}^{N}(x_{f,i} - x_{o,i}) \tag{4.28c}$$

$$CI = MBE \pm t\frac{\sigma}{\sqrt{N}} \tag{4.28d}$$

where N is the sample size, σ is the standard deviation.

4.3 Results

4.3.1 Environmental conditions

A summary of the recorded meteorological data is presented in Table 4.3. Solar and net radiation values are consistently high as only clear cloudless days were selected for measurements. Humidity, which is temperature-dependent, is relatively consistent. Wind speed has little variation, except for the first day where it has double the average value. The ambient temperature varies by about 10 K.

Table 4.3. Summary of recorded meteorological data with the given measurement ID that will be used throughout the document

ID	Date (2021)	Time	T'_a [°C]	ϕ [%]	V [m/s]	R_{solar} [W/m^2]	R_{net} [W/m^2]	VPD [kPa]
1a	01/13	12:00	30.3	51.2	2.5	988.1	654.4	2.09
1b	01/13	14:00	31.6	48.8	2.3	900.8	574.1	2.36
2a	01/14	12:00	32.1	40.3	1.9	969.7	628.8	2.83
2b	01/14	14:00	34.2	41.5	2.6	943.2	612.1	3.11
3a	01/22	12:00	30.7	45.9	0.9	960.9	628.2	2.37
3b	01/22	14:00	30.6	47.1	1.7	969.7	624.5	2.30
4a	01/26	12:00	25.4	58.5	1.9	988.1	652.1	1.33
4b	01/26	14:00	25.4	61.3	2.7	975.4	637.2	1.25
5a	02/02	12:00	29.2	40.0	1.1	951.4	628.2	2.41
5b	02/02	14:00	31.2	35.0	1.5	945.1	606.1	2.93
6a	02/09	12:00	27.8	55.5	1.2	936.2	610.2	1.65
6b	02/09	14:00	28.2	55.3	2.0	940.0	606.1	1.70
7a	02/23	12:00	21.3	61.4	1.4	890.6	586.0	0.97
7b	02/23	14:00	22.9	55.7	1.8	884.9	571.8	1.23

Note: The ID is used to identify the dates throughout the rest of the document. The ID is created by chronologically assigning number to the measurement days and adding an 'a' or 'b' for 12:00 and 14:00 measurements respectively. VPD is vapour pressure deficit

A PCA of the meteorological data and measured reference temperatures is presented in Figure 4.5. From the Figure, it is clear that radiation explains most of the variability in the data. The solar and net radiation have a strong positive correlation. Even though the radiation is responsible for most of the variation in the data, it has low correlations to the other measured values. The wind has no correlation to the other variables and this is due to the low variation of wind conditions measured. In theory, if the absolute humidity remains constant and the ambient temperature increases, the relative humidity will decrease. This is

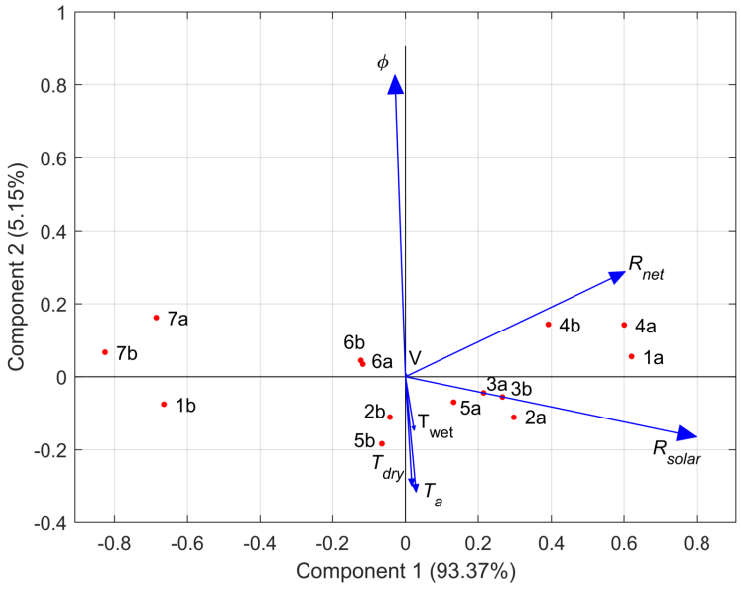

Figure 4.5. Principle component analysis on the meteorological conditions and the measured reference temperatures

seen in the PCA, where the negative correlation between T_a and ϕ is strong. Two points from the same day are generally close together, because of similar weather, specifically radiation, which has the strongest effect on the variation conditions, but not for 1a and 1b.. On this day, there was a sharp decrease in both solar and net radiation from 12:00 to 14:00. This was verified with the commercial weather station data that is not used.

4.3.2 Reference leaves condition selection

In Figure 4.6, the distributions of the different reference temperatures conditions are presented for certain days, along with the distribution of the shaded and sunlit canopy temperatures. It was decided to take reference measurements before and after each of three treatment groups discussed in Chapter 6.

With T_{wet}, the sunlit reference leaves reach temperatures similar to the sunlit and shaded canopies. The sunlit leaves have a larger variation than the shaded leaves. By using the shaded wet leaf, it is ensured that the wet reference is lower than the canopy temperatures, and a consistent temperature can be measured.

For T_{dry}, it is clear that the dry reference temperatures taken on the shaded side of the canopy overlap the shaded and sunlit canopy temperatures and are not fit for use. The dry sunlit leaves are well above the canopy temperatures, but there is significant variation in the detached leaf temperatures. These detached leaves reach very high temperatures as no convective cooling can take place on at the back of these leaves. For these reasons, it is decided that a attached, sunlit dry leaf must be used for a reference T_{dry} measurement. Is has a temperature consistently above the canopy and has low variability. An outlier on day 5a is

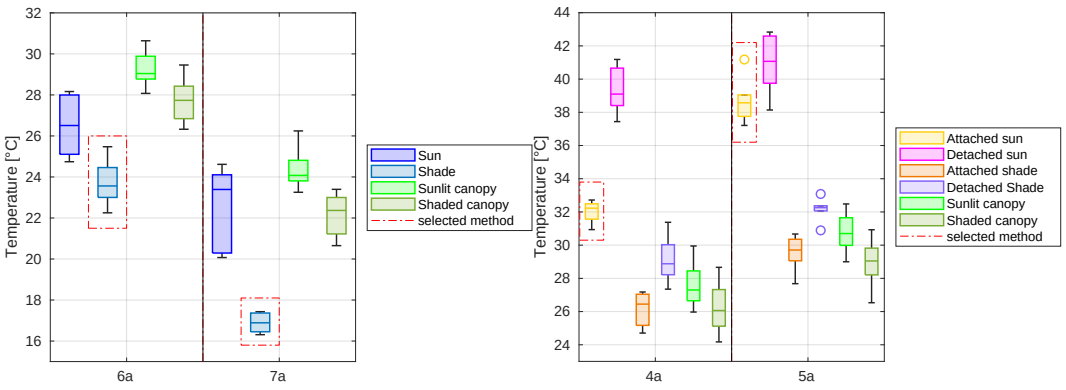

(a) T_{wet} and canopy **(b)** T_{dry} and canopy

Figure 4.6. Box plots of Natural reference surfaces under different conditions

noticed, but this data point is not considered for the average, as discussed in Section 4.2.3.

By fixing these reference methods as the baseline Natural method, it is ensured that the CWSI will be in the range of 0 to 1.

4.3.3 Optimisation

The results of the optimisation are presented in Table 4.4 and the errors are given in Table 4.5. The T_{wet} and T_{dry} errors are presented for each model and each period (training and testing).

The HT model performed well in calculating T_{wet}. The CI is within 0.5 K of the physical measurements. Only on two occasions did the error exceed 1 K. On the training day with the largest error (7a), all the models performed poorly, all underestimating T_{wet}. The HT method had the smallest T_{wet} error on this day. For T_{dry}, the largest HT error on day 5a, is once again overestimated by all the models. The HT method performed better on the testing data than on the training data for T_{dry}, which indicate that the model is not over-fitted. The 95% confidence interval for the T_{dry} with the HT methods is (-0.11 ± 0.87) K.

The EMP model performed relatively well considering the simplicity of the method. The T_{wet} calculation of the EMP model a has larger variation than the HT model, as seen by the difference between the MAE and the RMSE. The T_{wet} errors of the EMP model are comparable to those of the HT model, at (-0.22 ± 0.54) K, but the T_{dry} errors are slightly higher at (-0.18 ± 1.13) K.

The unoptimised LEB model consistently underestimated T_{wet} and overestimated T_{dry}. There is no difference in the testing and training data, as the same model is used. The T_{dry} errors might be due to the temperature of a Vaseline-covered leaf being used as reference, whereas the equations were derived for a normal non-transpiring leaf. Likewise, the T_{wet} is calculated for a fully transpiring leaf, not a fully wet leaf and it was therefore expected that T_{wet} would be overestimated by the model. The use of Vaseline and water for T_{dry} and T_{wet} al-

Table 4.4. Model parameters reached with optimisation

Parameter	Model	Final Value	Comment
θ_e	HT	$-10°$	This value is on the lower bound and significantly increases the temperature of T_{dry}.
α_{v}	HT	0.63	This value slightly lowers T_{dry} and is close to the range of 0.4-0.6 that Nobel (2009) predicts for leaf material
α_{w}	HT	0.25	T_{wet} increases only slightly by this value
f_{dir}	HT	0.8	Values of around 0.9 reported for clear days Cengal and Ghajar (2015) but the final value is on the lower bound, increasing both T_{wet} and T_{dry}
δ_{bc}	HT	-5 K	A negative value is expected as the shaded inside of the canopy will be below T_{a}. This value will increase T_{wet} but decrease T_{dry}.
δ_{offset}	EMP	5.495 K	Very similar to the 5 K offset used by Moller *et al.* (2007) for Merlot in Israel. King and Shellie (2016) found that CWSI values were not in the desired range when using 5 K, indicating that a higher value is required. This value may be region and climate dependent.
δ_{frac}	EMP	0.219	A value below ambient temperature and above the wet-bulb temperature is guaranteed with this method, but is not comparable with other values in literature as it is a novel method. It provides consistently good results.

HT and EMP are the heat transfer and empirical models respectively

ready over- and underestimate these reference leaf temperatures. The T_{wet} and T_{dry} confidence intervals at (-3.84 ± 0.80) K and (3.57 ± 0.71) K respectively, indicate that the errors do not have large variations, but are nevertheless significantly under- and overestimated.

Some days produce large errors in all the models. Day 1a for example, has high T_{dry} errors. A change in the PCA for this day was discussed in Section 4.3.1. The models overestimated T_{dry}, indicating that the actual leaf did not receive as much radiation as measured by the weather stations. The radiation measurement may be incorrect for this period. On this day, the wind was the strongest of all the measurement periods, which explains the high error in the EMP model, which does not directly account for wind. The wind cooled down the T_{dry}, but the EMP model could not compensate for it. On day 5a, the calculated T_{dry} is very high, but investigating the weather conditions does not reveal a clear explanation of the large errors. The errors on this day do not conform to the errors on the other days. On day 3a, the lowest wind speed was recorded and the HT

and EMP models underestimated T_{wet} and T_{dry}. This may indicate that at low wind speeds, the wind is not transferred to the canopy rows. On day 7a, T_{wet} was underestimated by all the models. The LEB model had a particularly high T_{wet} error on this day, which had the highest relative humidity and the lowest VPD. As a result, the evaporative demand on the T_{wet} leaf was low. The models estimated that more cooling would occur as a result of evaporation, but the atmospheric conditions did not allow for this evaporation. The HT method, which directly calculates evaporation, had the lowest T_{wet} error on that day.

Overall, the HT method performed the best in calculating the reference temperatures. The simple EMP method performed better than the more complicated LEB method. The EMP model errors are within 0.5 K of the HT model. Optimisation on more days with more variation in weather conditions may further improve the results.

Table 4.5. Errors in calculating reference temperatures with the different automatic methods in the different measurement periods

Phase	ID	HT		EMP		LEB	
		T_{wet}	T_{dry}	T_{wet}	T_{dry}	T_{wet}	T_{dry}
Training Data	1a	0.81	2.08	0.79	2.69	-2.98	5.53
	1b	0.41	-0.17	0.30	0.32	-1.89	3.76
	2a	0.37	-0.69	-0.12	-1.64	-2.94	4.81
	2b	-0.89	-1.06	-1.43	-2.08	-3.36	3.75
	3a	-0.27	-2.77	-0.69	-3.61	-4.67	1.55
	3b	1.12	0.89	1.09	1.35	-2.39	3.49
	5a	0.70	2.98	0.95	3.50	-1.54	5.69
	5b	0.78	-0.21	0.60	-0.66	-2.53	3.21
	6a	-0.59	-0.62	-0.90	-1.00	-2.17	2.98
	6b	0.15	0.48	-0.05	0.54	-4.15	3.58
Testing Data	4a	-0.25	-0.06	-0.60	0.05	-4.81	4.09
	4b	0.67	-2.15	0.09	-2.35	-3.95	1.76
	7a	-1.56	0.66	-1.79	1.04	-6.39	3.58
	7b	-0.84	-0.85	-1.36	-0.72	-5.00	2.24
Testing Data	MAE	0.83	0.93	0.96	1.04	-	-
	RMSE	0.95	1.20	1.16	1.33	-	-
	MBE	-0.49	-0.60	-0.91	-0.49	-	-
All data	MAE	0.67	1.12	0.77	1.54	3.48	3.57
	RMSE	0.76	1.46	0.92	1.90	3.73	3.77
	CI	0.04 ±0.46	-0.11 ±0.87	-0.22 ±0.54	-0.18 ±1.13	-3.48 ±0.80	3.57 ±0.71

Note: T_{wet} and T_{dry} errors are in K. Negative errors are coloured and scaled blue and positive errors are coloured and scaled red.

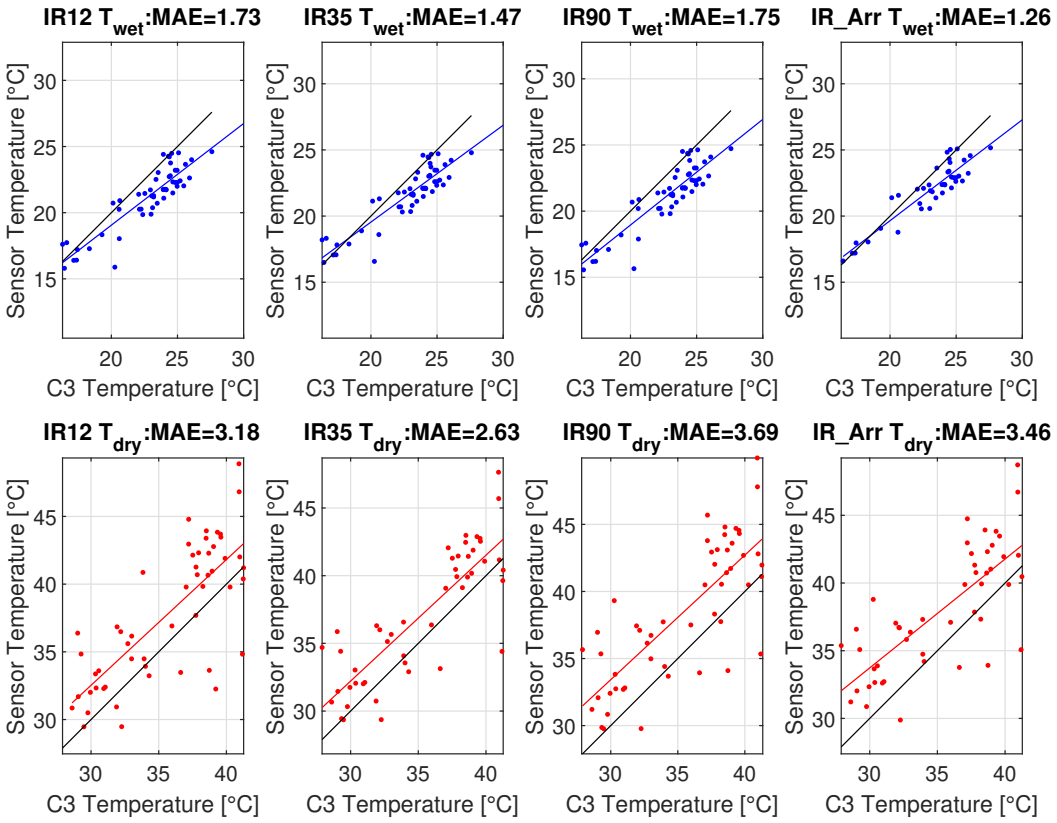

Figure 4.7. Low-cost sensor reference temperature vs C3 reference temperature. The black lines indicate a 1:1 relationship.

4.3.4 Low-cost sensor reference temperature measurements

In Figure 4.7, the difference between the C3 and the low-cost sensors is presented for T_{wet} and T_{dry} for individual measurements. The average T_{wet} errors are lower than the average T_{dry} errors, but T_{wet} has a different gradient from the C3. All sensors underestimated T_{wet} by about 2.5 K.

For T_{dry}, the low-cost IR sensors all measured higher temperatures than the C3. This could indicate that the Flir has a systematic error, but this is unlikely as the same offset is not observed for T_{wet}. The variation in the T_{dry} errors are much higher those that of T_{wet}.

The errors in Figure 4.7 may be misleading as the reference temperatures are taken as the average of six measurements. MAEs and MBEs are presented in Table 4.6. When combining the six measurements, the MAE of the combined measurements are lower, but the offsets seen in Figure 4.7 remains. The IR35 is the best performing sensor, with MAE below 1.5 K for both T_{wet} and T_{dry}.

Table 4.6. Low-cost sensors average errors of the six measurements

	MAE		MBE	
Sensor	T_{wet}	T_{dry}	T_{wet}	T_{dry}
IR12	1.75	1.89	1.75	-1.76
IR35	1.35	1.43	1.35	-1.29
IR90	1.77	2.77	1.77	-2.77
IR_Arr	1.14	2.29	0.90	-2.00

Note: T_{wet} and T_{dry} errors are in K

4.4 Discussion

4.4.1 Heat Transfer model sensitivity to weather conditions

The HT model's sensitivity to weather conditions is presented in Figure 4.8a. As expected, both T_{wet} and T_{dry} are sensitive to T_a. T_{wet} has evaporative cooling which increases with an increased ambient temperature. As the ambient temperature increases, the relative humidity decreases (assuming a constant absolute humidity) and the rate of evaporation increases. This evaporation opposes the increase in T_a and T_{wet} is thus less sensitive to ambient temperature than T_{dry}. For the same reason T_{wet} is more sensitive to relative humidity than T_{dry}, upon which it has no affect.

Change in wind speed does not have a linear effect on the reference temperatures. The convective heat transfer coefficient is proportional to the square root of the wind speed (see Equations 4.11 and 4.12). As evaporative heat transfer is analogous and opposite to convective heat transfer (see Equations 4.12 and 4.16), T_{wet} is less sensitive to wind than T_{dry}.

Solar radiation affects T_{dry} more than T_{wet}. This is to be expected as T_{wet} is in the shade and only receives diffuse solar radiation.

Figure 4.8b shows the magnitude of the different heat transfer mechanisms on the two reference leaves. The radiation term is the sum of radiative heat exchange between the leaf and the soil, sky, opposite canopy and the back canopy. T_{dry} loses heat via convection and radiation as it is above the ambient temperature. The opposite applies to T_{wet}. It is noted that the convection heat transfer and evaporative heat transfer for T_{wet} are in opposite directions, as the T_{wet} leaf is below T_a.

The results from the HT model's sensitivity agree well with the PCA of the measured weather conditions and reference temperatures in Figure 4.5. The ambient temperature has the largest positive correlation to T_{dry}, and slightly less to T_{wet}. This observation was also made for the HT model. The fact that solar radiation is nearly orthogonal to the reference temperatures in h PCA, agrees with the HT model, as the model predicts that the solar radiation has only a small in-

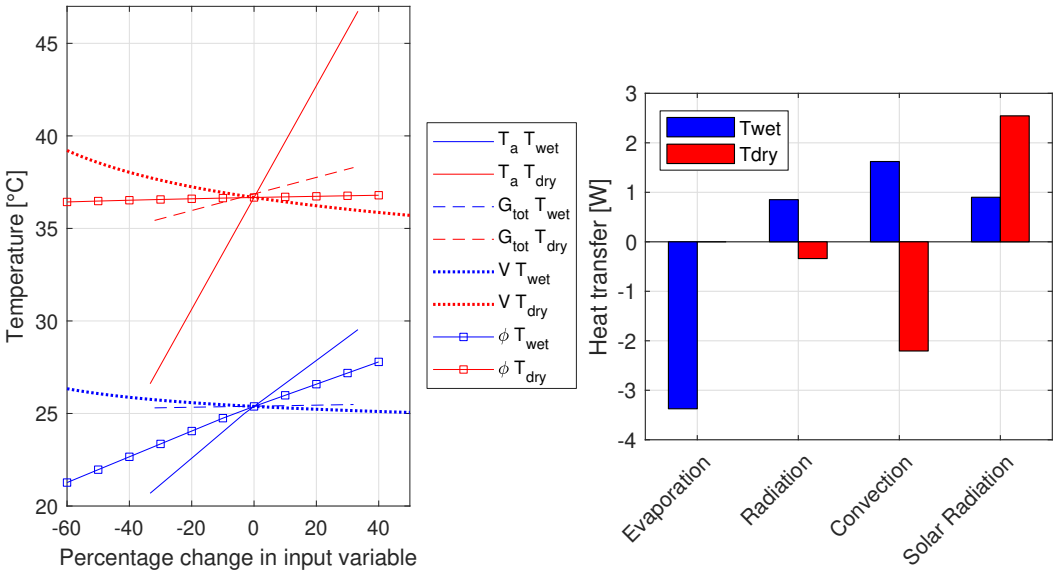

(a) Change in T_{wet} and T_{dry} as the meteorological variables are individually varied. The percentage change is from the nominal conditions.

(b) Magnitudes of HT mechanisms

Figure 4.8. HT model at nominal conditions of $T'_a = 30\,°C$, $\phi = 0.5$, $V = 2\,m/s$ and $G_{tot} = 940\,W/m^2$.

fluence over the reference temperatures. In the HT model sensitivity analysis, the wind speed had a low influence on the reference temperatures, which agrees with the low correlation in the PCA. The relative humidity has a strong negative correlation to the reference temperatures, which is contrary to the HT model, as relative humidity is strongly dependent on ambient temperature. For Figure 4.8a, T_a was kept constant while increasing ϕ.

4.4.2 HT and LEB sensitivity to optimisation parameters

The sensitivity of the calculated T_{dry} and T_{wet} to the optimised parameters listed in Table 4.2 is presented in Figure 4.8. The most sensitive parameter for the HT model is the solar absorptivity of the Vaseline, α_v, and it only influences T_{dry}. The solar absorptivity of the wet leaf has a small effect on T_{wet} and none on T_{dry}.

The angle of incidence error has a strong negative gradient, as the angle of incidence is measured from the leaf normal (see Figure 4.2). The closer the solar angle to the leaf normal, the more radiation it receives. Counter-intuitively, T_{dry} and T_{wet} decrease slightly with increasing direct component of solar radiation. The total solar radiation that reaches the leaf is the sum of direct (around 90%) and diffuse (around 10%) components of radiation. Of the direct component of radiation, a small fraction (because of the low solar angle of incidence) heats up the leaf. As the component of direct solar radiation (f_{dir}) increases, a larger proportion is further attenuated by the effect of the angle of the leaf to the sun and

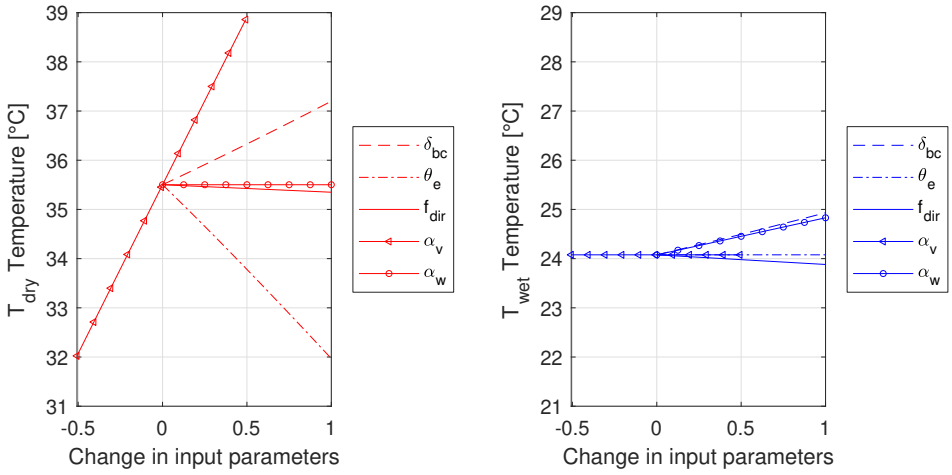

Figure 4.9. Sensitivity of the HT model to the optimisation parameters at nominal conditions of Figure 4.8. The parameters are varied between the lower and upper bounds specified in Table 4.2. and the zero position is the value reached with optimisation.

less radiation reaches the T_{dry} leaf. See equation 4.8 for the sum of the direct and diffuse components of solar radiation. The temperature of T_{wet} decreases slightly with an increase in f_{dir}, as a smaller portion of the solar radiation is scattered diffusely.

4.4.3 Comparison of the different models

The Natural method is an adequate baseline reference temperature method used in many studies. By taking the average of the six measured temperatures in each period, the effects of fluctuations in weather conditions are avoided.

The EMP method, being the simplest method, can be used as a reference when no other data is available. A novel approach was used by taking a temperature between the wet- and dry-bulb temperatures for T_{wet}. This method only takes ambient temperature and humidity into account, which are the two most important weather parameters, as seen in the PCA. It was observed that the model performed worst in periods with high wind speeds.

The unoptimised LEB model had large errors, but the consistency of the direction of the errors allow the values to be usable. As T_{wet} and T_{dry} are under and overestimated, the canopy temperature will not be close to these reference temperatures and the CWSI is guaranteed to be in the range of zero to one. This model has the additional disadvantage of requiring a net radiometer. Other authors such as Sepúlveda-Reyes *et al.* (2016) have successfully implemented LEB models. When correlating the CWSI to the stem water potential (SWP), these authors obtained a r^2 of 0.36 using an LEB method, compared to r^2 of 0.21 when using the Natural method.

The HT method performed the best of all the models. To understand the parameters reached, one must take Figure 4.9 into account. It is noted that the

optimisation parameters have a lesser effect on T_{wet} than T_{dry}, and that θ_e and α_v only affect T_{dry}. As a result, the optimisation has independent control over T_{dry}, using θ_e and α_v. The model thus optimises T_{wet} using the shared parameters (f_{dir} and δ_{bc}) and α_w which influence both T_{wet} and T_{dry}, to optimise T_{wet}. It then uses θ_e and α_v to optimise T_{dry}.

The shared parameters are optimised to values that lower T_{wet} (except for f_{dir}, which has a very small influence). This indicates that the evaporative cooling of the T_{wet} leaf is underestimated, as it is the only method of heat transfer that cools T_{wet}, as seen in Figure 4.8b. In Table 4.5, it is seen that T_{wet} is generally overestimated by the HT model.

In Figure 4.9, the effects of the parameters on T_{dry} are seen. Remembering that δ_{bc} is set by the optimisation of T_{wet}, it is observed that θ_e reaches a value that increases T_{dry}. α_v is in the middle of its range, indicating that the model had very good control over the model's T_{dry} temperature.

The effect of convective heat transfer may be the cause of errors in the HT model. The same model of convective heat transfer applies to both T_{wet} and T_{dry} (heating and cooling the respective surfaces). Had the magnitude of convective heat transfer been lower, then T_{wet} would be at a lower temperature and the optimisation parameters would not reach its limits. T_{dry} would be at a higher temperature and θ_e would not reach its limits. This is however not conclusive evidence and further investigation into the convective heat transfer may improve the results.

4.4.4 Low-cost sensors

When measuring T_{dry}, the MR obstructed sunlight when brought close to the leaf and the steady state temperature of the leaf was disturbed, which can explain the large variation in the data. This was confirmed by noting that the variation between the C3 and low-cost sensors on the shaded T_{dry} leaves (in Section 4.3.2) were lower for all the sensors (results not shown). The induced errors cannot be avoided when using these low-cost sensors, except if a sensor with a very small field of view (FOV) is used from around 0.3 m, not casting shade on the target leaf.

The offset in T_{dry} may be as a result of the reflected temperature from the MR that is higher than the reflected temperature from the opposing shaded side of the canopy and the sky. The opposing canopy and sky contribute most of the radiation heat transfer received by the T_{dry} leaves. Equation 4.2 shows that the radiation emitted by a surface is the combination of its own temperature and reflected temperature. The IR sensors report higher T_{dry} values, even though the leaf temperature is mostly unchanged (the MR only casts a shadow for a few seconds). The MR reaches high temperatures when used in the sun, with IR internal thermistor temperatures as much as 10 K above ambient temperature.

This reflected temperature explanation is motivated by the shaded Vaseline covered leaf temperatures in Section 4.3.2, which has an offset of only ±2 K. In

this case, the opposing canopy is sunlit and the difference between the MR and the canopy temperature is smaller, having a lesser effect on the reported temperature.

One might argue that the radiation emitted by the atmosphere between the leaf and the sensor can have a further influence over the temperature, but Costa *et al.* (2013) and Jones (2004) state that it only needs to be taken into account with airborne and satellite images. Figure 2.1 indicates that the atmospheric transmissivity of the air is very high at distances below 1 m.

The reflectivity of the Vaseline-covered leaf may higher than that of the water-coated leaf, suggested by the fact that the temperature offsets are not observed with T_{wet}. A constant value of $\epsilon = 0.96$ is used in literature. Watson (1933) found that Vaseline can decrease the emissivity of leaf material, but does not specify a value. Most authors use a value of 0.96 for grapevine leaves and do not report using different emissivity values for reference leaves. The value of 0.96 was thus used throughout this study. Jones (2004) found that a emissivity error of 1% can lead to a temperature error of 0.75 K at an ambient temperature of 27 K°C. A change in the emissivity of the Vaseline would be taken into account on the C3 as well, and the temperature offset would remain unexplained.

The IR35 sensor performed the best when taking both T_{wet} and T_{dry} into account. The IR12 sensor only focuses on a small area of the leaf and may not give a good representative leaf temperature. In contrast, the IR90 sensor has high variability when measuring T_{dry} as it focuses on a large area and may include non-leaf background material.

4.5 Conclusion

Different conditions for the application of the Natural method were compared and it was found that an attached Vaseline-covered leaf in the sun and a water-covered leaf in the shade provide the most consistent and applicable reference temperatures. After these conditions were established as the baseline method, it was used to measure target temperatures for the optimisation models.

Optimisation strategies were successfully implemented to calculate parameters for different models of calculating CWSI reference temperatures. The most complex method (HT) performed the best when evaluating it against training data, but requires additional refinement in calculating the convective heat transfer. The HT method could calculate T_{wet} and T_{dry} to within 0.5 K and 1 K respectively. The EMP method provided good results, considering that it only requires temperature and humidity data. The LEB model performed poorly in calculating T_{wet}, and T_{dry}, but is was explained that the equations were not derived for these specific conditions.

Lastly, the low-cost sensors were not found to be reliable in measuring T_{dry}, but could measure T_{wet} to within 2 K. It was found that the IR35 sensor performed the best out of the low-cost sensors.

Chapter 5

Canopy Temperature

5.1 Introduction

5.1.1 Canopy temperature measurement

Canopy temperature is defined as the average of the plant's leaf temperature distribution (Fuchs, 1990). This temperature is approximated with the use of infrared (IR) sensors, by taking the average temperature of the leaves in the field of view (FOV) of the sensors. Pou *et al.* (2014) found that selecting a region of interest (ROI) from an entire canopy's thermal image, rather than single leaves, provides an appropriate method to define canopy temperature. The authors explain that using large areas decreases disturbances caused in the microclimate of the canopy.

Accurate canopy temperature measurements are essential for the determination of a plant's water status, but they are not trivial to determine (Fuchs, 1990). Background temperatures, observed due to gaps in the canopy, can introduce measurement errors. To mitigate these effects, IR camera users can manually select ROIs in the thermal image. For single-area sensors, these errors are unavoidable and only measurements close to the canopies can ensure that no background is included in them.

5.1.2 Chapter Objectives

The main objective of this chapter is to determine whether the low-cost sensors can measure the same canopy temperatures as the Flir C3, which is used as a baseline measurement and reference canopy temperature for this chapter. To accomplish this, the low-cost sensors are used at different distances to accommodate for the differences in sensor FOVs. The use of a white panel (WP) as background is investigated to determine whether it can improve the results of the temperature measurements.

A second objective is to determine whether methods of calculating representative temperatures for the IR camera sensors can eliminate the process of man-

ually selecting ROIs on an normal images.

5.2 Materials and methods

5.2.1 Measurement procedure and study site

In the same experiment as described in Chapter 4, additional measurements were taken of the canopies to investigate the different IR sensors. On six of the seven days listed in Table 4.3, five sensors were used to measure the temperature on both sides of nine plants. Measurements were taken at 2 m, 1 m and 0.5 m on both sides of the canopy. All these measurements were taken with and without a WP as background to attempt to eliminate the effect of the background sky and soil temperatures. Measurements were done at 12:00 and 14:00, roughly one hour before and after local solar noon respectively. In total, 24 measurements were taken per plant per day.

The measurement sequence on both sides of each plant was: (i) C3 at 2 m; (ii) measurement rig (MR) at 2 m; (iii) C3 at 1 m; (iv) MR at 1 m; (v) C3 at 0.5 m; (vi) MR at 0.5 m. The 2 m measurement was taken aiming at the centre of the canopy. Thereafter as the sensors were moved closer, the measurement was aimed at dense areas in the canopy.

5.2.2 Canopy background

A WP was constructed from sheets of white Correx plastic sheeting and an aluminium frame, making it light enough to carry around in the vineyard. The panel, at 3.5 m × 2.5 m is larger than the canopy of the vines. This WP is used instead of the black panel mentioned in Section 2.6, to differentiate between the background and the shaded leaves in the canopy. Giuliani and Flore (2000) chose a black panel to heat up above the canopy temperature for thermal thresholding. With the single-area sensors, that is not possible and a hot background panel would further interfere with the results.

5.2.3 IR camera representative canopy temperatures

Masked temperature

An accurate reference canopy temperature is required for evaluating low-cost sensors and array analysis methods. A manual process of selecting only leaf material from the red-green-blue (RGB) image taken from 2 m ensures that the maximum number of canopy leaves is taken into consideration for the reference canopy temperature.

To accomplish this, a Matlab program was written to present the thermal and RGB images and allows the user to select the ROI which is used for temperature calculations. An example of the masking process is presented in Figure 5.1.

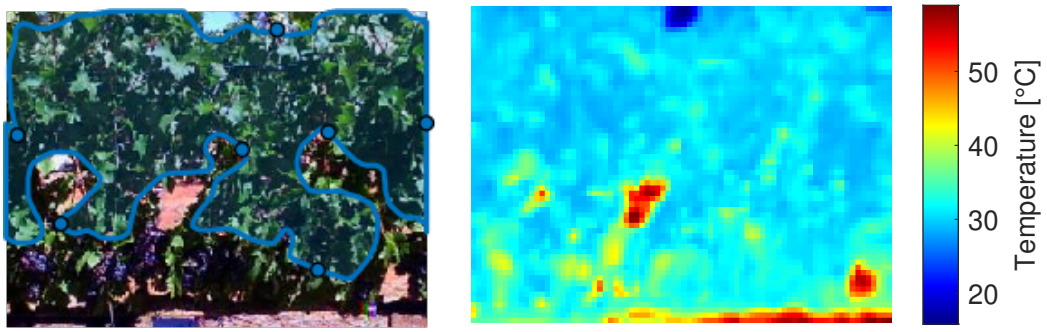

(a) RGB image with manually drawn mask

(b) Thermal image of the canopy where pseudo-colours are used to indicate temperature

Figure 5.1. Masked RGB image of canopy with mask and the accompanying thermal image

Only leaf material is carefully selected while avoiding background, especially sky, which has a very low temperature measurement with an IR sensor, and the soil, which can measure upwards of 55 °C. The representative canopy temperature is then calculated as the average temperature of all the selected areas in the mask. This reference canopy temperature method is referred to as the 'Mask' method.

Filter temperature

Another method to eliminate non-leaf material is to use the crop water stress index (CWSI) reference temperatures (T_{wet} and T_{dry}, taken by the same sensor) as thresholds to eliminate thermal pixels (Jones, 2002; Gutiérrez *et al.*, 2021). An example of this approach is shown in Figure 5.2. This automatic method can be applied to the IR_Arr and the C3 sensors. This method has the drawback of not being able to discern between leaf and non-leaf material. The stem or grape berries are likely to be within the range and will affect the average temperature. This method is referred to as the 'Filter' method.

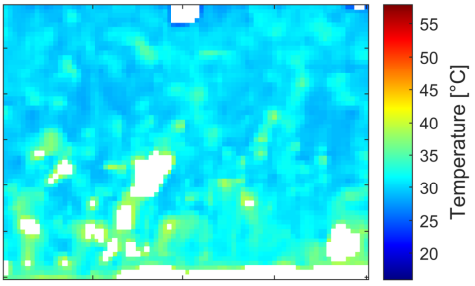

Figure 5.2. Thermal image filtered with CWSI reference temperatures. The white space on the figure refers to temperatures that are out of the CWSI range. The same image as Figure 5.1 is used.

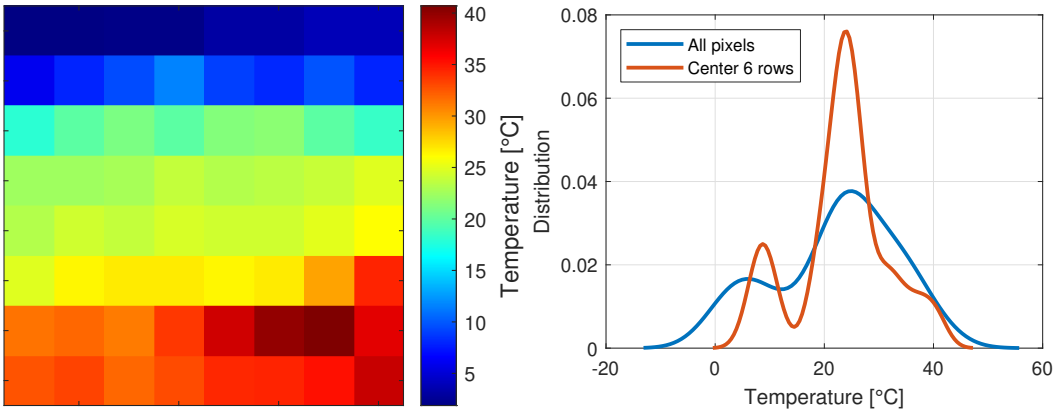

(a) Temperature matrix **(b)** Temperature distributions

Figure 5.3. Temperature matrix and distribution of an IR_Arr canopy measurement

Peak temperature

A simple method of estimating a representative canopy temperature is to calculate the most frequent temperature in the temperature matrix. To accomplish this, the values are divided into 100 bins, equally scaled between the minimum and maximum temperatures. The bin with the most values is selected as a representative canopy temperature. This is synonymous with taking the peak value of a histogram of the temperature values. As the canopy fills the largest portion of the camera FOV, the most frequent temperature can be taken as a representative canopy temperature that ignores the effects of background temperatures. This method is referred to as the 'Peak' method.

In Figure 5.3 the temperature distribution is presented alongside the temperature matrix. Two temperature distributions are presented, one with all the values included and one where the bottom and top rows on the temperature matrix are omitted to avoid sky and soil temperatures. These two distributions indicate that the method of selecting the peak from the histogram works well to eliminate soil and sky temperatures, as the peaks are at the same temperature of 24.6 °C.

Average temperature

A simple average temperature of all the values in the matrix is provided to ensure that the proposed methods can outperform an approach where no complex calculations are done.

5.2.4 Single-area sensors

The single-area sensors capture an entire area and report a weighted average temperature, as discussed in Section 3.2.2.

Gaps in the canopy, allowing background surfaces to affect the canopy temperature readings, cannot be avoided. By selecting sensors with appropriate

(a) Non-stressed plant, SWP = −1.028 MPa **(b)** Stressed plant, SWP = −1.540 MPa

Figure 5.4. Stressed and non-stressed vines captured from 2 m with white panel background on 23 February 2021

FOVs at the different distances, these errors can be minimised. The water-stressed plants have more gaps in their leaves, exposing the hot soil in the background. This can lead to false positive correlations of high temperatures for the high water-stressed plants when investigating CWSI. Figure 5.4 shows the difference between a stressed and non-stressed plant. Both plants have small gaps in the leaves, but the stressed plant has significant areas of missing leaves. It is therefore expected that these sensors will perform better at closer distances.

5.2.5 Area measured by sensors

Figure 5.5 shows the different areas captured by the sensors at the three measurement distances. A single vine is pruned to 2 m high, with cordon height at 0.8 m and row spacing of 2 m. From Figure 5.5 it is clear that the IR_Arr and IR90 sensors will measure areas all around the target plant when measured from 2 m. The strategies mentioned above are used to correct for this. It is important to capture as much leaf material as possible while minimising the amount of background that is captured.

5.2.6 Temperature comparisons

All the sensors' temperatures are compared to the C3 at 2 m with a WP background. As seen in Figure 5.5, the C3 includes the entire canopy, and the small areas at the top and bottom of the canopy are omitted with the masking process. The WP with manual image masking ensures that background temperatures are avoided. Each of the six measurements taken with all the sensors is compared to this reference canopy temperature measurement.

The measurements are grouped to compare only the distances and background. The purpose of this experiment is to determine under which conditions

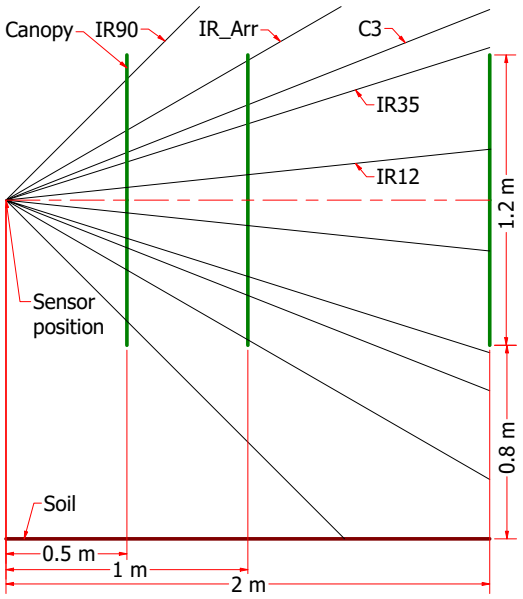

Figure 5.5. Side view of the FOVs of the different sensors at the three measurement distances. The FOV from the top is less important as the canopies are 2 m wide and are bordered by adjacent canopies under the same irrigation treatment.

low-cost sensors can accurately measure canopy temperature. In the next chapter it will be determined under which measurement conditions the canopy temperature is the best indicator for plant water stress.

5.3 Results and discussion

5.3.1 Automatic IR camera methods

The mean absolute errors (MAEs), root mean squared errors (RMSEs) and mean bias errors (MBEs) between the reference canopy temperature and the automatic IR camera methods are presented in Table 5.1.

Firstly, looking only at the different backgrounds with the Mask temperature, it is seen that the errors are larger when no WP background is used. At the closest distance, however, the WP does not matter as the camera's entire FOV is focused on canopy material. The best distance to determine accurate canopy temperature with the Mask method and no WP is from 2 m. This is to be expected as the entire canopy is taken into account for a representative temperature.

The Peak method does not perform well, apart from at 2 m with a WP, where it performs the best of all the methods and configurations. The MBE shows that the Peak method underestimates the canopy temperatures, while the RMSE shows that the variation in the errors is not large. This indicates that the canopy temperatures are generally positively skewed. This method is inadequate as it does not perform well without a WP or at closer distances.

Table 5.1. Error matrix of canopy temperatures comparing the automatic IR image methods to the masked C3 measurements

Measure	Distance [m]	WP	Mask	Filter	Peak	Average
MAE	2.0	✓	Ref	0.43	0.26	0.51
		✗	0.60	0.62	0.81	1.30
	1.0	✓	0.38	0.37	0.54	0.38
		✗	0.58	0.57	0.83	0.76
	0.5	✓	0.63	0.51	0.70	0.53
		✗	0.65	0.54	0.90	0.59
RMSE	2.0	✓	Ref	0.51	0.36	0.59
		✗	0.78	0.80	1.12	1.66
	1.0	✓	0.48	0.66	0.66	0.68
		✗	0.81	0.73	1.05	0.96
	0.5	✓	0.82	0.67	0.88	0.69
		✗	0.84	0.71	1.11	0.76
MBE	2.0	✓	Ref	0.32	-0.16	0.44
		✗	-0.17	0.06	-0.51	1.13
	1.0	✓	-0.17	0.05	-0.46	0.11
		✗	-0.21	-0.04	-0.67	0.42
	0.5	✓	-0.11	-0.14	-0.62	-0.06
		✗	-0.24	-0.25	-0.84	0.05

Note: All error values are in K. Negative errors are coloured and scaled blue and positive errors are coloured and scaled red

Apart from 2 m, the Average method performs better than the Peak method when no WP is used, but the errors are larger than those of the Filter method. It is not expected that this model performs well at long distances, due to the inclusion of non-leaf background material. It is observed that a simple average temperature performs almost as well as the best method at close distances where the entire FOV of the sensor is filled by canopy material.

Overall, the Filter method performs the best of all the automatic methods when no WP is used. This method performs well at all distances, and the best at 0.5 m. As discussed in Section 5.2.3, the stem and fruit, which are within the CWSI reference temperature thresholds, can skew the average of the filtered temperature. As a result, the method performs better at 1 m than at 2 m, where the stem and fruits are not visible. Moving too close to the canopy can result in a temperature that is not representative of the entire canopy. The MBE at 1 m without a WP is −0.04 K, which is very close to zero, and the temperatures are thus not

skewed in either direction.

Sepúlveda-Reyes *et al.* (2016) investigated thermal image thresholding by using CWSI reference temperatures from the method described by Jones (1999) to filter aerial and ground-based vineyard thermal images. Sepúlveda-Reyes *et al.* (2016) found that only 70% of leaf material was correctly identified on the sunlit side of the canopy in the ground-based measurements. The authors suggest that measurement of reference leaves at different angles with respect to the sun increased the variability of the measurements and lead to the misclassification of leaf material. In our study, special care was taken to identify and measure reference leaves oriented normal to the canopy, as indicated in Section 4.2.3

Gutiérrez *et al.* (2021) successfully used thermal thresholding to calculate a representative canopy temperature from thermal images obtained by a thermal camera attached to an all-terrain vehicle. A correlation of $r^2 = 0.71$ was found between CWSI stem water potential (SWP).

For the Mask method, the temperature measurement accuracy does not change significantly as the measurement distance changes. The error of the Mask method is less than 1 K in all the cases. The measurement distance and thus the camera FOV does not have a significant effect on the T_c measurement, which is an advantage of thermography. Pou *et al.* (2014) found that the selecting a ROI of an entire canopy is more appropriate than selection a ROI of a single leaf in the canopy, as disturbances in the microclimate of individual leaves are minimised with the large area measurement.

5.3.2 Single-area IR sensors

To find the best measurement distance for the low-cost IR sensors, one must keep Figure 5.5 in mind. At 2 m, the IR12 sensor captures a small area of the canopy and the IR35 sensor measures slightly over the top and bottom of the canopy. Only a small part of the IR90 sensor's FOV is on the canopy at 2 m. At 1 m, the IR35 sensor captures more than half of the canopy, excluding the top and bottom surfaces where the extreme background temperatures occur. At this distance, about half of the IR90 sensor's FOV is filled by the canopy. At 0.5 m the IR12 and IR35 sensors' FOV is on even smaller portions of the canopies, while the IR90 sensor focuses on the entire canopy. This is the only distance where the IR90 is expected to measure representative canopy temperatures.

The results of the temperature error analysis for the low-cost sensors are presented in Table 5.2. The sensor temperatures are again compared to the masked canopy temperature, with a WP, using the C3 from 2 m.

As expected, the IR90 improves as the distance decreases. The smallest error is observed at 0.5 m with the WP. The WP was not expected to make a difference at this short distance, but it may cover gaps at diagonal angles in the canopy that allow the sensor to measure soil or sky temperature. A relatively low error is observed at 2 m without the WP. It may be that the low sky temperatures above the canopy and the high soil temperatures below the canopy cancel out, but it

Table 5.2. Canopy temperature error matrix of the low-cost sensors compared to the masked C3 measurements

Measure	Distance [m]	WP	IR12	IR35	IR90	IR_Arr Peak	IR_Arr Filter
MAE	2.0	✓	1.96	2.28	3.04	8.96	8.74
		✗	2.60	2.14	2.19	8.17	8.91
	1.0	✓	1.95	2.17	3.11	10.30	10.10
		✗	2.21	2.47	2.51	10.14	9.76
	0.5	✓	2.05	2.32	1.94	10.36	10.29
		✗	2.08	2.66	2.34	10.28	10.37
RMSE	2.0	✓	2.32	2.70	3.58	9.70	9.40
		✗	2.87	2.58	2.69	8.92	9.54
	1.0	✓	2.41	2.37	3.62	11.00	10.80
		✗	2.62	2.78	3.13	10.80	10.38
	0.5	✓	2.86	2.51	2.20	11.02	10.96
		✗	2.74	2.87	2.66	10.93	11.02
MBE	2.0	✓	1.90	-2.23	-2.76	-8.95	-8.73
		✗	2.57	-1.54	-1.29	-8.13	-8.90
	1.0	✓	1.74	-2.17	-3.04	-10.29	-10.09
		✗	2.16	-2.46	-1.82	-10.12	-9.76
	0.5	✓	1.75	-2.32	-1.91	-10.35	-10.29
		✗	1.89	-2.66	-2.29	-10.27	-10.37

Note: All error values are in K. Negative errors are coloured and scaled blue and positive errors are coloured and scaled red.

is clear from Figure 5.5 that this measurement cannot be reliable. The relatively large errors between the RMSE and MAE indicate that there is a large variation in the errors at 2 m.

The IR35 sensor performs the best at 2 m with no WP, where most of the canopy is in the sensor's FOV. The small areas that do capture sky and soil temperatures are on the outer section of the sensor's FOV, which is weighted less than the central areas in the FOV (see Figure 3.2). Unlike the IR90 sensor, the smallest errors were observed without a WP. The error bias for this sensor is negative, indicating that the sensor underestimates the canopy temperatures. The difference between the MAE and RMSE of this sensor is generally lower than the other two low-cost sensors, indicating that its error variance is lower.

The IR12 sensor performed the best of the low-cost sensors. As expected, due to the small FOV of this sensor, the best temperature measurements were taken from the furthest distance. In contrast to the other sensors, the IR12 sensor

overestimates the canopy temperature, as seen with the MBE. The large MAE of 2.60 K at 2 m with no WP is unexpected. As only a small portion of the canopy is in the sensor's FOV, it was assumed that the background temperature would not affect it significantly. But due to the low sensor FOV, a small gap in the canopy has a large impact on the temperature measurement.

Considering the relative performance of the low-cost sensors, the IR35 sensor at 2 m with no WP is recommended for canopy temperature measurements. The slightly better MAE (0.18 K) performance of the IR12 with a WP is outweighed by the physical implications of requiring a WP background. The IR35 under these conditions ensures that a large area of the canopy is measured, while focusing on the centre of the canopy where the most leaf material is.

Looking at the MBE in Table 5.2, it is evident that the IR12 sensor has a positive error bias while the IR35 and IR90 have negative error biases. The sensors' spectral bands, mentioned in Section 3.2.2, may be responsible for these offsets. The IR12 sensor detects IR radiation in a lower spectral band than the C3. Albedo, which is reflected solar radiation (in the <4 µm spectral band (North, 2015)), is detected by this sensor which then reports an overestimated target temperature. Figure 5.6a affirms this argument, where it is observed that the temperature error is greater (positive) on the sunlit than on the shaded side of the canopy. The shaded side errors are also positive, as some sunlit leaves are still visible from the shaded side of the canopy, due to gaps in the canopy and the high solar angle of incidence. Leigh *et al.* (2006) emphasises the need to use IR sensors that operate in the long-wave band when measuring plant leaf material in sunlight. The authors developed a method of taking a temperature measurement with 1 s after shading the target leaves, to negate the effect of the albedo.

The calibration experiment did not account for the effect of albedo, as it was done in laboratory conditions with no sunlight. It was not expected that the albedo effect would be as significant. The higher spectral band of this sensor might decrease the sensor's accuracy in determining an accurate T_c for the CWSI, which is investigated in the next chapter.

The IR35 and IR90 sensors consistently measure a lower temperature than the C3. The C3 canopy temperature is calculated by taking a reflective temperature into account, while the low-cost sensors simply use an on-board ambient temperature measurement to compensate for the reflected radiation (see Appendixes A.2 and A.3). Jones (2018) indicates that the environmental radiation incident on the measured surface can have a significant effect on the object's apparent temperature. The ambient temperature is an overestimation of the reflected temperature, as the sky and opposite canopies are the dominant components of the reflected radiation. The sensor's on-board temperature calculation subtracts the perceived effect of the reflected temperature. As a result, the low-cost sensor reports a lower temperature than the C3, which has a more accurate measurement of the reflected temperature. In Figure 5.6b, it is observed that the error is larger on the sunlit side of the canopy, where the opposing canopy as well as a portion of the soil are shaded. The lower temperature of this shade causes

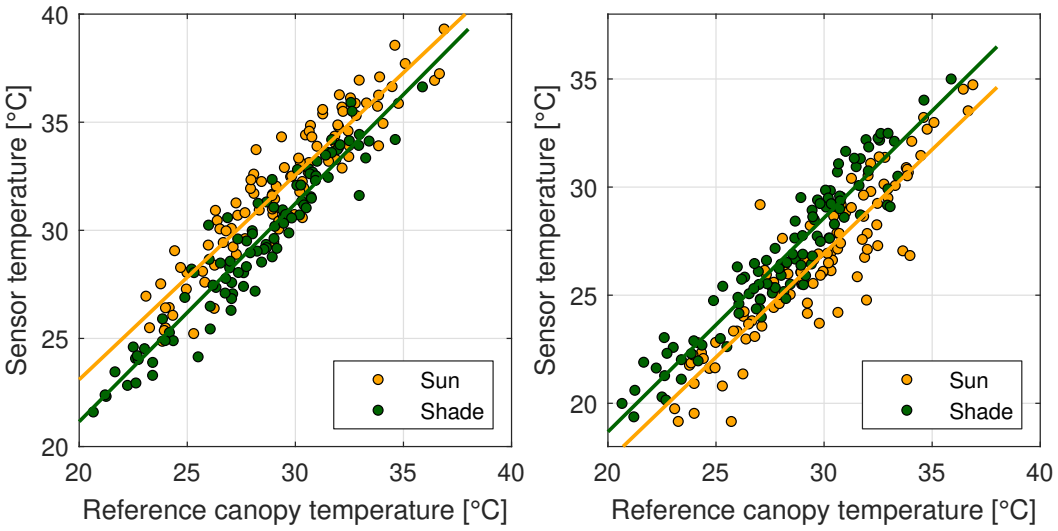

(a) IR12 **(b)** IR35

Figure 5.6. Canopy temperature differences between sunlit and shaded canopies, taken with white panel from 2 m

a larger reflective temperature error in the sensors on the sunlit side than on the shaded side of the canopies. This effect is not noticed in the IR12 sensor, in which case the error is assumed to be dominated by the albedo effect.

Another cause for the underestimation of temperature may be the inclusion of sky in the FOV of the IR35 and IR90 sensors. The IR12 sensor at 2 m is pointed horizontally and is unlikely to include sky in its measurements. The IR35 and especially the IR90 have a significant portion of the FOV pointing upwards and can thus be influenced by low sky temperature measurements.

5.3.3 IR array methods

The IR_Arr sensor performed very poorly. In Table 5.1 it is seen that the mean absolute errors (MAEs) are around 10 K using both the Peak and the Filter methods. These large errors were not observed with the T_{wet} and T_{dry} temperatures in Section 4.3.4.

In Figure 5.7a, the sensor temperature is plotted against the reference canopy temperature. It is observed that the slopes of the sensor temperatures are very high on the individual dates, and as a result, the overall correlation between the sensor and the reference canopy temperature is poor. It is further noticed that the 10 K is not a constant offset, but is accompanied by significant noise. Recalculating the errors by removing the calibration curve discussed in Chapter 3 does not improve the results.

This sensor, which can be used to observe the temperature distribution shown in Figure 5.3a, did serve a purpose in being used to aim the other sensors. The

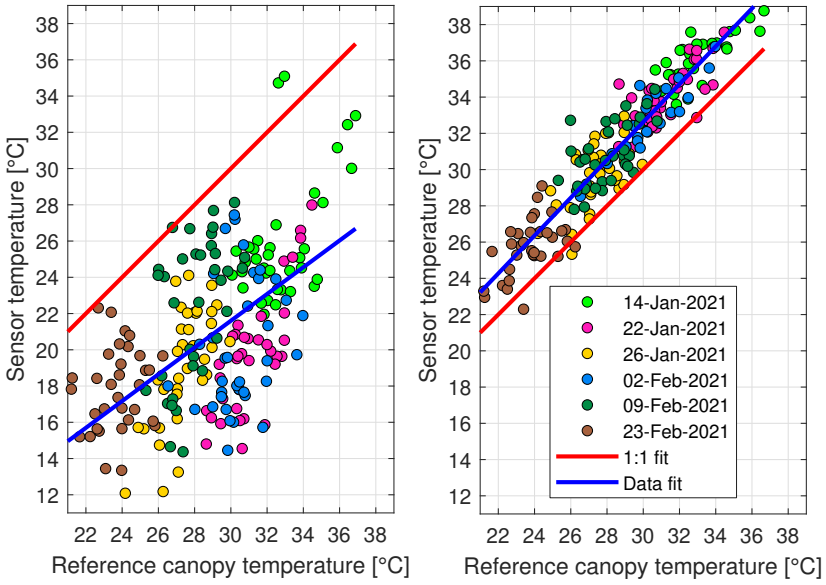

(a) IR_Arr **(b)** IR12

Figure 5.7. Scatter plot of sensor temperatures vs. reference temperatures. Measurements taken from 1 m with no WP. The same legend applies to both plots.

sensor is, however, not useable for research or commercial purposes in measuring canopy temperature.

The selected IR array type sensor was not successful in this study, but other studies have implemented similar sensors successfully. Noguera *et al.* (2020) measured CWSI in an olive orchard with a low-cost IR array type sensor. They used a Melexis MLX90620 IR sensor (16×4 pixels) to measure canopy temperatures and found a correlation of $r^2 = 0.90$ between CWSI and pre-dawn water potential (only 8 plants were measured on a single day).

5.4 Conclusions

It was established that the low-cost IR35 sensor, measuring from 2 m, can determine the canopy temperature to within 2.5 K. The different spectral ranges of the sensors and the method of calculating the reflective temperature of the IR measurement were identified as sources of erroneous T_c measurements with the low-cost sensors. In the next chapter, it is investigated whether the single-area low-cost sensors can be used to accurately measure CWSI.

The evaluation of automatic methods of IR camera representative temperature calculation was accomplished by comparing three methods. The Filter method which uses T_{wet} and T_{dry} as temperature thresholds to eliminate values in the temperature matrix proved to be the most successful. For commercial purposes, this method could prove useful, as it requires no image analysis from the operator while providing accurate canopy temperature measurements.

Chapter 6

Crop water stress index

6.1 Introduction

6.1.1 General introduction

Even though thermography is emerging as a robust and non-invasive strategy to assess plant water stress of vineyards, it has not been widely adopted (Garcia-Tejero *et al.*, 2016). The use of a stress index which normalises the canopy temperature to the instantaneous environmental conditions of the measurement is required.

The crop water stress index (CWSI) is such an index which depends on the canopy temperature and two reference temperatures. The requirement of three temperatures for the calculation of CWSI introduces measurement uncertainty.

$$CWSI = \frac{T_c - T_{wet}}{T_{dry} - T_{wet}} \quad (2.3)^*$$

Practical measurement uncertainties such as the canopy side, the use of a white panel (WP) background, time of day and measurement distance are not consistent in literature. The high cost and complicated image analysis techniques of IR cameras make low-cost single-area infrared (IR) sensors appealing. Clarity with regard to the best measurement parameters and IR sensor requirements will accelerate the commercial adoption of the CWSI technique.

6.1.2 Chapter objectives

The first objective is to establish whether canopy temperature is an accurate indicator of plant water stress. Thereafter, the need for a normalising stress index must be demonstrated.

The main objective of this chapter is to investigate under which measurement parameters low-cost sensors can be used to accurately determine CWSI. In addition, it is evaluated whether the best performing automatic temperature calculation method from Chapter 5 can be used to determine CWSI.

Finally, it is investigated whether the reference temperature strategies developed in Chapter 4 can be used for CWSI calculation with the different sensors. The overall goal is to determine whether a low-cost sensor, along with an automatic reference temperature method can be used as an indicator of plant water stress.

6.2 Materials and methods

6.2.1 Reference plant water stress measurement

Stem water potential (SWP), discussed in Section 2.5.3, is a comprehensive indicator of water shortage in plants (Choné *et al.*, 2001) and was taken as the reference water stress measurement for this study. A pressure chamber (PMS Instrument Company, model 1505D, Albany, USA) was used to perform the measurements. SWP was measured within 15 minutes of taking the thermal images. So as to reduce human error, the same operator performed all the SWP measurements. Full-grown and healthy leaves were selected from the middle of the canopy of each vine facing the shaded side of the canopy, to avoid overheating. To diminish leaf transpiration, each selected leaf was covered with aluminium foil inside a plastic zip bag at least 1 hour before the measurements (Choné *et al.*, 2001).

SWP is used as a baseline for plant water stress when comparing IR sensors. Carrasco-Benavides *et al.* (2020) points out that some studies compare the resolution of thermal images by linear regression between two sensors measuring the same variable (Martin, 2000). Linear regression is only recommended for comparing a new method with an established method and assumes that the new method is the source of error (Stockl *et al.*, 1998). The established SWP is used as a reference and the correlation coefficient of CWSI to SWP is used to evaluate the different measurement parameters and sensors.

6.2.2 CWSI reference temperatures

In many studies (e.g., Costa *et al.* (2013) and Zhou *et al.* (2021)) reference leaves or surfaces are placed in the field of view (FOV) of the canopy's thermal images to record the instantaneous reference temperature at T_c measurement time. For this study, single-area IR sensors are used, which cannot differentiate between different temperatures in its FOV. For consistency, reference temperature measurements were taken separately from canopy temperatures, with all the sensors.

The reference temperatures, recorded as described in Chapter 4, were used for this chapter.

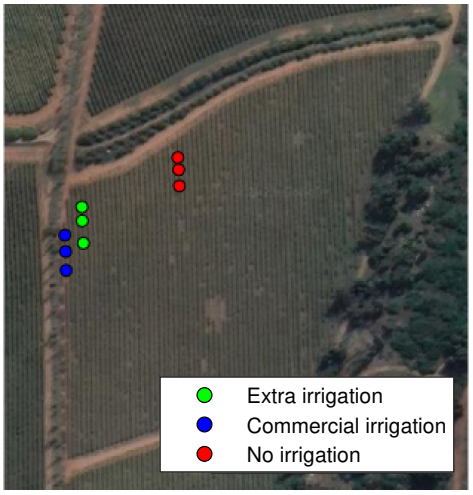

Figure 6.1. Satellite image of measurement site (Google Earth, 2021)

Figure 6.2. Grapevines at measurement site

6.2.3 Experimental setup

To have a wide range of water conditions during the growing season, three water regimes were implemented in the field with three replicates each (vine level): (i) Control vines were irrigated according to the commercial practice defined by the viticulturist; (ii) Dryland, where the vines were not irrigated during the entire season and received water only from rain; (iii) Full irrigation, in which case the vines received additional water every week to keep a minimum SWP value of −0.9 MPa. SWP below −0.9 MPa is classified as weak water deficit (Van Leeuwen *et al.*, 2009) (negative pressures are discussed in Section 2.5.3.) A total of 300 L of water was given to the fully irrigated plants in addition to the commercial irrigation, to control the water deficit. The regions were selected based on data from the previous season which indicated significant differences in stress levels, determined with SWP. The physical distances between the sets were taken into consideration to minimise the time taken to travel between the different sets. A satellite view of the measurement site is presented in Figure 6.1, and a view of a grapevine row is presented in Figure 6.2.

Taking into account that measurements take about 30 minutes, measurements were started at 11:45 and 13:45, approximately one hour before and after solar noon, respectively. Garcia-Tejero *et al.* (2016) suggest that between 11:00 and 14:00 (locally) is the best time of the day to collect thermal data that is physiologically meaningful.

6.3 Results and discussion

6.3.1 Physiological response

The plant water stress, measured with SWP, is presented in Figure 6.3. Initially, on 14 January, there is only a slight difference in the SWP of the groups. This difference between the groups increased as the season progressed, and reached a maximum difference of 1.12 MPa at the end of the season. It was observed that all the plants recovered some water deficit between 2 and 9 February. No rain fell during this period, but the block was irrigated for 12 hours (at 2.3 l/h) on 3 February. Some water did reach one of the stressed plants on 7 February and 26 February, as its SWP is significantly higher than the other two plants in its group. This is not a problem as a wide SWP range is still observed between the minimum and maximum SWP. The extra irrigation of the fully irrigated plants ensured that these plants did not reach a high water stress level. It is observed that the commercial irrigation was implemented when a moderate level of plant water stress was reached, according to Table 2.2.

The SWP measured is in a similar range to that of Poblete-Echeverria *et al.* (2017) who measured SWP to be from −0.5 MPa to −2.0 MPa (cv. Carménère). The seasonal progression of the difference between irrigated an non-irrigated SWP values is similar to that of Fernandes de Oliveira *et al.* (2021) (cv. Cannonau). The authors measured SWP of −0.6 MPa for both groups in the initial path of the season and recorded a minimum SWP of −1.65 MPa for the non-irrigated vines at the end of the season and the maximum difference between the irrigation groups were 0.4 MPa. The SWP values measured in this study are thus in the expected range and cover a wide range of plant water stress values.

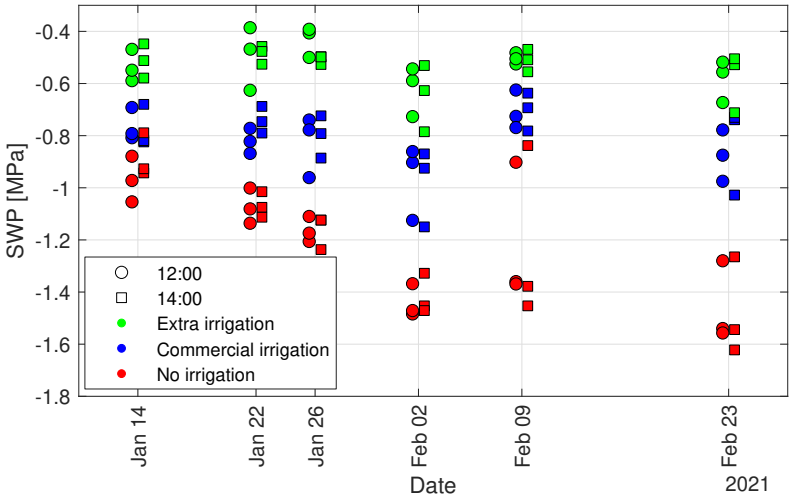

Figure 6.3. Scatter plot of SWP over time

6.3.2 Solar angle of incidence

The solar angle of incidence at the middle of the measurement time is presented in Figure 6.4a. The angle of incidence is dependent on measurement date, time, location and the orientation of the canopy. As the season progresses, the angle of incidence decreases if the measurement time is kept constant. It was, however, observed that the measurement time had a larger effect on the angle of incidence than the seasonal shift in the solar zenith angle.

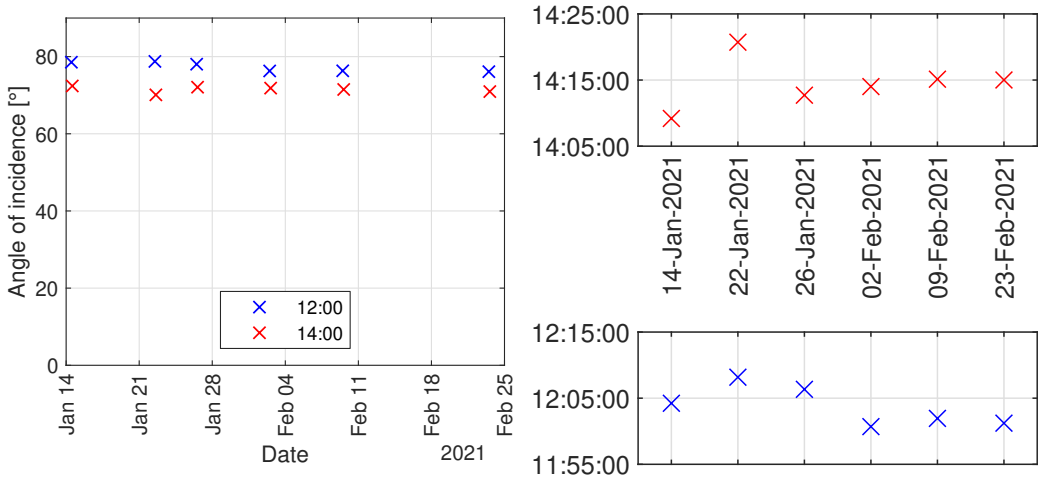

(a) Solar incidence angle

(b) Measurement time

Figure 6.4. Solar incidence angle and measurement time

6.3.3 Thermal response of vines

Figure 6.5a presents the correlation between SWP and canopy temperature on the different days. There are strong correlations between the variables on any given day (r^2 ranging from 0.41 to 0.95), but in general, over all the days, there is no correlation. The results agree with Gutiérrez *et al.* (2018) that indicate that the correlation between CWSI and SWP is greater on any given day than when days are combined, but individual days provide little information and days should always be combined.

It is noted that there is a definite change in the slope of the curves after 2 February. This coincides with the phenological stage of veraison, where the plant changes focus from using energy for plant growth to berry growth. The data is therefore split into two groups: pre-veraison (Stage II) and post-veraison (Stage III). The CWSI in the different stages is presented in Figure 6.5b. Fernandes de Oliveira *et al.* (2021) found a similar change in grapevine thermal response and suggests that as the phenological stages progress, lignification along the main shoot causes variation in water transport along the main shoots of the vines. The

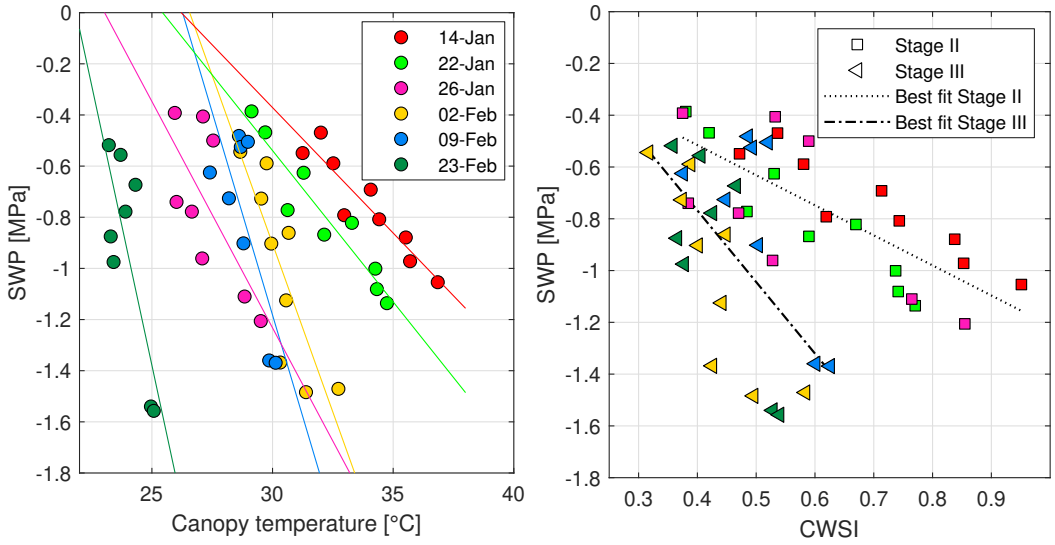

(a) SWP vs T_c' on different days

(b) SWP vs CWSI on different days

Figure 6.5. Scatter plot of SWP vs T_c' and SWP vs CWSI for the C3, with a white panel at 2 m, on the sunlit side at 12:00. The colour legend of (a) applies to (b) as well.

change in water transport results in different thermal responses of the vines in the different growth stages. The authors accounted for this by adjusting their stress index by adding different constants for the different major phenological stages. It has furthermore been suggested that at the end of the season, some leaves approach a senescent condition, where these leaves are not representative of the entire canopy, which might negatively influence results(Moller *et al.*, 2007).

Bellvert *et al.* (2014) provided evidence that the physiological stages of the grapevine affect the correlation and the equation between leaf water potential and CWSI (using the vapour pressure deficit (VPD) method described in Section 2.4.1). The authors explain that a change in the solar zenith angle affects the canopy temperature as the season progresses. As the sun's maximum solar zenith angle decreases from summer to winter, the fraction of shaded leaves in the canopy changes.

In this study two periods are separated and presented, but not adjusted with constants. The CWSI equation is used without modifications. The observed difference in the CWSI response in the different phenological stages agrees with Mwinuka *et al.* (2021) who found differences is the CWSI correlation to leaf water content in the different vegetative stages of African Eggplant

The SWP range (Figure 6.3) is larger in the second stage, and one would expect better correlations between CWSI and SWP, but in Figure 6.5a it is seen that the temperature variation in this period is lower than in the first period. This period after veraison, is important for viticulturists as the water stress in the vines has an influence over the ultimate wine quality.

6.3.4 CWSI Comparisons

The full matrix of CWSI to SWP correlations under the different measurement techniques, is presented in Table 6.1. The correlations were calculated independently for both stages, using 3 days per stage. Each r^2 value is thus calculated with 27 points, as there are nine target plants in the study. On 2 February, the IR12 sensor became disconnected, and the high correlations for this sensor in stage III are, in part, due to a lower number of measurements.

Table 6.1. CWSI vs SWP correlation matrix

Side	Sunlight	Distance [m]	WP	Mask		Filter		IR12		IR35		IR90	
				Stage II	Stage III	Stage II	Stage III	Stage II	Stage III	Stage II	Stage III	Stage II	Stage III
East	Sun 12:00	0.5	✗	0.49	0.09	0.51	0.03	0.01	0.01	0.24	0.01	0.16	0.01
		0.5	✓	0.64	0.27	0.62	0.26	0.17	0.01	0.53	0.07	0.39	0.02
		1.0	✗	0.63	0.33	0.63	0.20	0.10	0.02	0.26	0.05	0.08	0.05
		1.0	✓	0.54	0.12	0.55	0.03	0.06	0.02	0.46	0.05	0.13	0.21
		2.0	✗	0.58	0.36	0.55	0.16	0.23	0.00	0.04	0.00	0.00	0.00
		2.0	✓	0.54	0.34	0.57	0.06	0.32	0.00	0.16	0.00	0.06	0.00
	Shade 14:00	0.5	✗	0.39	0.48	0.42	0.46	0.50	0.24	0.33	0.42	0.13	0.29
		0.5	✓	0.49	0.54	0.44	0.55	0.41	0.56	0.35	0.57	0.20	0.41
		1.0	✗	0.31	0.31	0.35	0.41	0.26	0.67	0.29	0.21	0.05	0.02
		1.0	✓	0.36	0.39	0.32	0.39	0.29	0.64	0.28	0.51	0.00	0.00
		2.0	✗	0.22	0.37	0.35	0.48	0.06	0.44	0.04	0.01	0.00	0.00
		2.0	✓	0.27	0.32	0.25	0.32	0.10	0.34	0.08	0.09	0.02	0.01
West	Sun 14:00	0.5	✗	0.12	0.14	0.15	0.15	0.02	0.03	0.21	0.35	0.19	0.22
		0.5	✓	0.23	0.18	0.22	0.22	0.04	0.01	0.28	0.38	0.21	0.30
		1.0	✗	0.19	0.29	0.29	0.35	0.08	0.10	0.21	0.21	0.05	0.04
		1.0	✓	0.25	0.29	0.23	0.34	0.11	0.11	0.39	0.41	0.01	0.03
		2.0	✗	0.30	0.43	0.02	0.43	0.35	0.11	0.09	0.20	0.02	0.05
		2.0	✓	0.34	0.35	0.37	0.39	0.46	0.22	0.30	0.22	0.01	0.18
	Shade 12:00	0.5	✗	0.38	0.16	0.36	0.18	0.16	0.03	0.21	0.22	0.19	0.12
		0.5	✓	0.40	0.26	0.41	0.28	0.12	0.11	0.27	0.25	0.20	0.17
		1.0	✗	0.45	0.16	0.44	0.13	0.16	0.15	0.23	0.13	0.14	0.11
		1.0	✓	0.42	0.26	0.41	0.18	0.21	0.04	0.30	0.19	0.04	0.06
		2.0	✗	0.43	0.27	0.44	0.27	0.18	0.06	0.07	0.30	0.00	0.21
		2.0	✓	0.43	0.17	0.42	0.11	0.21	0.01	0.25	0.12	0.04	0.06

Note: Correlations (r^2) shaded from white (weak) to green (strong)

IR camera

To investigate only the C3 and the measurement sides, an extract from Table 6.1 is presented in Table 6.2.

Table 6.2. Extract from Table 6.1 of the CWSI vs SWP correlations for C3 at 0.5 m

Side	Sunlight	WP	Stage II	Stage III
East	Sun 12:00	✗	0.49	0.09
		✓	0.64	0.27
	Shade 14:00	✗	0.39	0.48
		✓	0.49	0.54
West	Sun 14:00	✗	0.12	0.14
		✓	0.23	0.18
	Shade 12:00	✗	0.38	0.16
		✓	0.40	0.26

Note: Correlations (r^2) shaded from white (weak) to green (strong)

Comparing the Eastern and Western sides of the canopy for the C3 with the best conditions (WP at 0.5 m) only, it is clear that the correlation is better on the Eastern side, irrespective of the measurement time and thus the sun's position. Gutiérrez *et al.* (2021) found that the Eastern side of the canopy provided the best correlations when combining four days measured over two seasons (only using afternoon measurements). The side of the canopy that received sunlight during the morning proved to be the better indicator of plant water stress. The Eastern side is photosynthetically active for a prolonged period of time (the whole morning, compared to the one hour that the Western side receives sunlight before measurements).

It is further noticed that the sunlit side, at 12:00, performed very well in stage II, and very poorly in stage III. The Eastern side, at 14:00, performs consistently in both periods. The change in the canopy's thermal response, discussed in Section 6.3.3, has a larger impact on the sunlit side of the canopies.

The consistency of the results at 14:00 on the shaded side of the canopy makes it attractive as a standard method for CWSI measurement. The results are consistent with literature that indicate that the shaded canopy side should be used for CWSI measurements (Jones, 2002; Pou *et al.*, 2014; Petrie *et al.*, 2019).

The C3 performed well at all three distances, but the correlation is the best at the closest distance, especially when no WP is used. Error is introduced by measuring non-canopy temperatures, such as background, trunk and fruit, when measuring from further distances. The benefit of including a larger sample of the canopy leaves for a representative canopy temperature does not outweigh these background errors. The fact that the shaded side of the canopy is used, reduces

the need to capture a larger sample of the canopy, as the leaves on the shaded side of the canopy are at a similar temperature.

Low-cost sensors

The findings in Section 6.3.4, regarding the canopy side, also apply to the low-cost sensors (presented in Table 6.1). The correlations are good on the sunlit side of the canopy at 12:00 in the first stage, but in the second stage, the correlations on the shaded side, at 14:00, are the best. A summary of the low-cost sensor CWSI to SWP correlation is presented in Table 6.3 for all distances, with and without a WP on the shaded side at 14:00.

Table 6.3. Extract from Table 6.1 of the CWSI vs SWP correlations for the low-cost sensors on the Eastern side of the canopy at 14:00

Distance	WP	IR12		IR35		IR90	
		Stage II	Stage III	Stage II	Stage III	Stage II	Stage III
2.0	✗	0.06	0.44	0.04	0.01	0.00	0.00
2.0	✓	0.10	0.34	0.08	0.09	0.02	0.01
1.0	✗	0.26	0.67	0.29	0.21	0.05	0.02
1.0	✓	0.29	0.64	0.28	0.51	0.00	0.00
0.5	✗	0.50	0.24	0.33	0.42	0.13	0.29
0.5	✓	0.41	0.56	0.35	0.57	0.20	0.41

Note: Correlations (r^2) shaded from white (weak) to green (strong)

It is clear, for the IR90 sensor, that the measurements at 0.5 m are the best, and the findings agree with that of Section 5.3.2. The FOV of the IR90 sensor is simply too large to accurately measure T_c. In stage III, at 0.5 m, the correlations with the WP are significantly better than the results without the WP. Similarly, the IR35 sensor performs best at 0.5 m. In most cases, the results with the WP are better than the results without the WP.

The IR12 sensor also performs the best at the closest distance, which was not expected. When measuring from 2 m with the IR12 sensor, a small change in the angle has a significant effect on the measured area, which could lead to the measurement of background material.

When no WP is used, the IR35 sensor from 0.5 m, or the IR12 sensor, from 1 m performed the best. But as explained, the IR12 results in stage III are better due to fewer measurements. It is therefore recommended, that if no WP is to be used, measurements should be taken from 0.5 m with the IR35 sensor. The results from this section agree with literature which indicates that where single area-sensors

are used to measure T_c, the sensors are placed within 0.5 m of the canopy (Ahi *et al.*, 2015; Shellie and King, 2020; Van Asbroeck, 2018).

6.3.5 Alternative CWSI reference temperature methods

The measurement of CWSI can be simplified by using the automatic reference temperature methods discussed in Chapter 4. A correlation matrix, for the different sensors and automatic reference methods, is presented in Table 6.4. The Filter method from Chapter 5 is presented as a sensor type.

Table 6.4. CWSI and SWP correlations for the different reference temperature methods. Measurements taken at 0.5 m with a WP on the shaded side of the canopy at 14:00.

Reference	Mask		Filter		IR12		IR35		IR90		IR35*	
	Stage II	Stage III	Stage II	Stage III	Stage II	Stage III	Stage II	Stage III	Stage II	Stage III	Stage II	Stage III
NAT	0.49	0.54	0.44	0.55	0.41	0.56	0.35	0.57	0.20	0.41	0.33	0.42
HT	0.30	0.46	0.28	0.43	0.41	0.43	0.29	0.42	0.23	0.40	0.30	0.35
EMP	0.46	0.53	0.42	0.52	0.61	0.53	0.70	0.48	0.60	0.44	0.65	0.38
LEB	0.32	0.51	0.30	0.47	0.49	0.52	0.49	0.62	0.47	0.59	0.46	0.57

Note: NAT, HT, EMP and LEB are the Natural, Heat transfer, Empirical and Leaf energy balance models respectively. Correlations (r^2) shaded from white (weak) to green (strong). *These IR35 measurements are from 0.5 m with no WP.

For the C3, the correlations do not improve by using the other reference methods. This is to be expected, as the methods were optimised to match the Natural method. The EMP method performs the best, with CWSIs in the range of 0.2 to 0.9. The leaf energy balance (LEB) seems to perform better than the heat transfer (HT) method, but it has a very narrow CWSI range of 0.3 to 0.75, which is explained by the under- and overestimation of the reference temperatures discussed in Section 4.4.3. The CWSI range of the HT method is 0.20 to 0.85. By using the automatic filtering method, the correlation for the natural method decreases in stage II, and increases slightly in Stage III. The increase in the correlation is not significant, and is assumed to be a random effect. By using the Empirical (EMP) method along with the automatic filtering method, the correlations only decrease by 0.07 and 0.02 in stage II and III respectively. This semi-automatic method requires a minimal amount of effort from the user, but crucially still requires the use of a WP. Without a WP, the r^2 is 0.39 and 0.43 in stage II and III respectively.

The CWSI calculated with the IR35 and IR90 sensors improves significantly when certain automatic reference temperature methods are used. The HT method,

which provided the most accurate results in Chapter 4, does not improve the correlations. This may be due to the constant offsets observed in the low-cost sensors in Chapter 5. The simple EMP method and LEB methods do improve the results. For the IR35 sensor, the LEB could improve the correlations in stages II and III, while the EMP method could only improve the correlations in stage II. For the IR90 sensor, both the EMP and LEB methods improve the correlations in both stages. The inaccuracy of the reference temperature measurements with these low-cost sensors, as discussed in Section 4.4.4, causes the correlations to improve for the low-cost sensors when using automatic reference temperatures. As with the C3, the correlations decrease significantly when no WP is used.

The IR35 sensor, however, with no WP has good correlations when using the EMP and LEB methods. In stage II the LEB correlations for this sensor are slightly worse than the C3 with the natural method, but they are slightly better in stage III. When using the EMP method, the correlations are better than the C3 in stage II and worse in stage III. The EMP approach is more attractive as a low-cost sensor, as with an automatic method that only requires ambient temperature and humidity data, it can accurately determine CWSI. The LEB method has the drawback of requiring a net radiometer in addition to the temperature, humidity and wind speed from the commercial weather station.

The HT method, which performed the best in Chapter 4, was outperformed by the EMP method in every case presented in Table 6.4. The LEB method that did not perform well in Chapter 4 gave good results when used with the low-cost sensors to calculate the CWSI. The EMP method performed the best and it is recommended that it should be used in conjunction with the low-cost sensors. Results from chapter 4 indicate that the EMP method perform the best in low-wind conditions.

Sepúlveda-Reyes *et al.* (2016) compared the correlation of CWSI to SWP and found that by using the Natural method for CWSI reference temperatures, the correlations are slightly better ($r^2 = 0.36$ vs $r^2 = 0.33$) than when using LEB equations. These results agree with that of the C3, but not with that of the low-cost sensors.

6.3.6 CWSI equation sensitivity

Accurate T_c measurements alone do not ensure accurate CWSI values. This was evident with the low-cost IR sensor which had canopy temperatures similar to the C3, but could not accurately determine the CWSI due to inaccurate reference temperature measurements.

Figure 6.6 presents the CWSI error vs measurement errors of the three input temperatures. CWSI is very sensitive to the overestimation of T_{wet} and the underestimation of T_{dry} but responds linearly to erroneous T_c measurements. The CWSI equation is sensitive when the reference temperatures are close to the canopy temperatures, and a large $T_{dry} - T_{wet}$ range ensures that the CWSI is in the 0 to 1 range. The LEB reference temperature method, which consistently over-

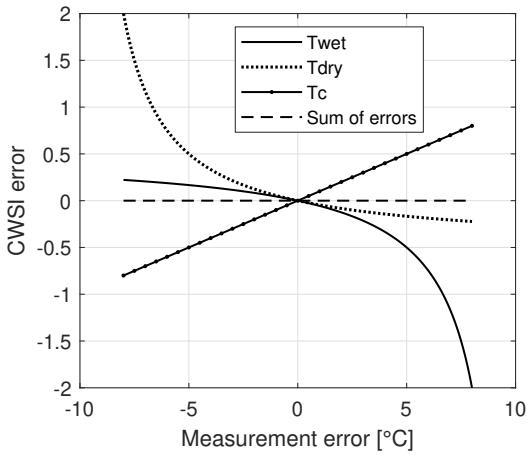

Figure 6.6. CWSI error vs measurement error for T_{wet}, T_{dry} and T_{c}. Plotted from nominal values of $T'_{\text{c}} = 30\,°\text{C}$, $T'_{\text{wet}} = 25\,°\text{C}$ and $T'_{\text{dry}} = 35\,°\text{C}$ about the origin with no measurement error.

estimates and underestimates T_{dry} and T_{wet} respectively, is very robust against these errors.

If all measurements are taken with the same instrument that has a systematic error, the errors will cancel out when calculating CWSI (Poirier-Pocovi *et al.*, 2020). This eliminates the need for calibration, but not when automatic reference temperature methods are used.

Besides the equation, the environmental conditions further complicate the CWSI accuracy. Wind speed negatively affects CWSI accuracy as rapid changes in the leaves' stomatal conductance influences the transpiration and in turn the leaf temperature (Jones, 1999). Furthermore, low VPD as a result of low ambient temperature and high relative humidity, influences the accuracy of CWSI (Jones, 1999). The effect of the solar radiation could not be verified as only clear cloudless days were selected for tests, but this is well established in literature (Fuchs, 1990; King and Shellie, 2016; Jones, 1999).

6.4 Conclusion

In this chapter, the ability of different IR sensors and techniques to measure plant water stress was investigated. It was found and verified in literature that grapevines have different thermal responses in their different major physiological stages. Independent correlations for these stages were evaluated and measurement techniques that perform consistently well in both measurement periods were identified. The shaded, Eastern side of the canopy, after midday, was identified as the best period to measure T_{c}. This was confirmed by all the sensors and agrees well with literature. The shaded side of the canopy, still photosynthetically active from the morning sun, provides the best measurement conditions for the CWSI.

The thermal camera could be used to determine CWSI most accurately when using the Natural method for CWSI reference temperatures. It was also evident that the use of a WP background increases the accuracy of the CWSI measurements. A thermal thresholding technique (Filter) can be used to automatically calculate representative canopy temperatures from the thermal images, along with the EMP method for CWSI reference temperatures.

The low-cost sensors could accurately predict the plant water stress level only when alternative methods of determining CWSI reference temperatures were used. The simple EMP method provided the best reference temperatures for these low-cost sensors.

The general aim of this study is accomplished: Methods of obtaining CWSI canopy temperatures and reference temperatures measurements have been improved. Low-cost sensors can be used to accurately determine grapevine CWSI.

Chapter 7

Conclusions and recommendations

7.1 Overview

This study aimed to determine whether low-cost IR sensors could be used to accurately determine grapevine crop water stress index (CWSI). In order to investigate this, CWSI reference and canopy temperature measurements methods were evaluated and new methods were developed. It was found that, when using automatic reference temperatures, the low-cost sensors could be used to accurately determine grapevine CWSI.

7.2 Conclusions and recommendations according to aims and objectives

Objective 1: Improve CWSI reference temperature measurement

(*a*) *Select a baseline reference temperature measurement protocol.*

The method proposed by Jones (1999), which used a Vaseline-covered leaf for T_{dry} and a water-covered leaf for T_{wet}, is a standard method of measuring CWSI reference temperatures. Different measurement protocols of this method are, however, used in literature. By comparing different measurement protocols, it was found that a sunlit T_{dry} leaf, attached to the canopy, serves as a reliable upper reference temperature. Furthermore, the attached T_{wet} leaf, in the canopy shade, serves as a reliable lower reference temperature.

(*b*) *Compare and select automatic reference temperature methods.*

Two new automatic reference temperature methods were proposed and developed. The heat transfer (HT) model uses fundamental heat transfer

formulations to calculate T_{wet} and T_{dry}. The model accounts for radiative, convective and evaporative heat transfer, and the relevant equations are presented. The Empirical (EMP) method, on the other hand, uses empirical correlations to estimate the reference temperatures based only on ambient temperature and humidity.

Five unknown parameters of the HT method and two parameters of the EMP method were determined by using Particle Swarm optimisation. These parameters were established by optimising the methods' output to ground truth measurements taken with an IR camera in a commercial vineyard. These ground truth measurements were based on the standard technique from literature. In addition to these two new methods, the well-established leaf energy balance (LEB) was used to calculate the reference temperatures. By comparing the models' output to the physical measurements, it was found that the HT method performed the best. It was able to calculate T_{wet} and T_{dry} to within 0.5 K and 1 K respectively. It was shown that the model responds to meteorological conditions as expected. The EMP method performed well for its simplicity. It provided accurate results, but proved unstable in windy conditions. Reference temperatures calculated with the leaf energy balance (LEB) method were significantly higher and lower than the physical T_{dry} and T_{wet} measurements respectively. The LEB equations were not developed for the situation in this study, but the method still proved useful for the low-cost sensors, as was found in the later chapters.

The HT method can be refined by measuring wind speed at leaf level and further developing the convective and evaporative heat transfer relations for the different airflow conditions. Investigation into the radiative properties of the reference surfaces may lead to improved results.

(*c*) *Compare measurements of the low-cost sensors to those of an IR camera.*

The low-cost sensor measurements of the CWSI reference leaf temperature were found to be unreliable. The errors were investigated, and the induced error from casting a shadow on the measurement surface was shown to be an error source. The results emphasise the need for automatic reference surface temperature measurements.

Objective 2: Investigate hardware and physical requirements of canopy temperature measurements

(*a*) *Calibrate the sensors that will be compared in the study.*

A water bath calibration method was used to ensure that all the sensors measure the same temperatures in the expected vineyard temperature range. It was determined that the Flir One would not be appropriate for use in this study.

(*b*) *Investigate automatic analysis techniques of thermal images.*

Automatic methods of thermal image analysis were investigated to eliminate user input in manually selecting canopy material from the normal camera images. A histogram analysis (which picks the most frequent temperature in the matrix), and a filtering method (which uses the measured T_{wet} and T_{dry} to eliminate background pixels), were investigated. It was found that the filtering method performs better than the histogram analysis.

(*c*) *Compare low-cost sensor canopy measurements to commercial IR camera measurements.*

Constant offsets between the low-cost sensors and the C3 were identified when measuring the canopy temperature. The difference in spectral ranges of these sensors was identified as a major cause of these offsets. A further source of error is the different methods of compensating for the reflected IR radiation that the sensors use. The low-cost IR array temperature sensor was found to be inaccurate in measuring the canopy temperature. The histogram and filtering method did not improve the IR array sensor's performance.

Thermal cameras with higher accuracy and resolution will improve background temperature avoidance, while improving the measured canopy temperature. Similar sensor spectral ranges should be used when comparing the temperatures of sunlit plant canopies. While the use of a WP background does improve the results, more practical methods of avoiding background temperatures with the low-cost sensors must be investigated.

Objective 3: Determine the best conditions for CWSI measurements

(*a*) *Determine the best measurement parameters for accurate CWSI measurement.*

The best measurement parameters were identified by correlating CWSI to stem water potential (SWP). The phenological progression of the grapevines necessitated the need for different correlations in their different phenological stages. The plants' thermal response in the latter stages of the season was much lower than in the initial stages of the season, even though the SWP range was larger.

It was found that measurements taken on the shaded (Eastern) side of the canopies, at 14:00, provided the most consistent correlations between CWSI and SWP. This side of the canopies was photosynthetically active the entire morning, resulting in a good thermal response to the plants' water status. In addition, the lower variability of the unshaded leaves provides more consistent canopy temperatures. For the C3, the best measurement distance was found to be 0.5 m, using a WP background. These conditions

provide canopy temperature measurements which, when used for CWSI, correlate well to SWP.

This measurement time and distance were also found to work the best for the low-cost sensors. All the low-cost sensors performed well at 0.5 m with a WP, while the IR35 sensor also performed well with no WP at 0.5 m.

Good conditions for canopy temperature measurements for CWSI calculation were found, but further refinement can improve the results. It is established that the shaded canopy temperatures, about an hour after solar noon work well, but different times in this period can be investigated. Images taken automatically every few minutes for a few hours after solar noon can be used to establish the ideal measurement time. Another measurement aspect that can be investigated is the measurement angle. At angles other than directly normal to the canopy, less gaps in the canopy may be visible, which could improve the results and avoid the use of a WP.

(*b*) *Investigate whether the low-cost sensors can be used along with automatic reference temperature methods to determine CWSI.*

When using the different automatic reference methods, the C3's results were not found to improve. The low-cost sensors' CWSI had better correlations to SWP when the automatic reference temperatures were used. This is as the low-cost sensors cannot accurately measure the CWSI reference temperatures. It is concluded that a low-cost sensor, used in conjunction with a simple reference temperature calculation, can be used to accurately measure CWSI without the need for a WP background. This finding provides a low-cost and low-effort method of measuring plant water stress and accomplishes the general aim of the study.

7.3 Final Remarks

This study provides valuable groundwork in the improvement of grapevine water stress measurement with infrared sensors. The results from this study are insightful, but have led to more research questions. Continued research and development will ensure that canopy temperature measurement for water stress detection becomes common practice among researchers and viticulturists. Verification across more grapevine cultivars will further improve the results.

Low-cost single-area sensors, used along with weather station data, can be used to accurately determine grapevine CWSI.

Appendices

Appendix A

Infrared energy

A.1 Basic principles

A.1.1 Electromagnetic and thermal radiation

Electromagnetic radiation that applies to heat transfer is the thermal radiation emitted as energy transitions within atoms, molecules and electrons of matter (Cengal and Ghajar, 2015). The infrared (IR) region of the electromagnetic spectrum ranges from 0.75 µm to 100 µm. Radiation is a volumetric phenomenon being emitted, transmitted and absorbed throughout the volume of matter. For non-transparent (opaque) materials, however, radiation is a surface phenomenon, as the radiation emitted by the inner regions cannot reach the surface of the material (Cengal and Ghajar, 2015). By applying a thin coating to a material, the radiation characteristics of material can be altered completely.

A theoretical material, known as a blackbody is a perfect emitter and absorber of radiation, independent of wavelength (grey surface) and direction (diffuse surface). In 1879 Joseph Stefan expressed the radiation energy emitted by a blackbody as

$$E_b(T) = \sigma T^4 \tag{A.1}$$

where σ is the Stefan-Boltzmann constant (5.670×10^{-8}) and T is the absolute surface temperature in Kelvin. E_b is the blackbody emissive power, which is the sum of radiation emitted over all wavelengths.

A.1.2 Surface radiative properties

At a given temperature, a blackbody emits the maximum possible radiation and is used as a reference for describing the radiative properties of a material (Cengal and Ghajar, 2015). Emissivity (ϵ) of a material is defined as the ratio of radiation emitted by a surface to the radiation emitted by a blackbody at the same temperature. ϵ varies with temperature, wavelength and direction of emittance. The total hemispherical emissivity is the ratio of radiation emitted over all wavelengths

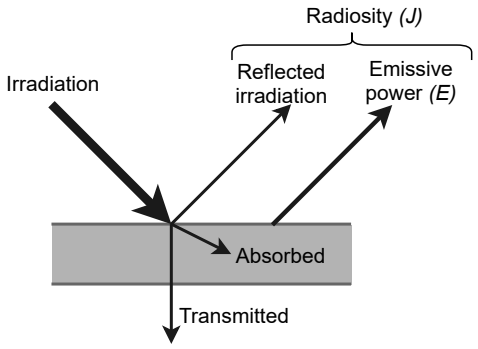

Figure A.1. Sum of components of IR radiation.

and directions, to the blackbody emissive power

$$\epsilon(T) = \frac{E(T)}{E_{\text{blackbody}}(T)} \tag{A.2}$$

For practical applications, grey and diffuse approximations are used in radiation calculations (Cengal and Ghajar, 2015). A material's emissivity is taken as its total hemispherical emissivity.

Radiation incident on a body (known as irradiation, G) can either be absorbed, transmitted , or reflected by the surface. The fraction of the absorbed, transmitted and reflected irradiation is known as a surface absorptivity (α), transmissivity (τ) and reflectivity (ρ), respectively. The sum of the components must be equal to 1, and these are presented in Figure A.1. These irradiation properties are total hemispherical properties, as α, τ and ρ are average properties for a surface over all directions and wavelengths.

A.1.3 Kirchoff's law

Given a small body with emissivity ϵ, surface area A_s and absorptivity α at temperature T, surrounded by an enclosure at the same temperature; the interior of the enclosure approximates a blackbody as radiation is reflected multiple times inside the cavity and is given many opportunities to be absorbed by the surface. This blackbody approximation is valid regardless of the surfaces' radiative proprieties and the small body in the enclosure is too small to alter the blackbody nature of the enclosure. The irradiation on any surface of the body is equal to the radiation emitted by a blackbody at the same temperature.

$$G = E_b(T) = \sigma T^4 \tag{A.3}$$

The portion of the irradiation that is absorbed is

$$G_{\text{abs}} = \alpha G = \alpha \sigma T^4 \tag{A.4}$$

and radiation emitted by the body is

$$E_{\text{emit}} = \epsilon\sigma T^4 \tag{A.5}$$

Since the body is in equilibrium with its surroundings, the incoming radiation is equal to the outgoing radiation

$$A_s\epsilon\sigma T^4 = A_s\alpha\sigma T^4 \tag{A.6}$$

and it is concluded that

$$\epsilon(T) = \alpha(T) \tag{A.7}$$

The total hemispherical emissivity of a surface is equal to its total hemispherical absorptivity coming from blackbody at the same temperature. This is an approximation based on the assumption that the surface temperature is the same temperature as the irradiation source and is only valid for temperature differences less than a few hundred degrees (Cengal and Ghajar, 2015).

A.2 Temperature calculation from infrared radiation measurement

Every blackbody surface emits radiation in proportion to its temperature. As surfaces are not ideal blackbodies, only a fraction (ϵ) of the energy is emitted.

Radiation E_{obj} is emitted by the object and is attenuated by its emissivity ϵ_{obj}. The atmosphere, with a transmissivity of τ_{atm}, further attenuates the radiation between the object and the sensor. The radiation emitted by the object that is observed by the sensor is

$$\varphi_{\text{obj}} = E_{\text{obj}}\epsilon_{\text{obj}}\tau_{\text{atm}} \tag{A.8}$$

where φ is the radiative heat flux. τ_{atm} is the transmissivity of the atmosphere between the object and the sensor.

The surroundings emit radiation which reflects off the object's surface. As the transmissivity of the opaque object is zero, the object's reflectivity $\rho = 1-\epsilon_{\text{obj}}$. The radiation heat flux emitted from the surroundings, reflected off the surface and passing through the air is

$$\varphi_{\text{surr}} = E_{\text{surr}}(1-\epsilon_{\text{obj}})\tau_{\text{atm}} \tag{A.9}$$

The atmosphere between the object and sensor has a transmissivity τ_{atm}, which depends on the ambient temperature and humidity. As no radiation is reflected off the atmosphere $\epsilon_{\text{atm}} = 1-\tau_{\text{atm}}$. The radiation heat flux emitted from the atmosphere is

$$\varphi_{\text{atm}} = E_{\text{atm}}(1-\tau_{\text{atm}}) \tag{A.10}$$

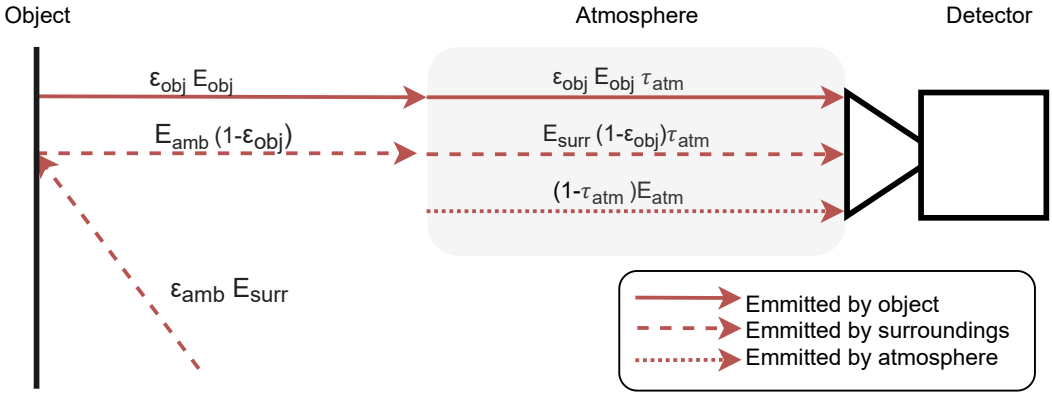

Figure A.2. Components of IR signal measured by the detector

The transmissivity of the air is a function of air temperature, relative humidity and measurement distance (Minkina and Dudzik, 2006). IR sensor manufacturers use proprietary empirical functions to calculate τ_{atm} (Minkina and Dudzik, 2009). An approximation is used in this study.

The total signal (S) observed by the sensor is dependent on components of the radiation emitted by the object, surroundings and the air between the object and the sensor, as shown in Figure A.2

$$S = C(\varphi_{\text{obj}} + \varphi_{\text{surr}} + \varphi_{\text{atm}}) \tag{A.11}$$

where C is some parameter depending on the specific detector, optical components and atmospheric properties (Minkina and Dudzik, 2009). Following the principles of equations A.8 through A.11, the total detector signal is derived as (Minkina and Dudzik, 2006):

$$S_{\text{tot}} = S_{\text{obj}}\epsilon_{\text{obj}}\tau_{\text{atm}} + S_{\text{surr}}(1-\epsilon_{\text{obj}})\tau_{\text{atm}} + S_{\text{atm}}(1-\tau_{\text{atm}}) \tag{A.12}$$

S_{obj}, S_{surr} and S_{atm} are detector signals proportionate to black body radiation intensity of the respective fluxes. The sensor detector can only detect the sum of these signals and cannot differentiate between the sources of these signals.

The components the signal emitted by the atmosphere and surroundings must be compensated for. Rearrange A.12 to find S_{obj}, the signal of the object at temperature T_{obj}.

$$S_{\text{obj}} = \frac{S_{\text{tot}}}{\epsilon_{\text{obj}}\tau_{\text{atm}}} - (S_{\text{surr}}\frac{1-\epsilon_{\text{obj}}}{\epsilon_{\text{obj}}} + S_{\text{atm}}\frac{1-\tau_{\text{atm}}}{\epsilon_{\text{obj}}\tau_{\text{atm}}}) \tag{A.13}$$

To calculate S_{obj}, the exitance of the air and surroundings are required, to remove their components in the sum of S_{obj}.

Software converts a signal to a temperature by

$$T_{\text{i}} = \frac{B_2}{\ln(\frac{B_1}{S_{\text{i}}} + B_3)} \tag{A.14}$$

B_1, B_2 and B_3 are sensor calibration constants (Minkina and Dudzik, 2009). Rewrite A.14 in terms of S, the calibrated IR signal measured by the sensor, in terms of the temperature causing the signal.

$$S_{\mathrm{i}} = \frac{B_1}{\exp \frac{B_2}{T_{\mathrm{i}}} - B_3} \tag{A.15}$$

S_{surr} and S_{atm} can be calculated with A.15 by estimating its respective temperatures. Substitute S_{surr} and S_{atm} into equation A.13

$$S_{\mathrm{obj}} = \frac{S}{\epsilon_{\mathrm{obj}} \tau_{\mathrm{atm}}} - \left(\frac{B_1}{\exp \frac{B_2}{T_{\mathrm{surr}}} - B_3} \cdot \frac{1-\epsilon_{\mathrm{obj}}}{\epsilon_{\mathrm{obj}}} + \frac{B_1}{\exp \frac{B_2}{T_{\mathrm{atm}}} - B_3} \cdot \frac{1-\tau_{\mathrm{atm}}}{\epsilon_{\mathrm{obj}} \tau_{\mathrm{atm}}}\right) \tag{A.16}$$

Substitute equation A.14 into equationA.16 and finally calculate the object temperature as

$$T_{\mathrm{obj}} = \frac{B_2}{\ln\left(\frac{B_1}{S_{obj}} + B_3\right)} \tag{A.17}$$

The process described here takes the emissivity of the target surface into account. Commercial thermal cameras use the process mentioned here to give an accurate temperature measurement of a target surface.

A.3 Simple emissivity correction for low-cost sensors

Low-cost sensors often do not take the radiation reflected off the surface and the radiation emitted by the atmosphere into account when reporting a temperature measurement. They assumes that all the radiation received by the sensor is from the target surface (assuming a blackbody).

If the radiation emitted by the atmosphere is ignored, which is a reasonable assumption at short distances, then the IR radiation received by the sensor is only the sum of the radiation emitted by and reflected off the surface:

$$E_{\mathrm{recieved}} = \epsilon E_{\mathrm{obj}} + (1-\epsilon) E_{\mathrm{surr}} \tag{A.18}$$

Eqn A.1 is substituted into equation A.18 to calculate the emissivity corrected temperature (Apogee Instruments (2021)):

$$S = \sqrt[4]{\frac{T_{\mathrm{sensor}}^4 - (1-\epsilon) T_{\mathrm{reflected}}^4}{\epsilon}} \tag{A.19}$$

The reflected temperature can be approximated as the ambient temperature (Minkina and Dudzik, 2009).

Appendix B

Climatic and thermodynamic properties

B.1 Atmospheric pressure

Atmospheric pressure, P_{atm}, can be estimated using the ideal gas law

$$P_{\text{atm}} = 101300\left(\frac{293 - 0.0065z}{293}\right)^{5.26} \tag{B.1}$$

from equation (7) in Allen *et al.* (1998), where z is altitude in m and assuming an atmospheric temperature of 20 °C.

B.2 Latent heat of vaporization

λ, the latent heat of vaporization of water is the amount of energy required to change the temperature of 1 kg of water by 1 K. λ only varies slightly over ambient temperate ranges and a value of 2.45 MJ/kg is adequate for air temperature of around 20 °C (Allen *et al.*, 1998).

B.3 Psychometric constant

The Psychometric constant γ, correlates the partial pressure of water vapour to the air temperature:

$$\gamma = \frac{c_{\text{p}} P_{\text{atm}}}{0.622\lambda} = 0.665 \times 10^{-3} P_{\text{atm}} \tag{B.2}$$

where c_p is the specific heat of air at constant pressure, and0.622 is the ratio of the molecular weight of water vapour to that of air. γ is mainly dependent on air pressure and can be assumed constant at a particular location (Allen *et al.*, 1998). More accurate values can be obtained by evaluating c_{p} at the specific air temperature.

B.4 Saturation vapour pressure

Water vapour pressure contributes to the total atmospheric pressure. The partial pressure of the water vapour (P_{H_2O}) is directly related to the amount of water in the air. The maximum amount of water vapour in air is called the saturated vapour pressure ($P^*_{H_2O}$) and is dependent on the air temperature. At higher temperatures, air has a larger capacity for water vapour and the relationship is exponential.

$P^*_{H_2O}$ is related to air temperature and can be calculated, according to Allen *et al.* (1998) as

$$P_{H2O,sat} = 0.6108 \exp\left(\frac{17.27 T'_a}{T'_a + 237.3}\right) \tag{B.3}$$

where the ambient temperature T'_a is in °C.

B.5 Slope of the saturation vapour pressure curve

The slope of the saturation vapour pressure curve (Δ), measured in (kPa/°C) is used in evapotranspiration equations and increases with temperature. Δ can be approximated as

$$\Delta = \frac{4098[0.6108 \exp(\frac{17.27 T_a}{T_a + 237.3})]}{(T_a + 237.3)^2} \tag{B.4}$$

using the ambient temperature (Allen *et al.*, 1998).

B.6 Vapour pressure deficit

Vapour pressure deficit, also known as vapour pressure depression, is the difference between the partial vapour pressure of saturated atmospheric air (at a certain dry-bulb temperature) and the vapour pressure of unsaturated air at the same dry-bulb temperature.

$$\delta_e = P^*_{H_2O} - P_{H_2O} \tag{B.5}$$

B.7 Relative humidity

Relative humidity is the fraction of water vapour in the air compared to the maximum water vapour that can be carried by the air at a specific temperature. As water vapour is directly related to partial pressure, the relative humidity can be expressed as

$$\phi = \frac{P_{H_2O}}{P^*_{H_2O}} \tag{B.6}$$

As the temperature changes throughout the day, relative humidity will change, even though the vapour pressure might remain relatively constant.

B.8 Net radiation

The net radiation (R_{net}) is the difference between the absorbed incoming solar radiation and the emitted radiation from a leaf surface and is dependent on the leaf surface temperature T_l (Jones, 2014).

$$R_{net} = R_{absorbed} - \epsilon\sigma(T_l)^4 \tag{B.7}$$

R_{ni}, the isothermal net radiation, is defined as radiation absorbed by an identical surface at the ambient temperature T_a.

$$R_{ni} = R_{absorbed} - \epsilon\sigma(T_a)^4 \tag{B.8}$$

Combining equations B.7 and B.8 and defining $T_l = T_a + \Delta T$ gives

$$R_{ni} = R_n + \epsilon\sigma(T_a^4 + 4T_a^3(\Delta T) + 6T_a^2(\Delta T)^2 + 4T_a(\Delta T)^3 + (\Delta T)^4 - T_a^4). \tag{B.9}$$

As $\Delta T << T_a$, all terms with ΔT^2 or higher can be neglected. This results in

$$R_{ni} \simeq R_{net} + 4\epsilon\sigma T_a^3 \Delta T. \tag{B.10}$$

The second term in equation B.10 is long wave radiative heat loss and is put in a form that is similar to equations used for conductive and convective heat transfer:

$$4\epsilon\sigma T_a^3 \Delta T = (\frac{4\epsilon\sigma T_a^3}{\rho c_p})\rho c_p(T_s - T_a) \tag{B.11}$$

The ρc_p term cancels out. Conductance to radiative heat transfer (g_r) is defined as

$$g_r = \frac{4\epsilon\sigma T_a^3}{\rho c_p}) \tag{B.12}$$

The combination of equations B.10 and B.12 gives

$$R_{net} \simeq R_{ni} - g_r\rho c_p(T_s - T_a). \tag{B.13}$$

Appendix C

Measurement rig

A graphical user interface developed for the touch screen display is presented in Figure C.1. It was developed with the Nextion Editor software. It allows the user to specify measurement parameters that is later used to divide the data for analysis.

A wiring schematic for the measurement rig and its sensors is presented in Figure C.2.

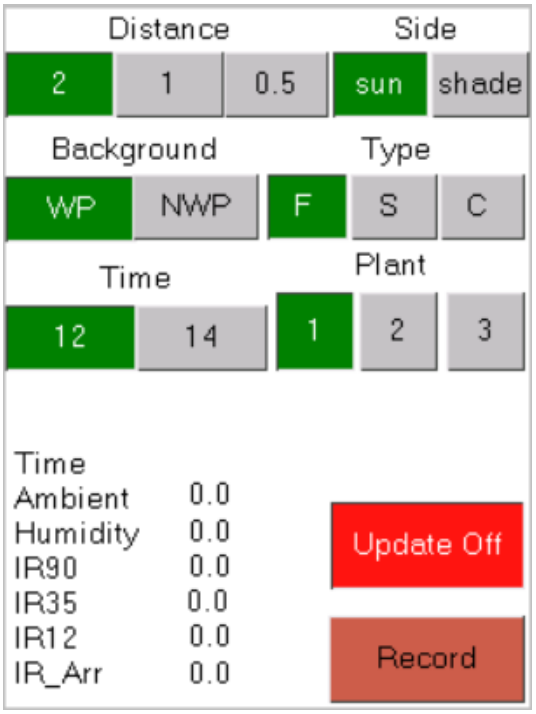

Figure C.1. Measurement rig touch screen graphical user interface

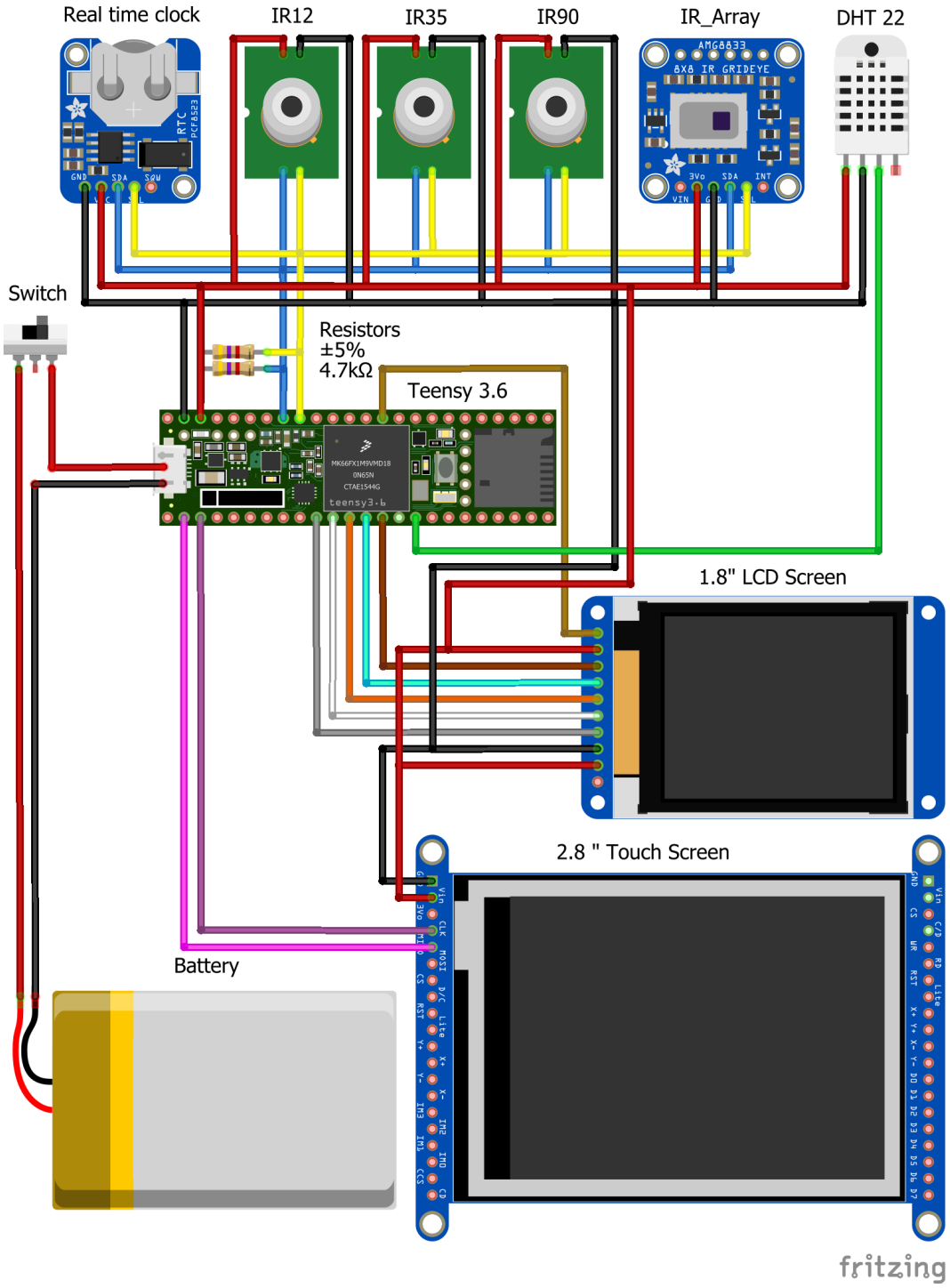

Figure C.2. Measurement rig schematic

List of References

Ahi, Y., Orta, H., Gündüz, A. and Gültaş, H.T. (2015). The canopy temperature response to vapor pressure deficit of grapevine cv. semillon and razaki. *Agriculture and Agricultural Science Procedia*, vol. 4, pp. 399–407. (Cited on page 76)

Alchanatis, V., Cohen, Y., Cohen, S., Moller, M., Sprinstin, M., Meron, M., Tsipris, J., Saranga, Y. and Sela, E. (2009). Evaluation of different approaches for estimating and mapping crop water status in cotton with thermal imaging. *Precision Agriculture*, vol. 11, no. 1, pp. 27–41. (Cited on page 10)

Alghory, A. and Yazar, A. (2018). Evaluation of crop water stress index and leaf water potential for deficit irrigation management of sprinkler-irrigated wheat. *Irrigation Science*, vol. 37, no. 1, pp. 61–77. (Cited on page 10)

Allen, R.G., Pereira, L.S., Raes, D. and Smith, M. (1998). Crop evapotranspiration - guidelines for computing crop water requirements. (Cited on pages 90 and 91)

Améglio, T., Archer, P., Cohen, M., Valancogne, C., Daudet, F.-A., Dayau, S. and Cruiziat, P. (2021). Significance and limits in the use of predawn leaf water potential for tree irrigation. *Plant and Soil*, vol. 207, pp. 155–167. (Cited on page 16)

Apogee Instruments (2021). Emissivity correction for infrared radiometer sensors. [2021, June 1].
Available at: https://www.apogeeinstruments.com/emissivity-correction-for-infrared-radiometer-sensors/ (Cited on page 89)

Bellvert, J., Marsal, J., Girona, J. and Zarco-Tejada, P.J. (2014). Seasonal evolution of crop water stress index in grapevine varieties determined with high-resolution remote sensing thermal imagery. *Irrigation Science*, vol. 33, no. 2, pp. 81–93. (Cited on pages 10, 17, 18, and 72)

Bower, S.M., Kou, J. and Saylor, J.R. (2009). A method for the temperature calibration of an infrared camera using water as a radiative source. *Review of Scientific Instruments*, vol. 80, no. 9, p. 095107. (Cited on pages 7, 8, and 27)

Brunt, D. (1940). Radiation in the atmosphere. *Quarterly Journal of the Royal Meteorological Society*, vol. 66, pp. 34–40. (Cited on page 37)

Camacho-Alonso, G., Baeza, P., Mendoza, G., Hueso, A. and Tarquis, A.M. (2017). Usefulness and limits of the crop water stress index obtained from leaf temperature for vine water status monitoring. In: *XIIIth International Terrior Congress*. (Cited on page 21)

Campbell, G.S. and Norman, J.M. (1998). *An Introduction to Environmental Biophysics*. Springer New York. (Cited on page 19)

Carey, V.A. (2005). The use of viticultural terroir units for demarcation of geographical indications for wine production in stellenbosch and surrounds. Unpublished masters thesis. Stellenbosch: Stellenbosch University [Online].
Available at: http://refhub.elsevier.com/S0378-3774(20)32240-X/sbref19
(Cited on page 33)

Carrasco-Benavides, M., Antunez-Quilobrán, J., Baffico-Hernández, A., Ávila-Sánchez, C., Ortega-Farías, S., Espinoza, S., Gajardo, J., Mora, M. and Fuentes, S. (2020). Performance assessment of thermal infrared cameras of different resolutions to estimate tree water status from two cherry cultivars: An alternative to midday stem water potential and stomatal conductance. *Sensors*, vol. 20, no. 12, p. 3596. (Cited on pages 7, 18, 19, and 68)

Cengal, Y.A. and Ghajar, A.J. (2015). *Heat and mass transfer*. 5th edn. McGraw Hill. (Cited on pages 37, 38, 39, 40, 42, 47, 85, 86, and 87)

Cetas, T.C. (1978). Practical thermometry with a thermographic camera—calibration, transmittance, and emittance measurements. *Review of Scientific Instruments*, vol. 49, no. 2, pp. 245–254. (Cited on page 7)

Chaerle, L. and Van Der Straeten, D. (2001). Seeing is believing: imaging techniques to monitor plant health. *Biochimica et Biophysica Acta (BBA) - Gene Structure and Expression*, vol. 1519, no. 3, pp. 153–166. (Cited on page 9)

Chandel, A.K., Khot, L.R. and Yu, L.-X. (2021 mar). Alfalfa (medicago sativa l.) crop vigor and yield characterization using high-resolution aerial multispectral and thermal infrared imaging technique. vol. 182, p. 105999. (Cited on page 5)

Chaves, M.M., Santos, T.P., Souza, C.R., Ortuno, M.F., Rodrigues, M.L., Lopes, C.M., Maroco, J.P. and Pereira, J.S. (2007). Deficit irrigation in grapevine improves water-use efficiency while controlling vigour and production quality. *Annals of Applied Biology*, vol. 150, no. 2, pp. 237–252. (Cited on page 1)

Chaves, M.M., Zarrouk, O., Francisco, R., Costa, J.M., Santos, T., Regalado, A.P., Rodrigues, M.L. and Lopes, C.M. (2010). Grapevine under deficit irrigation: hints from physiological and molecular data. *Annals of Botany*, vol. 105, no. 5, pp. 661–676. (Cited on page 1)

Choné, X., Van Leeuwen, C., Dubourdieu, D. and Gaudillère, J.P. (2001 04). Stem Water Potential is a Sensitive Indicator of Grapevine Water Status. *Annals of Botany*, vol. 87, no. 4, pp. 477–483. (Cited on pages 1, 16, 17, and 68)

Cohen, Y., Alchanatis, V., Meron, M., Saranga, Y. and Tsipris, J. (2005 may). Estimation of leaf water potential by thermal imagery and spatial analysis. *Journal of Experimental Botany*, vol. 56, no. 417, pp. 1843–1852. (Cited on page 10)

Coombe, B.G. (1995). Adoption of a system for identifying grapevine growth stages. *Australian Journal of Grape and Wine Research*, vol. 1, no. 2, pp. 104–110. (Cited on page 9)

Costa, J.M., Grant, O.M. and Chaves, M.M. (2013). Thermography to explore plant–environment interactions. *Journal of Experimental Botany*, vol. 64, no. 13, pp. 3937–3949. (Cited on pages 54 and 68)

Drechsler, K., Kisekka, I. and Upadhyaya, S. (2019). A comprehensive stress indicator for evaluating plant water status in almond trees. *Agricultural Water Management*, vol. 216, pp. 214–223. (Cited on page 7)

Eichhorn, K.W. and Lorenz, D.H. (1977). Phenological development stages of the grape vine. *Nachrichtenblatt des Deutschen Pflanzenschutzdienstes*, vol. 29, no. 8, pp. 119–120. (Cited on page 9)

Fernandes de Oliveira, A., Mameli, M.G., Lo Cascio, M., Sirca, C. and Satta, D. (2021). An index for user-friendly proximal detection of water requirements to optimized irrigation management in vineyards. *Agronomy*, vol. 11, no. 2, p. 323. (Cited on pages 9, 18, 32, 70, and 71)

Figliola, R. (1995 jan). *Theory and Design for Mechanical Measurements*. 3, second edition edn. John Wiley and Sons New York. (Cited on page 30)

Flir (2016). *FLIR C3*. [2020, August 10]. Available at: https://flir.netx.net/file/asset/3946/original/attachment (Cited on page 24)

Flir (2018). *FLIR ONE Pro-Series*. [2020, August 10]. Available at: https://www.flir.com/globalassets/imported-assets/document/flir-one-pro-series-datasheet.pdf (Cited on page 24)

FOA (2017). FAOSTATS. Food and Agriculture Organization of the United Nations, Rome, Italy. (Cited on page 1)

Fraga, H., García de Cortázar Atauri, I. and Santos, J.A. (2018). Viticultural irrigation demands under climate change scenarios in portugal. *Agricultural Water Management*, vol. 196, pp. 66–74. (Cited on page 1)

Fuchs, M. (1990). Infrared measurement of canopy temperature and detection of plant water stress. *Theoretical and Applied Climatology*, vol. 42, no. 4, pp. 253–261. (Cited on pages 9, 55, and 78)

Fuentes, S., Bei, R.D., Pech, J. and Tyerman, S. (2012). Computational water stress indices obtained from thermal image analysis of grapevine canopies. *Irrigation Science*, vol. 30, no. 6, pp. 523–536. (Cited on pages 32 and 34)

Gaing, Z.-L. (2003). Particle swarm optimization to solving the economic dispatch considering the generator constraints. *IEEE Transactions on Power Systems*, vol. 18, no. 3, pp. 1187–1195. (Cited on page 41)

Garcia-Tejero, I.F., Costa, J.M., Egipto, R., Duan-Zuazo, V.H., Lima, R.S.N., Lopes, C.M. and Chaves, M.M. (2016). Thermal data to monitor crop-water status in irrigated mediterranean viticulture. *Agricultural Water Management*, vol. 176, pp. 80–90. (Cited on pages 32, 67, and 69)

Giuliani, R.G. and Flore, J.A. (2000). Potential use of infra-red thermometry for the detection of water stress in apple trees. *Acta Horticulturae*, , no. 537, pp. 383–392. (Cited on pages 19 and 56)

Glenn, J.T. (2017). Thermimage: Thermal image analysis. R package [2020, March 20]. Available at: `https://cran.r-project.org/package=Thermimage` (Cited on page 24)

Gonzalez-Dugo, V., Testi, L., Villalobos, F.J., López-Bernal, A., Orgaz, F., Zarco-Tejada, P.J. and Fereres, E. (2020 oct). Empirical validation of the relationship between the crop water stress index and relative transpiration in almond trees. *Agricultural and Forest Meteorology*, vol. 292-293, p. 108128. (Cited on page 5)

Google Earth (2021). Thelema wine farm, south africa -33°54'11.8"s - 18°55'12.4"e, eye alt 928 m. [August 1, 2021].
Available at: `http://www.earth.google.com` (Cited on pages xiii and 69)

Grant, O.M., Tronina, L., Jones, H.G. and Chaves, M.M. (2006). Exploring thermal imaging variables for the detection of stress responses in grapevine under different irrigation regimes. *Journal of Experimental Botany*, vol. 58, no. 4, pp. 815–825. (Cited on pages 1, 12, 17, 18, and 31)

Guilioni, L., Jones, H.G., Leinonen, I. and Lhomme, J.P. (2008). On the relationships between stomatal resistance and leaf temperatures in thermography. *Agricultural and Forest Meteorology*, vol. 148, no. 11, pp. 1908–1912. (Cited on page 14)

Gutiérrez, S., Diago, M.P., Fernández-Novales, J. and Tardaguila, J. (2018). Vineyard water status assessment using on-the-go thermal imaging and machine learning. *PLOS ONE*, vol. 13, no. 2, p. e0192037. (Cited on pages 18, 21, and 71)

Gutiérrez, S., Fernandez-Novales, J., Diago, M.-P., Iniguez, R. and Tardaguila, J. (2021). Assessing and mapping vineyard water status using a ground mobile thermal imaging platform. *Irrigation Science*, vol. 39, no. 4, pp. 457–468. (Cited on pages 10, 57, 62, and 74)

Horwitz, J.W. (1999). Water at the ice point: a useful quasi-blackbody infrared calibration source. *Applied Optics*, vol. 38, no. 19, pp. 4053–4057. (Cited on page 8)

Idso, S.B., Jackson, R.D., Pinter, P.J., Reginato, R.J. and Hatfield, J.L. (1981). Normalizing the stress-degree-day parameter for environmental variability. *Agricultural Meteorology*, vol. 24, pp. 45–55. (Cited on pages 2, 8, 9, 12, and 31)

Ihuoma, S.O. and Madramootoo, C.A. (2017). Recent advances in crop water stress detection. *Computers and Electronics in Agriculture*, vol. 141, pp. 267–275. (Cited on page 10)

IPCC (2021). Climate change 2021 the physical science basis. Working Group I contribution to the Sixth Assessment Report of the Intergovernmental Panel on Climate Change. (Cited on page 1)

Jackson, R.D. (1982). Canopy temperature and crop water stress. In: *Advances in Irrigation*, vol. 1, pp. 43–85. Elsevier. (Cited on page 1)

Jolliffe, I.T. and Cadima, J. (2016). Principal component analysis: a review and recent developments. *Philosophical Transactions of the Royal Society A: Mathematical, Physical and Engineering Sciences*, vol. 374, no. 2065, p. 20150202. (Cited on page 43)

Jones (1999). Use of infrared thermometry for estimation of stomatal conductance as a possible aid to irrigation scheduling. *Agricultural and Forest Meteorology*, vol. 95, no. 3, pp. 139–149. (Cited on pages 2, 9, 11, 12, 14, 19, 31, 32, 33, 34, 35, 62, 78, and 80)

Jones, H.G. (2002). Use of infrared thermography for monitoring stomatal closure in the field: application to grapevine. *Journal of Experimental Botany*, vol. 53, no. 378, pp. 2249–2260. (Cited on pages 9, 10, 11, 12, 18, 25, 34, 57, and 74)

Jones, H.G. (2004). Application of thermal imaging and infrared sensing in plant physiology and ecophysiology. In: *Advances in Botanical Research*, vol. 41, pp. 107–163. Elsevier. (Cited on page 54)

Jones, H.G. (2018). Thermal imaging and infrared sensing in plant ecophysiology. In: *Advances in Plant Ecophysiology Techniques*, pp. 135–151. Springer International Publishing. (Cited on pages 8, 10, 13, and 64)

Jones, H.J. (2014). *Plants and Microclimate*. 3rd edn. Cambridge University Press. (Cited on pages 14, 32, and 92)

Kaplan, H. (2007). *Practical Applications of Infrared Thermal Sensing and Imaging Equipment, Third Edition*. SPIE. (Cited on pages 5, 6, and 7)

Keller, M. (2015). Phenology and growth cycle. In: *The Science of Grapevines*, pp. 59–99. Elsevier. (Cited on page 9)

King, B.A. and Shellie, K.C. (2016). Evaluation of neural network modeling to predict non-water-stressed leaf temperature in wine grape for calculation of crop water stress index. *Agricultural Water Management*, vol. 167, pp. 38–52. (Cited on pages 20, 21, 47, and 78)

King, W.B. and King, W.B. (1984). Geomorphology of the Cape Peninsula. Cape Town: University of Cape Town [2021, March 13].
Available at: `https://open.uct.ac.za/handle/11427/23262` (Cited on page 33)

Klepper, B. (1968 December). Diurnal pattern of water potential in woody plants. *Plant Physiology*, vol. 43, no. 12, pp. 1931–1934.
Available at: https://doi.org/10.1104/pp.43.12.1931 (Cited on page 16)

Kumar, N., Adeloye, A.J., Shankar, V. and Rustum, R. (2020). Neural computing modelling of the crop water stress index. *Agricultural Water Management*, vol. 239, p. 106259. (Cited on page 20)

Lee, K. and Park, J.-b. (2006). Application of particle swarm optimization to economic dispatch problem: Advantages and disadvantages. In: *2006 IEEE PES Power Systems Conference and Exposition*, pp. 188–192. IEEE. (Cited on pages 33 and 41)

Leeuwen, C.V., Trégoat, O., Choné, X., Bois, B., Pernet, D. and Gaudillère, J.-P. (2009). Vine water status is a key factor in grape ripening and vintage quality for red bordeaux wine. how can it be assessed for vineyard management purposes? *OENO One*, vol. 43, no. 3, p. 121. (Cited on page 17)

Leigh, A., Close, J.D., Ball, M.C., Siebke, K. and Nicotra, A.B. (2006). Research note: Leaf cooling curves: measuring leaf temperature in sunlight. *Functional Plant Biology*, vol. 33, no. 5, p. 515. (Cited on page 64)

Maes, W.H., Baert, A., Huete, A.R., Minchin, P.E.H., Snelgar, W.P. and Steppe, K. (2016). A new wet reference target method for continuous infrared thermography of vegetations. *Agricultural and Forest Meteorology*, vol. 226-227, pp. 119–131. (Cited on page 32)

Mahooti, M. (2021). Nrel's solar position algorithm (spa). Matlab File Exchange [2021, June 23.
Available at: https://www.mathworks.com/matlabcentral/fileexchange/59903-nrel-s-solar-position-algorithm-spa (Cited on page 38)

Marrero, T.R. and Mason, E.A. (1972). Gaseous diffusion coefficients. *Journal of Physical and Chemical Reference Data*, vol. 1, no. 1, pp. 3–118. (Cited on page 39)

Martin, R.F. (2000). General deming regression for estimating systematic bias and its confidence interval in method-comparison studies. *Clinical Chemistry*, vol. 46, no. 1, pp. 100–104. (Cited on page 68)

Matese, A., Baraldi, R., Berton, A., Cesaraccio, C., Gennaro, S.D., Duce, P., Facini, O., Mameli, M., Piga, A. and Zaldei, A. (2018). Estimation of water stress in grapevines using proximal and remote sensing methods. *Remote Sensing*, vol. 10, no. 1, p. 114. (Cited on page 21)

Maxwell, E.L., Stoffel, T.L. and Bird, R.E. (1986). Measuring and modeling and solar and irradiance on vertical and surfaces. Tech. Rep., Solar Energy Research Institute. (Cited on page 38)

Medrano, H., Tomás, M., Martorell, S., Escalona, J.-M., Pou, A., Fuentes, S., Flexas, J. and Bota, J. (2014 December). Improving water use efficiency of vineyards in semi-arid regions. a review. *Agron. Sustain. Dev.*, vol. 35, no. 2, pp. 499–517.
Available at: https://doi.org/10.1007/s13593-014-0280-z (Cited on page 1)

Melexis (2019). *MLX90614 family*. [2020, August 10].
Available at: https://www.melexis.com/en/documents/documentation/datasheets/datasheet-mlx90614 (Cited on pages 25 and 29)

Mills, A.F. and Gansen, V. (2009). *Heat transfer*. Pearson India Education Services. (Cited on page 37)

Minkina, W. and Dudzik, S. (2006). Simulation analysis of uncertainty of infrared camera measurement and processing path. *Measurement*, vol. 39, no. 8, pp. 758–763. (Cited on page 88)

Minkina, W. and Dudzik, S. (2009). *Infrared Thermography Errors and Uncertainties*. Wiley. (Cited on pages 5, 6, 8, 88, and 89)

Moller, M., Alchanatis, V., Cohen, Y., Meron, M., Tsipris, J., Naor, A., Ostrovsky, V., Sprintsin, M. and Cohen, S. (2007). Use of thermal and visible imagery for estimating crop water status of irrigated grapevine. *Journal of Experimental Botany*, vol. 58, no. 4, pp. 827–838. (Cited on pages 10, 32, 40, 47, and 72)

Mwinuka, P.R., Mbilinyi, B.P., Mbungu, W.B., Mourice, S.K., Mahoo, H.F. and Schmitter, P. (2021 February). The feasibility of hand-held thermal and UAV-based multispectral imaging for canopy water status assessment and yield prediction of irrigated african eggplant (solanum aethopicum l). *Agricultural Water Management*, vol. 245, p. 106584.
Available at: https://doi.org/10.1016/j.agwat.2020.106584 (Cited on pages 5 and 72)

Nobel, P.S. (2009). *Physicochemical and Environmental Plant Physiology*. 4th edn. Oxford: Elsevier Academic Press. (Cited on pages 38 and 47)

Noguera, M., Millán, B., Pérez-Paredes, J.J., Ponce, J.M., Aquino, A. and Andújar, J.M. (2020). A new low-cost device based on thermal infrared sensors for olive tree canopy temperature measurement and water status monitoring. *Remote Sensing*, vol. 12, no. 4, p. 723. (Cited on pages 7, 11, and 66)

North, G. (2015). *Encyclopedia of atmospheric sciences*. Academic Press, London. (Cited on page 64)

Olivo, N., Girona, J. and Marsal, J. (2008). Seasonal sensitivity of stem water potential to vapour pressure deficit in grapevine. *Irrigation Science*, vol. 27, no. 2, pp. 175–182. (Cited on page 9)

Peel, M.C., Finlayson, B.L. and McMahon, T.A. (2007). Updated world map of the köppen-geiger climate classification. *Hydrology and Earth System Sciences*, vol. 11, no. 5, pp. 1633–1644. (Cited on page 33)

Pellegrino, A., Clingeleffer, P., Cooley, N. and Walker, R. (2014 jun). Management practices impact vine carbohydrate status to a greater extent than vine productivity. *Frontiers in Plant Science*, vol. 5. (Cited on page 2)

Petrie, P.R., Wang, Y., Liu, S., Lam, S., Whitty, M.A. and Skewes, M.A. (2019). The accuracy and utility of a low cost thermal camera and smartphone-based system to assess grapevine water status. *Biosystems Engineering*, vol. 179, pp. 126–139. (Cited on pages 2, 10, 11, 12, 17, 21, 31, 32, 34, and 74)

Pineda, M., Baron, M. and Perez-Bueno, M. (2020). Thermal imaging for plant stress detection and phenotyping. *Remote Sensing*, vol. 13, no. 1, p. 68. (Cited on pages 18 and 19)

Poblete-Echeverria, C., Ahumada-Orellana, L., Zuniga, M., Sepulveda-Reyes, D. and Ortega-Farias, S. (2019 sep). Comparing water potential variables under different water stress levels: a case study on carménère grapevines. *Acta Horticulturae*, , no. 1253, pp. 101–108. (Cited on pages 16 and 17)

Poblete-Echeverria, C., Espinace, D., Sepulveda-Reyes, D., Zuniga, M. and Sanchez, M. (2017). Analysis of crop water stress index cwsi for estimating stem water potential in grapevines: comparison between natural reference and baseline approaches. *Acta Horticulturae*, vol. 1150, pp. 189–194. (Cited on pages 1, 8, 31, and 70)

Poirier-Pocovi, M., Volder, A. and Bailey, B.N. (2020). Modeling of reference temperatures for calculating crop water stress indices from infrared thermography. *Agricultural Water Management*, vol. 233, p. 106070. (Cited on pages 2, 10, 11, 12, 19, 31, 32, and 78)

Pou, A., Diago, M.P., Medrano, H., Baluja, J. and Tardaguila, J. (2014). Validation of thermal indices for water status identification in grapevine. *Agricultural Water Management*, vol. 134, pp. 60–72. (Cited on pages 10, 11, 31, 55, 62, and 74)

Prueger, J.H., Parry, C.K., Kustas, W.P., Alfieri, J.G., Alsina, M.M., Nieto, H., Wilson, T.G., Hipps, L.E., Anderson, M.C., Hatfield, J.L., Gao, F., McKee, L.G., McElrone, A., Agam, N. and Los, S.A. (2018). Crop water stress index of an irrigated vineyard in the central valley of california. *Irrigation Science*, vol. 37, no. 3, pp. 297–313. (Cited on page 18)

Reda, I. and Andreas, A. (2008). Solar position and algorithm for and solar radiation and applications. Tech. Rep., National Renewable Energy Laboratory. (Cited on page 38)

Rienth, M. and Scholasch, T. (2019). State-of-the-art of tools and methods to assess vine water status. *OENO One*, vol. 53, no. 4. (Cited on pages 15 and 16)

Ru, C., Hu, X., Wang, W., Ran, H., Song, T. and Guo, Y. (2020). Evaluation of the crop water stress index as an indicator for the diagnosis of grapevine water deficiency in greenhouses. *Horticulturae*, vol. 6, no. 4, p. 86. (Cited on page 11)

Rud, R., Cohen, Y., Alchanatis, V., Levi, A., Brikman, R., Shenderey, C., Heuer, B., Markovitch, T., Dar, Z., Rosen, C., Mulla, D. and Nigon, T. (2014). Crop water stress index derived from multi-year ground and aerial thermal images as an indicator of potato water status. *Precision Agriculture*, vol. 15, no. 3, pp. 273–289. (Cited on page 32)

Sepúlveda-Reyes, D., Ingram, B., Bardeen, M., Zúñiga, M., Ortega-Farías, S. and Poblete-Echeverría, C. (2016). Selecting canopy zones and thresholding approaches to assess grapevine water status by using aerial and ground-based thermal imaging. *Remote Sensing*, vol. 8, no. 10, p. 822. (Cited on pages 10, 12, 21, 31, 52, 62, and 77)

Shellie, K.C. and King, B.A. (2020). Application of a daily crop water stress index to deficit irrigate malbec grapevine under semi-arid conditions. *Agriculture*, vol. 10, no. 11, p. 492. (Cited on pages 31, 32, and 76)

Stockl, D., Dewitte, K. and Thienpont, L.M. (1998 November). Validity of linear regression in method comparison studies: is it limited by the statistical model or the quality of the analytical input data? *Clinical Chemistry*, vol. 44, no. 11, pp. 2340–2346. (Cited on page 68)

Stoll, M. and Jones, H.G. (2007). Thermal imaging as a viable tool for monitoring plant stress. *J. Int. Sci. Vigne Vin*, vol. 42, no. 2, pp. 77–84. (Cited on pages 1 and 34)

Stull, R. (2011). Wet-bulb temperature from relative humidity and air temperature. *Journal of Applied Meteorology and Climatology*, vol. 50, no. 11, pp. 2267–2269. (Cited on page 41)

Van Asbroeck, S. (2018). *Measuring, Logging and Analyzing Continuous Thermal Data to Assess Grapevine*. Master's thesis. Unpublished masters thesis. Stellenbosch: Stellenbosch University [Online]. (Cited on pages 7 and 76)

Van Leeuwen, C., Trégoat, O., Choné, X., Bois, B., Pernet, D. and Gaudillère, J.-P. (2009). Vine water status is a key factor in grape ripening and vintage quality for red bordeaux wine. how can it be assessed for vineyard management purposes? *OENO One*, vol. 43, no. 3, p. 121. (Cited on pages 2 and 69)

Watson, A.N. (1933). Preliminary study of the relation between thermal emissivity and plant temperatures. *Ohio J. Sci.*, vol. 33, pp. 435–450. (Cited on pages 36 and 54)

Webb, L.B., Whetton, P.H. and Barlow, E.W.R. (2007 oct). Modelled impact of future climate change on the phenology of winegrapes in Australia. *Australian Journal of Grape and Wine Research*, vol. 13, no. 3, pp. 165–175. (Cited on page 1)

Zhou, Z., Majeed, Y., Naranjo, G.D. and Gambacorta, E.M.T. (2021). Assessment for crop water stress with infrared thermal imagery in precision agriculture: A review and future prospects for deep learning applications. *Computers and Electronics in Agriculture*, vol. 182, p. 106019. (Cited on pages 1, 2, and 68)